

Documentation of Hybrid Hydride Model for Incorporation into Moose- Bison and Validation Strategy

Fuel Cycle Research & Development

*Prepared for
U.S. Department of Energy
Used Fuel Disposition*

Veena Tikare, Philippe Weck, Peter Schultz,
Blythe Clark, and John Mitchell, Sandia National
Laboratories

Michael Glazoff, Idaho National Laboratory

Eric Homer, Brigham Young University

Sandia National Laboratories

August 2014

FCRD-UFD-2014-000063 Rev. 0

SAND2014-19022 R



APPENDIX E
FCT DOCUMENT COVER SHEET ¹

Name/Title of Deliverable/Milestone/Revision No. Documentation of Hybrid Hydride Model for Incorporation into Moose-Bison and Validation Strategy

Work Package Title and Number FT-14SN081002

Work Package WBS Number 1.02.08.10

Responsible Work Package Manager Veena Tikare *Sylvia J. Sattler for Veena Tikare*
 (Name/Signature)

Date Submitted: August 15, 2014

Quality Rigor Level for Deliverable/Milestone ²	<input checked="" type="checkbox"/> QRL-3	<input type="checkbox"/> QRL-2	<input type="checkbox"/> QRL-1 Nuclear Data	<input type="checkbox"/> Lab/Participant QA Program (no additional FCT QA requirements)
--	---	--------------------------------	---	---

This deliverable was prepared in accordance with Sandia National Laboratories
 (Participant/National Laboratory Name)

QA program which meets the requirements of
 DOE Order 414.1 NQA-1-2000 Other

This Deliverable was subjected to:

Technical Review

Technical Review (TR)

Review Documentation Provided

Signed TR Report or,

Signed TR Concurrence Sheet or,

Signature of TR Reviewer(s) below

Name and Signature of Reviewers

Sylvia J. Sattler

Peer Review

Peer Review (PR)

Review Documentation Provided

Signed PR Report or,

Signed PR Concurrence Sheet or,

Signature of PR Reviewer(s) below

NOTE 1: Appendix E should be filled out and submitted with the deliverable. Or, if the PICS:NE system permits, completely enter all applicable information in the PICS:NE Deliverable Form. The requirement is to ensure that all applicable information is entered either in the PICS:NE system or by using the FCT Document Cover Sheet.

NOTE 2: In some cases there may be a milestone where an item is being fabricated, maintenance is being performed on a facility, or a document is being issued through a formal document control process where it specifically calls out a formal review of the document. In these cases, documentation (e.g., inspection report, maintenance request, work planning package documentation or the documented review of the issued document through the document control process) of the completion of the activity, along with the Document Cover Sheet, is sufficient to demonstrate achieving the milestone. If QRL 1, 2, or 3 is not assigned, then the Lab / Participant QA Program (no additional FCT QA requirements) box must be checked, and the work is understood to be performed and any deliverable developed in conformance with the respective National Laboratory / Participant, DOE or NNSA-approved QA Program.

DISCLAIMER

This information was prepared as an account of work sponsored by an agency of the U.S. Government. Neither the U.S. Government nor any agency thereof, nor any of their employees, makes any warranty, expressed or implied, or assumes any legal liability or responsibility for the accuracy, completeness, or usefulness, of any information, apparatus, product, or process disclosed, or represents that its use would not infringe privately owned rights. References herein to any specific commercial product, process, or service by trade name, trade mark, manufacturer, or otherwise, does not necessarily constitute or imply its endorsement, recommendation, or favoring by the U.S. Government or any agency thereof. The views and opinions of authors expressed herein do not necessarily state or reflect those of the U.S. Government or any agency thereof.



Sandia National Laboratories is a multi-program laboratory managed and operated by Sandia Corporation, a wholly owned subsidiary of Lockheed Martin Corporation, for the U.S. Department of Energy's National Nuclear Security Administration under contract DE-AC04-94AL85000.

Sandia Review and Approval Number: SAND2014-19022 R.

Approved for Unclassified Unlimited Release

SUMMARY

This report documents the development, demonstration and validation of a mesoscale, microstructural evolution model for simulation of zirconium hydride δ -ZrH_{1.5} precipitation in the cladding of used nuclear fuels that may occur during long-term dry storage. While the Zr-based claddings are manufactured free of any hydrogen, they absorb hydrogen during service, in the reactor by a process commonly termed ‘hydrogen pick-up’. The precipitation and growth of zirconium hydrides during dry storage is one of the most likely fuel rod integrity failure mechanisms either by embrittlement or delayed hydride cracking of the cladding (Hanson et al., 2011). While the phenomenon is well documented and identified as a potential key failure mechanism during long-term dry storage (Birk et al., 2012 and NUREG/CR-7116), the ability to actually predict the formation of hydrides is poor. The model being documented in this work is a computational capability for the prediction of hydride formation in different claddings of used nuclear fuels. This work supports the Used Fuel Disposition Research and Development Campaign in assessing the structural engineering performance of the cladding during and after long-term dry storage.

In this work, a model to numerically simulate hydride precipitation at the microstructural scale, in a wide variety of Zr-based claddings, under dry-storage conditions is being developed. It will be used to aid in the evaluation of the mechanical integrity of used fuel rods during dry storage and transportation by providing the structural conditions from the microstructural scale to the continuum scale to engineering component scale models to predict if the used fuel rods will perform without failure under normal and off-normal conditions. The microstructure, especially, the hydride structure is thought to be a primary determinant of cladding failure, thus this component of UFD’s storage and transportation analysis program is critical.

The model development, application and validation of the model are documented and the limitations of the current model are discussed. The model has been shown to simulate hydride precipitation in Zircaloy-4 cladding with correct morphology, thermodynamics and kinetics. An unexpected insight obtained from simulations hydride formation in Zircaloy-4 is that small (sub-micron) precipitates need to order themselves to form the larger hydrides typically described as radially-reoriented precipitates. A limitation of this model is that it does not currently solve the stress state that forms dynamically in the precipitate or matrix surrounding the precipitate. A method to overcome the limitations is suggested and described in detail. The necessary experiments to provide key materials physics and to validate the model are also recommended.

Hanson, B., H. Alsaed, C. Stockman, D. Enos, R. Meyer, and K. Sorenson (2011). *Gap Analysis to Support Extended Storage of Used Nuclear Fuel*, FCRD-USED-2011 000136, PNNL-20509.

Birk, S., B. Hanson, S. Marschman, B. Sindelar, K. Sorenson, and J. Wagner (2012). *Used Nuclear Fuel Storage and Transportation Research, Development and Demonstration Plan*, FCRD-FCT-2012-000053.

NUREG / CR-7116, (2011). *Materials Aging Issues and Aging Management for Extended Storage and Transportation of Spent Nuclear Fuel*.

ACKNOWLEDGEMENTS

The authors would like to thank Sylvia J. Saltzstein (Dept. 6225, Storage and Transportation Technologies), Ken B. Sorenson (Dept. 6223, Advanced Nuclear Fuel Cycle Technologies), Evaristo J. Bonano (Center 6220, Advanced Nuclear Energy Programs) and the 6000 Division at Sandia National Laboratories for supporting this research. The authors also wish to thank John M. Scaglione (ORNL, Reactor and Nuclear Systems Division) for supporting this research, providing invaluable feedback during the course of this work, and editing and critical review of this document.

Efrain Hernandez and Remi Dingreville at Sandia National Laboratories are also acknowledged for providing information on modeling and for useful discussions. We thank Steve Marschman (INL) for his comments during the review of this report.

Finally, we would like to thank Laura Connolly for her help during the preparation of this report and for reviewing this report.

TABLE OF CONTENTS

SUMMARY	iv
ACKNOWLEDGEMENTS	vi
TABLE OF CONTENTS	vii
LIST OF FIGURES	ix
LIST OF TABLES	xii
ACRONYMS	xiii
1. INTRODUCTION	1-1
2. HYBRID POTTS-PHASE FIELD MODEL DESCRIPTION, VERIFICATION, AND VALIDATION	2-5
2.1 Potts Model	2-6
2.2 Phase Field Model	2-7
2.3 Comparison of Potts and Phase Field Models	2-8
2.4 Hybrid Potts-Phase Field Model	2-8
2.5 Verification and Validation of the Hybrid Model	2-10
2.5.1 Implementation and verification of the hybrid code and framework	2-12
2.6 Summary and Conclusions	2-26
2.7 References	2-27
3. ADAPTION OF HYBRID POTTS-PHASE FIELD MODEL TO SIMULATE δ -ZrH _{1.5} PRECIPITATION IN Zr-BASED CLADDINGS	3-1
3.1 Zirconium-Based Cladding Composition and Microstructure	3-2
3.1.1 Generating a Digital Microstructure	3-9
3.2 Phase Stability and Thermodynamics of Zirconium-Based Cladding	3-11
3.2.1 Generating Free Energies	3-12
3.2.2 δ -ZrH _{1.5} Precipitation	3-16
3.2.3 Modeling δ -ZrH _{1.5} Precipitation	3-22
3.3 Summary and Conclusions	3-35
3.4 References	3-36
4. APPLICATION AND VALIDATION OF THE HYBRID POTTS-PHASE FIELD MODEL FOR SIMULATION OF δ -ZrH _{1.5} PRECIPITATION IN THE α -Zr MATRIX	4-1
4.1 Case I: δ -ZrH _{1.5} Hydride Formation during Hydrogen Charging	4-1
4.1.1 Model Validation	4-4
4.1.2 Discussion	4-14
4.2 Case II: Precipitation and Reorientation of δ -ZrH _{1.5} Precipitates	4-15
4.2.1 Model Validation	4-18
4.2.2 Discussion	4-26

4.3	Summary and Conclusions.....	4-26
4.4	References	4-27
5.	DEVELOPMENT OF HYBRID POTTS-PHASE FIELD MODEL FOR SIMULATION OF ZIRCONIUM HYDRIDE PRECIPITATE FORMATION AND ZIRCALOY-4 CLADDINGS: FUTURE DEVELOPMENT TO INCORPORATE MORPHOLOGY OF PRECIPITATES.....	5-1
5.1	Precipitate Morphology.....	5-1
5.2	Thermodynamics of precipitation	5-6
5.3	Kinetics of precipitate nucleation and growth.....	5-7
5.4	Radiation-induced dislocation and growth in HCP α -Zr	5-9
5.5	Model Adaptation to Incorporate Precipitate Morphology	5-12
5.6	Discovery and Validation Experiments.....	5-13
5.7	Summary and Conclusions.....	5-14
5.8	References	5-15

LIST OF FIGURES

- Figure 2.1. Composition-dependent free-energy functional for the two-phase, two-component system studied in this work. 2-12
- Figure 2.2. Illustration of the simultaneous sharp/diffuse interface of the hybrid model. The two different phase regions of the 1-D model are separated by a sharp interface as denoted by the phase shading, while the composition (symbols) shows a diffuse interface with the composition gradient between the equilibrium compositions of the two phases. 2-13
- Figure 2.3. Composition evolution in (a) single-phase and (b) two-phase diffusion couples. The system in (a) starts with a step function in the composition with values at 0.0 and 0.6. The system evolves toward the equilibrium composition value of 0.3. The system in (b) starts with a two-phase microstructure all at a composition of 0.5. The system evolves toward the equilibrium compositions, $C_\alpha = 0.3$ and $C_\beta = 0.7$. In both cases the simulation data are open circles and the error function fit to the data is given by the solid line denoting an effective diffusivity value of 2.2. 2-15
- Figure 2.4. Grain growth curves for (a) single-phase and (b) two-phase systems. The single-phase systems have a grain growth exponent of 1/2 for all temperatures while the two-phase system shows stagnation at low temperatures and a grain growth exponent of 1/3 for higher temperatures denoting diffusion-limited grain growth. 2-16
- Figure 2.5. Snapshots of the (a) grain structure, (b) phase structure and (c) composition at various times for the two-component, two-phase system. The snapshots show grain and phase coarsening that tracks with the composition map, with each of the phases having compositions near the equilibrium values. α -phase grains, phase membership, and composition range are indicated by shades of blue; β -phase by shades of red. 2-18
- Figure 2.6. Snapshot of the phase and composition through the microstructure at a given position as indicated by the inset. The composition gradients track the phase boundaries quite well, with the individual phases each near their equilibrium composition values of 0.3 and 0.7. Deviations from these values are largely the result of the phase coarsening which necessitates diffusion of the composition such that some areas of the microstructure temporarily deviate from their equilibrium values. 2-19
- Figure 2.7. Two-phase system illustrating the diffusion of species from high curvature regions to low curvature regions according to the Gibbs-Thomson equation. The higher solubility of the A-component (shown in red) in the β phase (shown in blue) at surfaces of high positive curvature will drive diffusion of A to regions of high negative curvature, where the B-component on the other side is in a region of high positive curvature and is diffusing away. The diffusion kinetics limit the rate of microstructural coarsening. 2-20
- Figure 2.8. Snapshots of the (a) grain structure, (b) phase structure and (c) composition at various times for nucleation and phase transformations in the model two-component, two-phase system. The initial conditions involve a single phase at a compositions far from equilibrium. Nucleation is then prescribed at a given rate that results in the nucleation of the second phase which grows and consumes the majority of the system. α -phase grains, phase membership, and composition range are indicated by shades of blue; β -phase by shades of red. 2-23
- Figure 3.1. Estimated cladding temperature after drying during dry-storage (Hansen, 2012). 3-2
- Figure 3.2. A wide range of grain sizes and shapes are obtained depending on the hot-rolling temperature and strain rate used to form Zircaloy-2 claddings (Chakravartty et al., 2010). 3-3
- Figure 3.3. SEM of fatigued Zircaloy-4 (Lin & Haicheng, 1998). 3-5
- Figure 3.4. Electron backscatter diffraction (EBSD) image showing a typical grain structure of Zircaloy-4 (Qin et al., 2011). 3-5
- Figure 3.5. Texture of a hot-rolled and annealed Zry-4 plate represented by experimental basal {0002} and prism {10-1 0} and {11-2 0} pole figures, with the rolling direction (RD), transverse direction (TD) and normal direction (ND) indicated (Wang et al., 2013). 3-6

Documentation of Hybrid Hydride Model for Incorporation into Moose-Bison and Validation Strategy
August 15, 2014

- Figure 3.6. Synthetically generated microstructure for Zircaloy-4 using (a) standard Potts model and (b) Dream3D. RD, ND and TD are the rolling direction, normal direction and transverse direction. 3-9
- Figure 3.7. The frequency of basal pole orientation as a function of rotation around the transverse direction, θ , and the rolling direction, φ . 3-10
- Figure 3.8. Phase diagram for Zr-H Binary System. 3-12
- Figure 3.9. An early Zr-H phase diagram proposed by Beck (Beck, 1962). 3-12
- Figure 3.10. Hexagonal (hcp) Zr structure (different views): (a) in the direction perpendicular to the (0001) axes; (b) in the direction of the (0001) axes. Zr atoms are shown in cyan color; octahedral interstitials are indicated by arrows. 3-13
- Figure 3.11a & b. HCP Zr with a dissolved hydrogen in the (a) octahedral site or (b) forming a metastable Zr-H-Zr bond (Glazoff, 2013). 3-14
- Figure 3.12a-c. The compounds (a) γ -ZrH, (b) δ -ZrH_{1.5} and (c) ϵ -ZrH₂ are orthorhombic, cubic and tetragonal respectively. Teal colored spheres represent Zr and while H atoms (Glazoff, 2013). 3-14
- Figure 3.13. The Gibbs free energy of the several phases in the Zr H system as a function of the hydrogen mole fraction at 800 K. The light blue curve, labeled 3, and the dark blue curve, labeled 4, are the free energies of the phases of interest, namely α -Zr and δ -ZrH_{1.5}, respectively. 3-15
- Figure 3.14. Portion of the Zr-H phase diagram showing a detailed view at the Zr-rich region. 3-15
- Figure 3.15. Free-energy curves for the Zr-H system at 300°C. 3-16
- Figure 3.16. ZrH precipitates in zircaloy cladding have a characteristic morphology. They align themselves to form platelets in the radial direction of the cylindrical clad. 3-17
- Figure 3.17. The ZrH precipitates have oriented themselves in the axial direction due to the hoop stresses present in the clad. 3-18
- Figure 3.18. A schematic diagram showing the orientation of δ -ZrH_{1.5} precipitates with respect to the α -Zr matrix grain (IUCR, 2014; Li et al., 1999). 3-21
- Figure 3.19. Preferential precipitation of hydrides on grain boundaries shown in SEM (left) and schematically (right) (Ells, 1968). 3-22
- Figure 3.20. ZrH_{1.6} precipitates with needle-like morphology align to form a larger plate (Perovic et al., 1983). 3-22
- Figure 3.21. Growth of hydride precipitates in a single crystal of α -Zr. The same set of precipitates is shown from two different directions. As one can see the precipitates are needle-like in shape and have three different orientations in the same plane. 3-26
- Figure 3.22. Starting microstructure for the hydride precipitation simulations. 3-27
- Figure 3.23. All in the precipitates in the polycrystalline are imaged and shown from two different angles. 3-27
- Figure 3.24. The same simulation was run with an uni-axial, constant stress applied. 3-28
- Figure 3.25. Precipitation size distribution in a polycrystalline Zr-matrix with randomly oriented grains for the case of no applied stress and application of a constant, uni-axial stress. The same data are shown on a log- and normal-plots. The log plot shows the data more clearly for larger needle sizes and the linear plot shows the data more clearly for the smaller shorter needles. 3-29
- Figure 3.26. Input microstructure with basal orientation stochastically assigned using Equation 3-1 for small simulations with seven grains. The grains are elongated in the X-direction, which is also the rolling direction for the purposes of this illustration. 3-30
- Figure 3.27a, b, and c. Nucleation and growth of δ -ZrH_{1.5} precipitates at time = 3, 27 and 520 Monte Carlo Steps (MCS). Nucleation sites are at predominantly at grain boundaries, which is very clearly illustrated in d, e and f. where the same precipitates seen in a, b and c are imaged, but now looking

- down the rolling direction. The inset between c and f is provided to show the grain boundaries at the surface of the sample and is the same microstructure shown in Figure 3.26. 3-31
- Figure 3.28. The distribution of hydrogen on the surfaces of the microstructure. Unlike, the precipitates only the hydrogen content on the surfaces can be imaged. Hydrogen concentrations are highest in the δ -ZrH_{1.5} precipitates and the matrix is depleted. 3-32
- Figure 3.29. A slice through the microstructure shown in Figure 3.27 and Figure 3.28. (a) the grain structure shown in blue with red precipitates and (b) the composition corresponding to this slice. The red in (b) are regions of high hydrogen content as shown in the scale to the right, which is where the precipitates are located. 3-33
- Figure 3.30. Nucleation of precipitation in this simulation occurs with equal probability in any location. Precipitates at time = 5 and 330 MCS are shown here. The subsequent growth is controlled by diffusion. 3-34
- Figure 3.31. The distribution of hydrogen in the microstructure for the simulation results shown in Figure 3.30. 3-34
- Figure 3.32. A comparison of total precipitate formation for the two cases where nucleation occurs randomly with uniform probability anywhere in the grains and nucleation occurs preferentially at the grain boundaries. 3-35
- Figure 4.1: Schematic of the aqueous charging procedure used to drive hydrogen into the Zr-alloy at 90⁰C and current density of 100 mA/cm². 4-2
- Figure 4.2: Hydride thicknesses as a function of hydrogen charging time measured by ERD on Zircaloy-2, Zircaloy -4 and ZirloTM. 4-2
- Figure 4.3: Hydride thicknesses as a function of hydrogen charging time measured for Zircaloy-2. 4-3
- Figure 4.4: TEM micrographs showing hydride layer formation in Zircaloy-2 at 100, 300 and 1000 s of hydrogen charging. 4-4
- Figure 4.5: The initial microstructure used for the simulation of hydrogen charging of Zr-alloys with hydrogen source at the bottom. The arrows show the direction that is perpendicular to the basal plane. 4-5
- Figure 4.6: The numerical data obtained from ThermoCalc used for determining free energies and chemical potentials. 4-6
- Figure 4.7: Hydrogenation of α -Zr by an infinite source of H at the bottom surface of the microstructure. (a) and (b) are at time t = 10 MCS and (c) and (d) are t = 100 MCS. (a) and (c) show the precipitates nucleating and growing from the bottom surface with the coloring at the top indicating the H concentration in α -Zr grains and (b) and (d) show the H concentration in the entire microstructure, both in the δ -ZrH_{1.5} precipitates and α -Zr grains. 4-8
- Figure 4.8: Average precipitate thickness as a function of diffusion time plotted on log scales. The diffusion exponent of 1.93, almost 2, indicates diffusion-controlled kinetics. 4-9
- Figure 4.9: Summary of diffusion coefficients in Zircaloy-2 and Zircaloy-4 measured experimentally by many and summarize by Kearns (Kearns, 1972). 4-10
- Figure 4.10: Hydrogen charging of the α -Zr by an infinite source of H at the bottom surface of the microstructure with differential diffusion in the δ -ZrH_{1.5} phase. (a) and (b) are at time t = 10 MCS and (c) and (d) are t = 100 MCS. (a) and (c) show the precipitates nucleating and growing from the bottom surface with the coloring at the top indicating the H concentration in α -Zr grains and (b) and (d) show the H concentration in the entire microstructure, both in the δ -ZrH_{1.5} precipitates and α -Zr grains. 4-12
- Figure 4.11: Average precipitate thickness as a function of diffusion time plotted on log scales for the uniform diffusion and differential diffusion in the δ -ZrH_{1.5} precipitate. 4-13

- Figure 4.12: Optical images showing δ -ZrH_{1.5} precipitates in (a) Zircaloy-2 and (b) Zircaloy-4 with H content of 600 ppm wt. (Colas et al., 2010) 4-16
- Figure 4.13: A schematic diagram showing the transverse, normal and rolling directions in a cladding. The preferred orientation of the basal pole is in the normal direction with the basal plane aligning preferentially in the rolling direction. The orientation of circumferentially and radially oriented precipitates is also shown in the expanded view of the square. 4-17
- Figure 4.14: Optical micrographs showing precipitate orientation in Zircaloy-4 with and without applied stress. The arrows indicate applied uniaxial stress of 85 MPa (Colas et al., 2010). 4-18
- Figure 4.15: Digitally generated Zircaloy-4 microstructure with the rolling, normal and transverse directions indicated. See Figure 4.13 for definitions of the three directions. The size of this volume is 100 x 100 x 25 μ m. 4-19
- Figure 4.16: A small portion (10 x 10 x 10 μ m shown by the inset at the top right) of the simulation is imaged as imaging the total microstructure would be overwhelming amount of data at time t = 20 MCS in (a) and (b) and t = 100 MCS in (b) and (d). All the precipitates in that volume are shown in (a) and (c) with each color corresponding to a precipitate. The compositions corresponding to that image at the surface of the volume is shown in (b) and (d) with the red areas are high in hydrogen and are the precipitates. 4-21
- Figure 4.17: Reorientation of precipitates in the volume shown in (a) when stress is applied along the (b) circumferential direction and (c) the radial direction. 4-23
- Figure 4.18: Reorientation of precipitates in a thin slice over the entire simulation area with (a) no stress is applied, and with stress applied along the (b) circumferential direction and (c) the radial direction. (d) A micrograph showing the precipitate reorientation under applied stress in the radial direction. The scale of the microstructural images (a) to (c) in shown by the inset blue box. 4-24
- Figure 4.19: Frequency plot of precipitate oriented in that direction for Zircaloy-4 with (a) randomly oriented grains and no texture and (b) with strong texture with the basal plane aligned in the rolling direction. 4-25
- Figure 4.20: A feature such as that shown in the blue box on the optical micrograph was thought to be formed by precipitates rotating and aligning themselves as shown to the left in dark blue. Our simulations, however, are suggesting that this is not possible and stacking of the precipitates as shown to the right in lighter blue is probably the explanation for this behavior. 4-26
- Figure 5.1: *Left:* (Top) *a*-type dislocation in an annealed zirconium microstructure at 427°C: (A) 1.1×10^{25} n/m²; (B) 1.5×10^{25} n/m². (Bottom) *c*-type dislocation in annealed Zircaloy-4 at 287°C: (C) 8.5×10^{25} n/m², (D) 7×10^{25} n/m² (adapted from Choi et al., 2013). *Right:* Schematic representation of basal vacancy loops and interstitial prismatic loops formed in the HCP α -phase of pure Zr and Zr alloys. 5-10
- Figure 5.2: *Left:* Irradiation growth in annealed iodine and zone-refined zirconium single crystals at 280°C (Carpenter et al., 1981; Rogerson, 1988). *Right:* Comparison of growth behavior of cold-worked zirconium and Zircaloy-2 (Zee et al., 1987). 5-11

LIST OF TABLES

Table 3.1. Alloy composition given in weight % (Whitmarsh, 1962; Allegheny Technologies; Natesan & Soppet, 2004)	3-4
Table 3.2. Zr-based alloys with the precipitates found in them characterized by Motta and co-workers (Motta et al., 2007).....	3-8
Table 5.1 Isotropic inclusions: shape parameters and material moduli. The ellipsoidal parameters given here describe a long/needle-like precipitate.....	5-3

ACRONYMS

1D	One-dimensional
2D	Two-dimensional
3D	Three-dimensional
BCC	Body-centered Cubic
CALPHAD	CALculation of PHase Diagrams
DFT	Density Functional Theory
ERD	Elastic Recoil Detection
FCC	Face-Centered Cubic
FCT	Face-Centered Tetragonal
FEM	Finite-Element Method
HCP	Hexagonal
KMC	Kinetic Monte-Carlo
M&S	Modeling and Simulation
MCS	Monte Carlo Steps
MPI	Message Passing Interface
ND	Normal Direction
NRC	Nuclear Regulatory Commission
ODF	Orientation Distribution Function
pRXA	Partially Recrystallized
RD	Rolling Direction
RIG	Radiation-Induced Growth
SEM	Scanning Electron Microscopy
SPPARKS	Stochastic Parallel PARTicle Kinetic Simulator
SRA	Stress Relief Annealed
TD	Transverse Direction
TEM	Transmission Electron Microscopy
V&V	Verification and Validation

1. INTRODUCTION

The US's current used fuel management policy may require ensuring the containment of radioactive materials during storage and subsequent transport for an indeterminately long period. Dry-storage is currently the only available option for long-term sequestration of used nuclear fuels. Until a permanent sequestration or disposition solution is found, used fuel must be stored for an indeterminately long time. One of the barriers available for fuel confinement is the Zr-based cladding. Ensuring the structural integrity of the cladding is a key component in developing the technical basis for long-term dry-storage. The precipitation and growth of zirconium hydrides during dry-storage is one of the potential fuel rod integrity failure mechanisms by either embrittlement or delayed hydride cracking of the cladding (Hanson et al, 2011). While the phenomenon is well documented and identified as a potential failure mechanism during long-term dry-storage (Birk et al., 2012; NUREG CR-7116; 2011) the ability to actually predict the formation of hydrides is poor. The model, described and demonstrated in this document, is being developed as a tool to predict hydride formation during long-term dry storage.

The formation of hydride precipitates in Zr-based claddings is a well-known and well-documented phenomenon. The zircaloy cladding oxidizes while in the reactor as



This reaction produces a surface oxide layer and H₂ gas. Some portion, estimated to be 5 to 20%, of the hydrogen gas released by this reaction is absorbed by the clad and diffuses into the clad. The absorption process is typically called hydrogen uptake. Depending on the alloy composition, temperature and amount of H absorbed, the H can stay dissolved in the cladding or it can precipitate forming zirconium hydride precipitates when the solubility limit is exceeded.

The morphology of the ZrH_{1.5} precipitates that form during service in reactor is characterized by platelets aligned in the circumferential direction of the cladding. The hydride is thought to precipitate at defects and grain boundaries that are preferentially aligned along the circumferential direction of the clad. Furthermore, they form preferentially near the outer surface of the cladding where the temperature is lower and solubility of the hydrogen in the α -Zr matrix is also lower. The circumferentially oriented hydrides form in reactor when the internal stress applied by the internal gas pressurization and swelling fuel is countered by the coolant pressure resulting in low or no tensile hoop stress. When the used fuel rods have completed their service life, they are stored in cooling pools for some years. When the storage pool approaches capacity, the assemblies are transferred to dry storage casks where they go through a drying operation either through vacuum drying or forced helium backfill. During the drying stage, due to the temperature increase, the hydride that has precipitated during pool cooling partially redissolves into the cladding depending on highest temperature achieved during drying. Upon cooling and subsequent dry-storage, the ZrH_{1.5} reprecipitates, but this time the precipitates are reoriented along the radial direction. The alignment is due to the stress state of the cladding. With the coolant no longer applying a compressive stress, the swelled fuel pellets cause a tensile hoop stress in the cladding. The ZrH_{1.5} precipitates form perpendicular to this hoop stress. This orientation is undesirable as the oriented precipitates act as stress concentrators and may lead to fracture and or rupture of the cladding during long-term storage.

This document demonstrates a basic hydride precipitation model that is built on a recently developed hybrid Potts-phase field model that combines elements of Potts-Monte Carlo and the

phase-field models (Homer et al., 2013; Tikare and Schultz, 2012). The model capabilities are demonstrated along with the incorporation of the starting microstructure, thermodynamics of the Zr-H system and the hydride formation mechanism. An application of the model on the Zircaloy-4 microstructure, and the next steps in model development to complete the model and acquire full prediction capability are summarized as follows:

- A realistic microstructure was generated for the Zircaloy-4 with both geometric and crystallographic texture. Based on findings in the literature, the capability of generating a rolled microstructure with elongated grains matching the aspect ratio of published data was demonstrated. Furthermore, the crystallographic grain orientations were assigned based on texture data also found in the published literature.
- The free energies of the two pertinent phases, α -Zr and δ -ZrH_{1.5} were calculated and incorporated into the hydride model. CALPHAD-type thermodynamics calculations were used to generate free-energy data for the Zr-H system with four phases, the matrix α -Zr and the three hydride phases γ -ZrH, δ -ZrH_{1.5}, and ϵ -ZrH₂. The free energies of the two pertinent phases, α -Zr and δ -ZrH_{1.6}^{*} were fitted to generate smooth free-energy curves and incorporated into the hydride model. Furthermore, the chemical potentials that drive the compositional and phase changes were upgraded in the model to simulate more complex materials with more components and more phases, as necessary, for future simulations.
- The hybrid Potts-phase field model was modified to include crystallographic texture so that hydride precipitate nucleation and growth would occur along the long axis of the precipitate in the basal plane of the underlying HCP α -Zr grain.
- The model can distribute nucleation sites in the microstructure to match known nucleation behavior. Nucleation is thought to occur at defects such as dislocation loops and near grain boundaries. These capabilities are demonstrated in the model by treating the case of nuclei distributed randomly with uniform probability of occurring anywhere in the grains and preferentially occurring near grain boundaries.
- Hydride precipitate growth is simulated in a stress-free cladding and one with a constant, uniaxial stress applied to shown that the hybrid model is capable of incorporating local micro-mechanical stress state. The local stress state is due to the pressure applied by the internal gas pressure and fuel swelling, and in response to the dilatation accompanying precipitate growth; this is an important parameter for correct simulation and more rigorous model with evolving micromechanics will be developed in the near future.
- This model has been verified and validated for simulating microstructural evolution coupled to compositional changes, including grain growth, phase transformation,

* The δ -ZrH_{1.5} precipitate has a FCC crystal structure with its minimum free-energy composition corresponding to a stoichiometry of 2:3. However, when forming in the α -Zr matrix its stoichiometry increases as the equilibrium composition of δ -phase shifts to higher stoichiometry, such as ZrH_{1.6} or higher. In this document, the ZrH_{1.5} stoichiometric composition will be used to identify the δ phase.

- nucleation and growth of second phase, and Fickian diffusion. Furthermore, the development and adaptation made for simulating hydride precipitation have been verified to correctly simulate the materials processes claimed in this work.
- In addition to verification, two validation exercises were performed. The first exercise was the simulation of experiments performed by Clark et al., (2013) on hydride formation as a surface layer during hydrogen charging of Zr-alloys; and the second was the simulation of δ -ZrH_{1.5} precipitate formation and reorientation with and without applied stress from a hydrogen-supersaturated Zircaloy-4. The first validation exercise was successful and even provided some insight into surface layer diffusion behavior. In the second exercise, the simulation of precipitation under no applied stress was in agreement with experimental results. The precipitates form in the basal plane of the HCP α -Zr matrix with alignment primarily in the circumferential direction, as the basal planes are primarily oriented in this direction. [Reorientation of the precipitates under applied stress, however, was not observed. Detailed examination of the simulation results shows that the individual precipitates could not rotate as they were confined to form in the basal planes of different grains.] Since very few grains had basal planes that were nominally aligned in the radial direction, precipitates also could not align in this direction. Thus, reorientation was not possible in textured Zircaloy-4. This was confirmed by simulating the same microstructure, but with no crystallographic texture. In this simulation, reorientation of precipitates was observed. This discrepancy in the reorientation behavior between the experiments and simulations was considered and the origin of the reorientation behavior is thought to be due to the elastic stress field that develops in and around precipitates. The stress field is thought to influence the nucleation of precipitates so that they order themselves to align in different configurations. [When no or low stress is applied, the elastic stress field around the precipitates orders nucleation and elastically stabilizes the size of the precipitates.] Under large tensile hoop stresses, the nuclei align themselves by stacking, so that the long edges of the precipitates align on top of each other to give features that look like reoriented precipitates. Based on the discrepancy observed regarding the reorientation behavior the following is proposed:
 - Add the elastic stress field around precipitates to the model so that its physics and influence on microstructural evolution can be simulated. The methodology that will be used is the Eshelby solution to determine the stress state in and around precipitates. The strain energy density will be incorporated into the equation of state of the hybrid model and used to study the ordering of precipitates under various applied stress conditions.
 - Incorporate the morphological feature of the hydride precipitates ordering into the hybrid model. The hybrid model will be used to directly simulate the morphologies and alignment of precipitates under various texture and stress conditions observed in the different claddings. These morphologies obtained from the hybrid model will provide constitutive equations to a rate-theory model that will be performed on a digital microstructure to predict precipitation and reorientation given the local conditions such as temperature, composition, microstructural features such as grain boundaries and other characteristics such as radiation defect densities. This model will solve evolution equations as the rate of known kinetic processes given the local conditions in such a microstructure instead of by direct numerical simulation of all

the kinetic processes that are active. Thus, using a two-stage model, the full precipitation prediction model will be completed.

Almost all simulation presented are simulated using software built on the platform SPPARKS (Plimpton et al, 2009), a Sandia code designed for particle-based kinetic Monte Carlo simulations. This code is written in standard C++ and can run on virtually any UNIX machine with parallel or serial computing capability. The code for the hydride simulations is built within the SPPARKS framework.

Hanson, B., H. Alsaed, C. Stockman, D. Enos, R. Meyer, and K. Sorenson (2011). *Gap Analysis to Support Extended Storage of Used Nuclear Fuel*, FCRD-USED-2011 000136, PNNL-20509.

Birk, S., B. Hanson, S. Marschman, B. Sindelar, K. Sorenson, and J. Wagner (2012). *Used Nuclear Fuel Storage and Transportation Research, Development and Demonstration Plan*, FCRD-FCT-2012-000053.

NUREG / CR-7116, (2011). *Materials Aging Issues and Aging Management for Extended Storage and Transportation of Spent Nuclear Fuel*.

Homer, E.R, V. Tikare, and E. A. Holm (2013). Hybrid Potts-Phase Field Model for Coupled Microstructural-Compositional Evolution, *Comp. Mater. Sci.* **69**: 414–423.

Tikare, V., and P. A. Schultz (2012). *Verification and Validation of the Hybrid Potts-Phase Field Model for Coupled Microstructural-Compositional Evolution*, FCT NEAMS VVUQ Report M3MS-12SN060602

2. HYBRID POTTS-PHASE FIELD MODEL DESCRIPTION, VERIFICATION, AND VALIDATION

The hybrid Potts-phase field model was developed to treat processes that evolve by coupled microstructural and compositional evolution and was chosen to be the basis for simulation of $ZrH_{1.5}$ precipitation in Zr-based claddings. This model is ideally suited to treat this complex process on a sufficiently large scale that it could inform engineering, fuel rod-scale simulations. It has the advantage of combining the efficiency of the Potts model with the detailed compositional gradients that are easily handled by the phase field model to give an integrated capability efficiently. Microstructural evolution and phase transitions in alloyed materials cannot be decoupled from the compositional evolution within the same material. This is especially true for the evolution of multi-phase materials or for phase transformations in materials that are limited by diffusion kinetics such as the precipitation of δ - $ZrH_{1.5}$ in Zr-based claddings. This coupling results from the fact that the local microstructure, which is often expressed only in terms of grains, grain boundaries, orientations, etc., is actually defined in part by the local composition. Furthermore, these microstructural and compositional fields are strongly influenced by a number of thermal and thermo-mechanical environments that induce driving forces for their evolution (Humphreys & Hatherly, 2004; Janssens et al., 2007).

Since these microstructural and compositional fields are so strongly influenced by thermal and thermo-mechanical operations and thereby govern the resulting behavior, any advances in the ability to properly correlate, characterize and predict the coupled evolution of these fields can yield results of no small consequence. Advancements of this type would allow for dramatic improvements in materials engineering and enhanced materials performance. Materials models could be used to simulate the entire life of a material in order to identify problems before the material was put into operation. Accurate simulation of material behavior could have significant implications for any number of fields including materials processing, nuclear fuels processing and performance, etc.; essentially, any thermal or thermo-mechanical operation that results in microstructural and compositional evolution (Allison et al., 2006; Allison, 2011).

Mesoscale models for simulation of microstructural evolution are highly developed. The two most popular and widely used ones are the phase field and the Potts models. They have been extensively applied to many materials processes. These models are sufficiently advanced that current trend in development of capabilities is to simulate multiple, coupled materials physics that drive microstructural evolution. One method of doing this is to have hybrid models. An early hybrid combined the Potts model with a cellular automaton model to simulate recrystallization (Rollett et al., 1992). Another introduced an annihilation step into the Potts model to simulate densification during sintering (Tikare et al., 2010). Coupling of the finite-element method (FEM) with particles and phase-field has also been done (Tonks et al., 2012). However, even with this level of sophistication, microstructure and composition are frequently treated independently, or when coupled the resulting model provides significant detail but is not efficient in handling large microstructural networks (Janssens et al., 2007; Holm & Battaile, 2001; Emmerich, 2003, Du et al., 2011).

The hybrid Potts-phase field model combines elements of the Potts Monte Carlo and phase field models. The equation of state describing the thermodynamics of the system is a combination of the typical equations of state used by each of the models, phase field and Potts. The advantage of such a hybrid compared to existing models is that it enables simulation of complex coupled-physics efficiently and effectively. In what follows, we detail the modeling framework and the nature of the coupling between the composition and microstructure. The framework and solution techniques are then validated against a number of common metrics. Finally, the model is applied to simulate phase transformations through the process of nucleation and growth of δ -ZrH_{1.5} precipitates in α -Zr matrix. The thermodynamic driving forces for the precipitate growth were obtained rigorously from Thermo-Calc calculations, the kinetics of precipitate growth were controlled by diffusion of hydrogen in the α -Zr matrix, the crystallographic alignment and shape of the precipitates were incorporated and the underlying microstructure of α -Zr with realistic shape and crystallographic texture was used as the starting microstructure for simulations.

The hybrid model developed here represents an integration of the Potts Monte Carlo model and the phase field model. In the following sections, the two models are introduced, and their normal applications, their advantages and disadvantages are discussed. Following these introductions, the hybrid model and the manner in which it combines the two component models to provide an efficient framework for simulating coupled microstructural-compositional evolution is described. Finally, the verification and validation (V&V) methodology and results are reviewed in detail.

2.1 Potts Model

The Potts model is a statistical mechanical model that utilizes Monte Carlo methods to evolve an ensemble of discrete particles defined on a lattice. This ensemble of particles represents the material microstructure. Each particle at each lattice site, identified by i , can assume a spin, q , that represents a given feature of the microstructure, such as membership in a grain or phase. Then, the total energy of the system is given by summing the bulk energy, E_v , of each particle at each lattice site, i , and the interfacial energy, J , between neighboring sites, j . This total energy is given as

$$E_p = \sum_{i=1}^N \left(E_v(q_i) + \sum_{j=1}^n J(q_i, q_j) \right) \quad \text{Eq. 2-1}$$

where N represents the total number of sites, and the interfacial energy for each site is determined by summing the function J , defined as

$$J = \begin{cases} 1 & \text{for } i \neq j \\ 0 & \text{for } i = j \end{cases} \quad \text{Eq. 2-2}$$

over all n neighbor sites of site i . A rejection Monte Carlo algorithm is then used to systematically attempt spin changes, or microstructure evolution, according to Boltzmann statistics. Specifically, the probability for the site changes is given as

$$P = \begin{cases} \exp\left(-\frac{\Delta E}{k_b T}\right) & \text{for } \Delta E > 0 \\ 1 & \text{for } \Delta E \leq 0 \end{cases} \quad \text{Eq. 2-3}$$

for a change in energy, ΔE , resulting from an attempted spin change. In this manner, the ensemble of particles evolves in such a way as to lower its overall energy, transforming the microstructure in the process. The details of the Potts Model are given in more detail in Janssens et al. (2007), Holm & Battaile (2001) and Wu (1982). The Potts model has been successfully employed to study grain growth (Anderson et al., 1984), grain growth with the effects of misorientation distributions and anisotropy (Holm et al., 1991, 2001), abnormal grain growth (Grest et al., 1990), recrystallization (Holm et al., 2003), Zener pinning (Miodownik et al., 1999, 2000), Ostwald ripening (Tikare & Cawley, 1998a, 1998b), and sintering (Hassold et al., 1990; Tikare et al., 2003, 2010; Braginsky et al., 2005). The versatile framework of the Potts model provides the ability to study any number of microstructure evolution characteristics in a statistically representative manner.

2.2 Phase Field Model

The phase field model is a continuum thermodynamic method that employs continuum state variables to represent the state of a microstructure in the simulation space. These continuum variables are digitized at discrete points on a lattice. Similar to the Potts model, the energy for the phase field model is obtained by integrating the bulk free energy, f_o , and the interfacial energy, $\kappa_{\eta_q}(\nabla\eta_q)^2$, over the entire sample. This is given as

$$E_{pf} = \int \left(f_o + \sum_{q=1}^Q \kappa_{\eta_q} (\nabla\eta_q)^2 \right) dV \quad \text{Eq. 2-4}$$

where the summation is over the Q phase fields and f_o is a bulk free energy function of all Q phase fields. Thus, materials processes that are driven by a combination of bulk and/or interfacial free energy minimization can be captured by this model. The evolution of the state (continuum) variables is simulated by kinetic equations, namely the Cahn-Hilliard for conserved quantities and the Ginzburg-Landau equation for non-conserved quantities. Both are dependent on a free energy functional that represents the thermodynamics of the materials system under consideration using a set of state variables characterized by the materials state. A key feature of the phase field model is that the interfaces are diffuse. The gradient term for each of the phase fields $\nabla\eta_q$ defines the interfacial energy as given in **Equation 2-4**. As such, a finite gradient results in a diffuse interface, whereas a sharp interface would result in an infinitely large interfacial energy. The phase field model is covered in more depth in Refs. Janssens et al, 2007; Emmerich, 2003; Chen, 2002; Steinbach, 2009). As suggested by its name, the phase field model is typically used to study phase interfaces and has proven quite useful in researching solidification fronts (such as dendritic growth) (Boettinger et al., 2002; Asta et al., 2009), multi-phase microstructure evolution (Nestler & Wheeler, 2000), grain growth (Rollett et al., 2002), phase field crystal modeling for ordering and dislocation structures, etc. (Wu et al., 2010;

Olmsted et al., 2011). The phase field method is also quite versatile and the continuum variables provide the ability to study smooth, finite-width interfaces.

2.3 Comparison of Potts and Phase Field Models

Both the Potts model and the phase field model have proven to be extremely useful in investigating the behavior of materials in many different cases, as discussed above. Yet, our desire is to model the simultaneous evolution of both microstructure and composition and neither of these modeling techniques is well suited to the task. In the Potts model, this limitation is due to the fact that all microstructure representations must be given by discrete integer values in order to fit into the Potts model. Thus, the ability to study composition evolution does not readily fit into the Potts model, yet these discrete integer values make it very efficient for statistical sampling of microstructures. In contrast, the phase field model is a continuum thermodynamic model, so it can analyze continuous fields such as composition easily, but it is inefficient for sampling large statistical microstructures because each grain requires an individual phase field that must be solved. Furthermore, phase field models can suffer from numerical instabilities, requiring small iterative steps to find solutions to the phase fields. Finally, phase field models require the derivation of a thermodynamic function for the system to be studied, and this derivation is not always a straightforward task.

2.4 Hybrid Potts-Phase Field Model

As indicated by its name, the hybrid Potts-phase field model marries the Potts and phase field models. It is demonstrated in this work by treating a coupled microstructure and composition evolution problem. The microstructure and composition are represented by an ensemble of particles in a continuum composition field. The particle ensemble populates a square grid and represents membership in a particular microstructural feature. Overlaying this same grid is the composition field with digitized values at the same grid points. Thus each site is defined by three variables: spin (integer value) that defines the microstructure, phase (integer value), and local composition (a real-valued number). Since we are considering a two-phase system, the spins are divided into two sets, one that identifies it as a grain of the α -phase and the other the β -phase.

In this hybrid Potts-phase field modeling framework, the overall free energy is again given by the sum of the volumetric free energy and the interfacial free energy as

$$E_{hybrid} = \sum_{i=1}^N \left(E_v(q_i, C_i) + \sum_{j=1}^n J(q_i, q_j) + \kappa_C (\nabla C_i)^2 \right) \quad \text{Eq. 2-5}$$

The volumetric energy term, E_v , is now a function of both the particle state and the composition at its location. The particular function used in this work will be described shortly. This explicit coupling between the microstructural and compositional fields in E_v will force the different features of the microstructure and composition fields to evolve in conjunction with one another. The interfacial energy due to grain boundaries is given by the neighbor interaction energy J , as described in **Equation 2-2**, and an interface energy

due to composition gradients is given by the $\kappa_C (\nabla C_i)^2$ term, similar to the $\kappa_{\eta q} (\nabla \eta_q)^2$ term contained in **Equation 2-4**.

For the purposes of this work, we define a bulk free energy function for a model two-phase, two-component system as

$$E_v(q_i, C_i) = \lambda \left[(C - C_1)^2 + (C_2 - C)^2 \right] + a(C - C_3)^2 q_\alpha + a(C_4 - C)^2 q_\beta \quad \text{Eq. 2-6}$$

In this equation, λ , C_1 , C_2 , C_3 , C_4 , and a are all phenomenological constants that are used to fit the desired phases and phase equilibria characteristics. C is the composition that is to be evolved and q_α and q_β are phase identifiers that are valued at 1 or 0 depending on the phase of a given site, either α or β . Based on this two-phase, two-component energy functional, each site will have a given bulk free energy that is dependent on the local site composition and the site phase.

The evolution of the microstructure and composition in the hybrid model is treated by iteratively evolving the microstructure and then the composition. This iterative approach is the same as that used in phase field models; each order parameter is evolved individually using the same energy functional for coupling them. In the hybrid model, the microstructure is evolved exactly as described in Section 3.1; however, the energy is calculated using **Equation 2-5** instead of **Equation 2-1**. The composition is evolved with the Cahn-Hilliard equation

$$\frac{\partial C}{\partial t} = M_C \left\{ \nabla^2 \frac{\partial E_v}{\partial C} - \kappa_C \nabla^4 C \right\} \quad \text{Eq. 2-7}$$

where E_v is the bulk free energy of the site, given by **Equation 2-6** and M_C and κ_C are related to the diffusion coefficient and interfacial energy, respectively.

This hybrid Potts-phase field model is well suited to handle the coupled microstructure-composition evolution because Potts models can treat large microstructures efficiently while the phase field method provides the level of detail required to track composition. Additionally, the bulk free energy function, E_v , can be defined in any number of ways to capture different microstructural and compositional features.

The spatial, energy and time scaling in the hybrid model warrants some attention. The Potts model, an inherently non-dimensional model (Raabe, 2000), requires the definition of units in length, energy and time to match thermodynamic and kinetic quantities of real materials. The phase-field model, a continuum thermodynamic approach, directly solves kinetic equations with real materials parameters for length, time and energy. This hybrid model requires that the units of time, energy and length be treated consistently to simulate those of real materials correctly. To achieve this consistency, we non-dimensionalize units for the continuum field quantities and normalize the remainder to match.

The standard methods for obtaining non-dimensional units in the phase-field model are used here. Non-dimensional length \tilde{l} is normalized by the quantity l defined as

$$l = \sqrt{\frac{\kappa_c}{k_B T}} \quad \text{Eq. 2-8}$$

where κ_c is the composition gradient energy term in **Equation 2-8** with units of (length² * energy) thus giving l units of length. Non-dimensional time, \tilde{t} is obtained by normalizing time by the quantity τ

$$\tau = \frac{l^2}{D} = \frac{l^2}{M_c k_B T} \quad \text{Eq. 2-9}$$

where M_c is the mobility in **Equation 2-9** with units of length²/(energy *time) giving τ units of time. Non-dimensional energy is obtained by simply normalizing by $k_B T$. The corresponding quantities in the discrete portion of the hybrid and then normalized by these same units. The pixel length, d , is normalized by l , time in Monte Carlo steps (MCS) by τ , and energy by $k_B T$. We reexamine the energy and kinetic equations given in these non-dimensionalized units. The energy is given in **Equation 2-5** becomes $\tilde{E}_{hybrid} = E_{hybrid}/k_B T$ where each component in E_v , J and $\kappa(\nabla C)^2$, are all normalized by $k_B T$. The kinetic equation for microstructural evolution (**Equation 2-3**) becomes

$$P = \begin{cases} \exp(\Delta\tilde{E}) & \text{for } \Delta\tilde{E} > 0 \\ 1 & \text{for } \Delta\tilde{E} \leq 0 \end{cases} \quad \text{Eq. 2-10}$$

where $\Delta\tilde{E}$ is the non-dimensionalized change in energy, or $\Delta E/k_B T$. The kinetic equation for the composition evolution **Equation 2-7** becomes

$$\frac{\partial c}{\partial \tilde{t}} = \tilde{M}_c \left\{ \tilde{\nabla}^2 \frac{\partial \tilde{E}}{\partial c} + \tilde{\kappa} \tilde{\nabla}^4 C \right\} \quad \text{Eq. 2-11}$$

where $\tilde{\nabla}$ signifies a gradient over the normalized length and the non-dimensionalized mobility and gradient energy term, given as \tilde{M} and $\tilde{\kappa}$ respectively, are both 1 by definition.

2.5 Verification and Validation of the Hybrid Model

Line of sight: The initial element of any V&V plan at the subcontinuum scale is to establish a line of sight into the assessed system, define requirements for the activity, and identify the quantities of interest.

The new mesoscale framework targets, as described above, the coupled microstructural and compositional evolution of metallic alloy materials, such as a U-Pu-Zr nuclear fuel. For continuum-scale models of fuel pellet performance, the temperature gradients and heat flow are dependent upon details of the microstructure, with the local fission rate density, i.e., the heat sources, dependent upon the local elemental compositions. Hence, the important output quantities of the mesoscale models are the microstructural character and compositional distributions within the modeling domain, as a function of time and irradiation conditions. Continuum-scale fuel performance codes, such as FRAPCON, depend upon an accurate representation of the evolution of the nuclear fuel within the pellet to inform their simulations. The mesoscale methods provide these data as their output. In turn, the mesoscale simulations require input data describing thermodynamics phase stabilities, free energies of equilibrium and non-equilibrium compositions, and

kinetics of the materials. These inputs are usually available from materials databases of phase diagrams and experimental measurements of activated processes, potentially augmented on occasion with data from first principles simulations. For simulations, the initial conditions, the alloy composition and microstructure, nature of the physical domain, its dimensions and boundary conditions are well characterized and directly addressable as part of the mesoscale simulations tools. Furthermore, there are ample analytic predictions of idealized cases and experimental data of real systems of the final state of an evolved material, to serve as validation points for a future application of the simulation capability.

Using a Predictive Capability Maturity Model as an organizing principle for a V&V strategy, one can classify activities with a level of rigor for modeling and simulation (M&S) activities (Oberkampf et al., 2007). The mesoscale work described here is invested in discovery and implementing a model form for mesoscale simulations for nuclear fuels, and laying the foundation for applying the hybrid method for use in future fuel performance simulations. Within the subcontinuum scale, the required level of rigor is modest, appropriate to risk levels with only moderate consequences, but with future intended use to inform risks in higher consequence simulations to model nuclear fuel performance.

Traceability and reproducibility: The collection of V&V evidence must be sufficient to satisfy the level of rigor associated with the activity. The medium level of rigor associated with the current activity requires only a project report and enduring records maintained by the analyst, of the codes and methods used, and of the input and output data used in the simulations. The current report represents such a project report, summarizing the methods and tests used to verify and validate the codes, and input and output files to jobs runs are saved in project-specific directories that are regularly backed up.

Code verification: The first requirement descending from reproducibility and suitability of purpose is code identification, the provenance and successful build of the source code. The mesoscale model framework that is the subject of the report has been implemented as an application style to the open-source Stochastic Parallel PARTicle Kinetic Simulator (SPPARKS) package maintained by Sandia National Laboratories (Plimpton et al., 2009; SPARKS). The SPPARKS code has a number of stochastic simulation capabilities, including the Monte Carlo Potts method. In addition, SPPARKS has been designed to be scalable for large simulations on high-performance computing resources. The new application style for the hybrid Potts-phase field method can be executed in 1, 2 and 3 dimensions. At each site the following variables are used: spin (integer specifying membership in a grain), phase (integer specifying membership in a phase), composition (double precision), along with a neighbor list (integers). Therefore, unlike phase field where additional double precision fields must be added for all grains, this method only requires a single integer field to identify the grain membership at each site.

Specific versions of the SPPARKS code are distinguished by date stamps (rather than version numbers). The starting version used as the foundation for the mesoscale methods development is dated 31 March 2011. The SPPARKS code is a massively-parallel simulator, but here is used in single-processor mode, with a small number of processors on unix/linux-based workstations and with a large number of processors with open-

message passing interface (MPI) environment, with minimal dependence on platform or particular mathematical libraries. The SPPARKS code comes with a test suite, which was executed and it successfully passed.

The new hybrid mesoscale model was implemented upon this verified foundation. Test cases, as described in the next section, were designed to test and verify the performance of each aspect of the newly developed code. Upon completion of the project, the newly developed capabilities will be integrated into the SPPARKS package, in a new release version with its own date stamp, along with new test cases expanding the existing test suite to exercise this new capability. Next, we describe the new modeling framework, and V&V of the new capability in the following section.

2.5.1 Implementation and verification of the hybrid code and framework

Variables and initial implementation: The performance of the hybrid Potts-phase field modeling framework is examined here for a simple two-component, two-phase system. The bulk free energy functional for the system is given by **Equation 2-7** using the following variables: $\lambda = 0.3$, $C_1 = 0.25$, $C_2 = 0.75$, $C_3 = 0.05$, $C_4 = 0.95$, and $a = 0.5$, and is then non-dimensionalized by $k_B T$. The bulk free energy for the two different phases is plotted as a function of composition in Figure 2.1. In this verification test, the exact solution is straightforward: the minimum energy phase for sites with $C \leq 0.30$ is the α -phase, $C \geq 0.70$ is the β -phase, and $0.3 < C < 0.7$ phase separates into the α - and β -phases with compositions $C_\alpha = 0.3$ and $C_\beta = 0.7$ and volume fractions given by tie line calculations. The numerical simulation should converge to this physical description, if it is functioning properly.

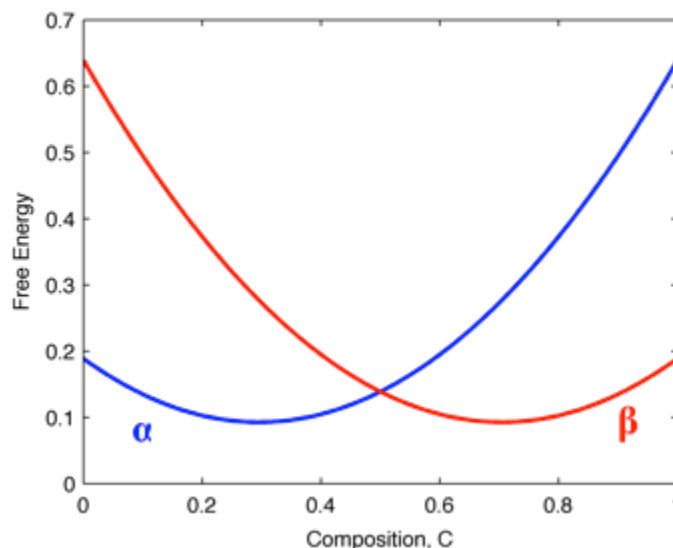


Figure 2.1. Composition-dependent free-energy functional for the two-phase, two-component system studied in this work.

To verify the hybrid interface implementation, we use a simple one-dimensional (1D) system with two grains, each of a different phase at their equilibrium composition. The temperature for the system is set to $k_B T = 0.3$. The initial conditions for the simulation are a sharp interface of the grains, phases and composition. Very quickly, the compositions

transitions from the sharp interface to a smooth, diffuse interface and reaches equilibrium. The equilibrium value of the composition across the grain and phase boundary is illustrated in Figure 2.2. Here it can be seen that the grain and phase boundaries remain sharp, which is to be expected as they are tracked with integer values, while the composition is diffuse, which is to be expected as it is tracked with continuum variables and the term $\kappa_c(\nabla C_i)^2$ must be finite. Furthermore, it is noted that the composition away from the phase boundary remains very close to its equilibrium value for each phase.

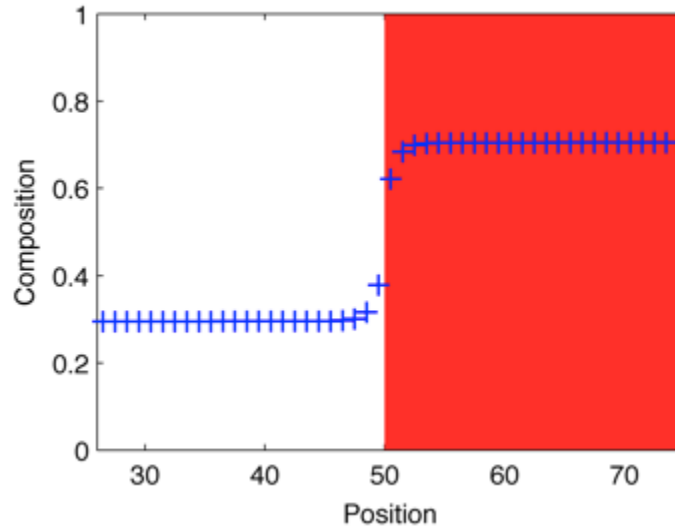


Figure 2.2. Illustration of the simultaneous sharp/diffuse interface of the hybrid model. The two different phase regions of the 1-D model are separated by a sharp interface as denoted by the phase shading, while the composition (symbols) shows a diffuse interface with the composition gradient between the equilibrium compositions of the two phases.

The interfacial energy of the stable interface is calculated to demonstrate both the model capability and the interpretation of units of interfacial energy. By definition, interfacial energy is the excess energy to form a unit area of interface. In this case the interface is between an α -grain and a β -grain. Thus the interfacial energy is calculated here as the difference between the bulk free energy of the α - and β -grains with no interfaces E_{NI} and the total free energy of these two grains forming a interface with area A , E_I . The energies E_I and E_{NI} for this configuration are calculated using **Equation 2-5**. The interfacial energy of the α - β interface is

$$\tilde{\gamma}_{\alpha\beta} = \frac{\tilde{E}_I - \tilde{E}_{NI}}{\tilde{A}} \quad \text{Eq. 2-12}$$

\tilde{A} is the non-dimensional interface area, based on a unit area in 1D, the non-dimensional length in two-dimensional (2D) and the non-dimensional area in three-dimensional (3D). Using **Equation 2-5** to evaluate energy for a single 1D α - β interface at $k_B T = 0.3$ gives $\tilde{E}_I - \tilde{E}_{NI} = 7$. The interfacial energy is then $\tilde{\gamma} = 7$ in non-dimensional units, since both contributing quantities are calculated in non-dimensional units.

Composition Evolution: To verify the kinetics of composition evolution, we evaluate both single-phase and interphase (two-phase) diffusion in 1-D systems with $k_B T = 0.3$ and all other variables as defined in Section 4.1.

The initial condition for the single-phase simulation is a diffusion couple where the composition is defined as a step function in the single-phase, single-grain sample. One portion of the material starts with composition $C = 0.0$ and the other $C = 0.6$, where the equilibrium value for this phase is $C_\alpha = 0.3$. The simulation then evolves by applying the hybrid Potts-phase field model, although the focus here is only on the composition evolution since it is a single-phase, single-grain system. The evolution of the composition field can be seen in Figure 2.3a, where the step function evolves toward a uniform, and equilibrium, value of the composition.

In the present work, the diffusional flux has been defined as

$$J = -M_c \nabla \mu \quad \text{Eq. 2-13}$$

where the conjugate force is the gradient in the chemical potential. Alternatively, one can use the traditional form of Fick's first law to calculate the diffusional flux as

$$J = -D \nabla C \quad \text{Eq. 2-14}$$

where D is the diffusivity and the conjugate force is the gradient in the composition. From this simple definition of the diffusional flux (**Equation 2-14**), Fick's second law can be solved with the error function for simple systems with a step-function composition in 1D. The analytical form for this solution is

$$\frac{C_x - C_o}{C_s - C_o} = 1 - \operatorname{erf}\left(\frac{x}{2\sqrt{Dt}}\right) \quad \text{Eq. 2-15}$$

where C_x is the composition at any given position x and time t , and C_s and C_o represent the values of the step composition before evolution.

Although the composition evolution in the hybrid model is governed by the flux according to **Equation 2-13**, the error function solution (solid line) is in excellent agreement with the simulated results (circles) plotted in Figure 2.3a. The effective diffusivity for the system can be obtained by setting **Equations 2-13 and 2-14** equal and solving for D . Such an exercise results in an effective diffusivity of $\tilde{D} = 7.3$, which perfectly matches the value obtained by fitting **Equation 2-15** to the diffusion results in a single-phase system. The numerical simulations reproduce the analytic result, verifying the correct functioning of this method and its solution.

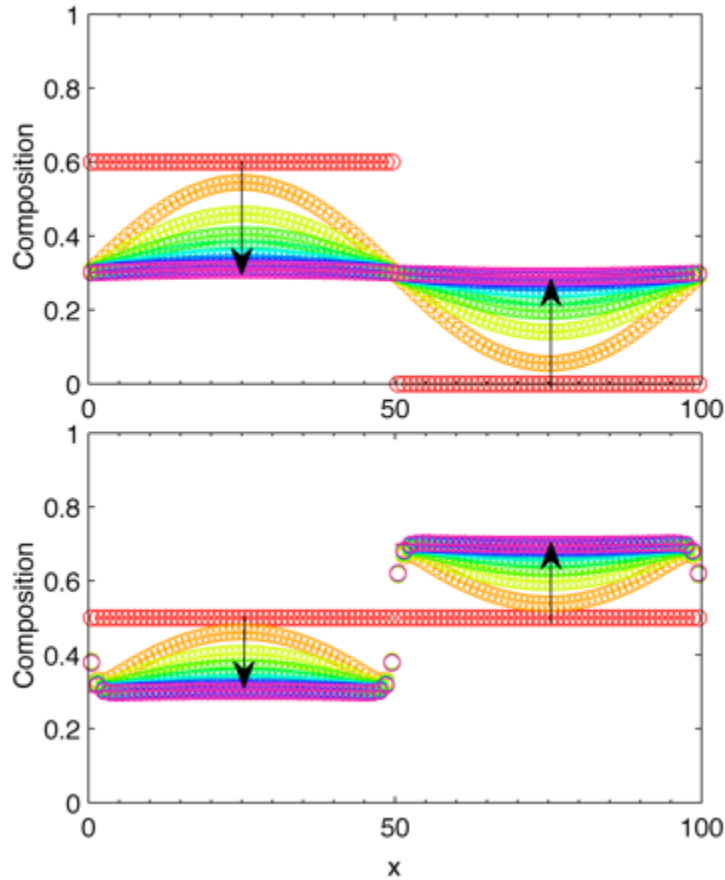


Figure 2.3. Composition evolution in (a) single-phase and (b) two-phase diffusion couples. The system in (a) starts with a step function in the composition with values at 0.0 and 0.6. The system evolves toward the equilibrium composition value of 0.3. The system in (b) starts with a two-phase microstructure all at a composition of 0.5. The system evolves toward the equilibrium compositions, $C_\alpha = 0.3$ and $C_\beta = 0.7$. In both cases the simulation data are open circles and the error function fit to the data is given by the solid line denoting an effective diffusivity value of 2.2.

To evaluate interphase diffusion, we start with a two-phase, two-grain diffusion couple with all sites at the same composition, $C = 0.5$. In this case, microstructure evolution is held stagnant to focus on the composition evolution across the phase boundaries, which can be seen in Figure 2.3b. Once again, the composition in the numerical simulations goes towards its equilibrium values of $C_\alpha = 0.3$ and $C_\beta = 0.7$ and fit the Fickian solution (**Equation 2-15**). In the single-phase diffusion case, the error function fit was perfect over the entire time range, while in the case of interphase diffusion, the error function fit is close but not exact. In close observation, not visible within Figure 2.3b, it can be seen that the error function fit is good at short times with the same diffusivity ($\bar{D} \approx 7.3$) as the single-phase case, but that at longer times, the diffusion in the two-phase cases proceeds more quickly than that predicted by the error function. In other words, the effective diffusivity increases with time for interphase diffusion but this can be explained by the additional terms that result from setting **Equations 2-13 and 2-14** equal. Again, the simulation results are in good agreement with analytically solution, passing this verification test of the model.

Microstructural evolution by grain growth: It is well known that curvature-driven grain growth should obey certain scaling laws. According to these scaling laws, the average grain size, $\langle R \rangle$, is related to time, t , according to

$$\langle R \rangle \propto t^n \tag{Eq. 2-16}$$

where $n = 1/2$ for curvature-driven grain growth in 2D. Here we examine the scaling relationships for both single-phase and two-phase systems in order to gauge the performance of the model two-phase, two-component system and verify the implementation.

Single-phase grain growth is evaluated in a 2D system with 2,000 by 2,000 sites all of a single phase at the equilibrium composition for 80,000 MCS. This has the effect of neglecting the compositional energy contribution, such that the microstructural evolution is driven only by curvature. Several simulations at varying temperatures, $k_B T = 0.0 - 0.5$, were evaluated with the variables defined in section 3.1 and initial conditions of randomly assigned spins to each site from 100 unique spin values. The grain growth curves for these simulations are shown in the log-log plot for average radius and MCS in Figure 2.4a. It is evident that the grain growth is independent of temperature for these ranges and consistently follows the expected scaling ($n = 1/2$) after a short initial transient. Thus, for single-phase microstructures without any composition gradients, the grain growth is curvature driven, as expected, and the numerical simulations are verified to reproduce this very basic phenomenon.

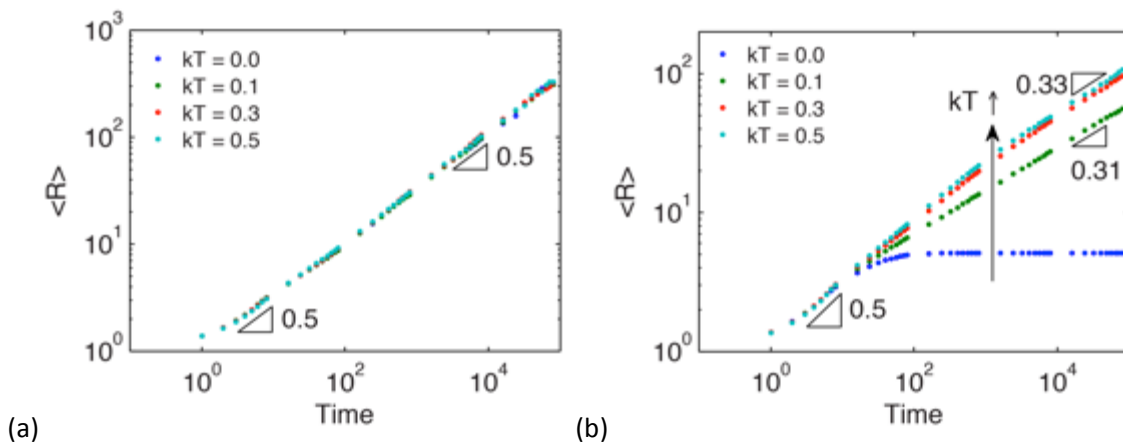


Figure 2.4. Grain growth curves for (a) single-phase and (b) two-phase systems. The single-phase systems have a grain growth exponent of 1/2 for all temperatures while the two-phase system shows stagnation at low temperatures and a grain growth exponent of 1/3 for higher temperatures denoting diffusion-limited grain growth.

When grain growth is not only driven by curvature but also by the reduction in the free energy that is dependent on a number of factors, it is expected that the microstructural coarsening will scale differently than when driven only by curvature. To fully investigate this, several simulations, with varying temperatures, $k_B T = 0.0 - 0.5$, were evaluated for 80,000 MCS. Once again, all the variables for the simulations are defined in Section 4.1 and the sites are initially assigned to random values from 100 unique spin values where

half the spins are α -phase and the other half β -phase. The composition of the α -phase sites is initially set to $C = 0.25$ and the β -phase sites to $C = 0.75$.

The grain growth curves for the two-phase system are plotted in Figure 2.4b. After a brief period of initial coarsening, with a scaling exponent of $n = 1/2$, it can be seen that simulation temperature plays an important part in two-phase grain growth. As seen in Figure 2.4b, at $k_B T = 0.0$, the grain growth becomes completely stagnant. However, at any $k_B T > 0$, grain growth is not stagnant and for $k_B T = 0.3 - 0.5$, the coarsening proceeds with an exponent of $n \cong 1/3$. This suggests that grain growth, when driven by minimization of free energy dependent on both microstructure and composition, requires thermal fluctuations with small excursions from equilibrium composition values in order for grain growth and phase changes to occur. These simulation temperature effects in two-phase systems are well understood (Tikare et al., 2010; Tikare & Cawley, 1998a; Tikare et al., 2001). Finite temperatures are necessary to overcome thermal pinning effects (Holm et al., 1991).

To better understand the actual mechanics of the coupled microstructural-compositional evolution, we examine the simulation at $k_B T = 0.3$ in more detail. Several snapshots of the system over the course of the simulation are given in Figure 2.5 where the grains (spin), phase and composition fields are shown. Grains and phase regions coarsen while maintaining constant phase fraction of $\sim 50\%$. During this coarsening the composition field tracks the phase boundaries closely. It is noted however, that there are no composition gradients at grain boundaries between grains of the same phase. This behavior is expected because the free energy functional defined in **Equation 2-6** is only for a two-phase, two-component system where the composition is only tied to phase and not individual grain boundaries. It is also noted that conservation of mass is achieved in these and all other simulations presented here, a rather basic but necessary verification test.

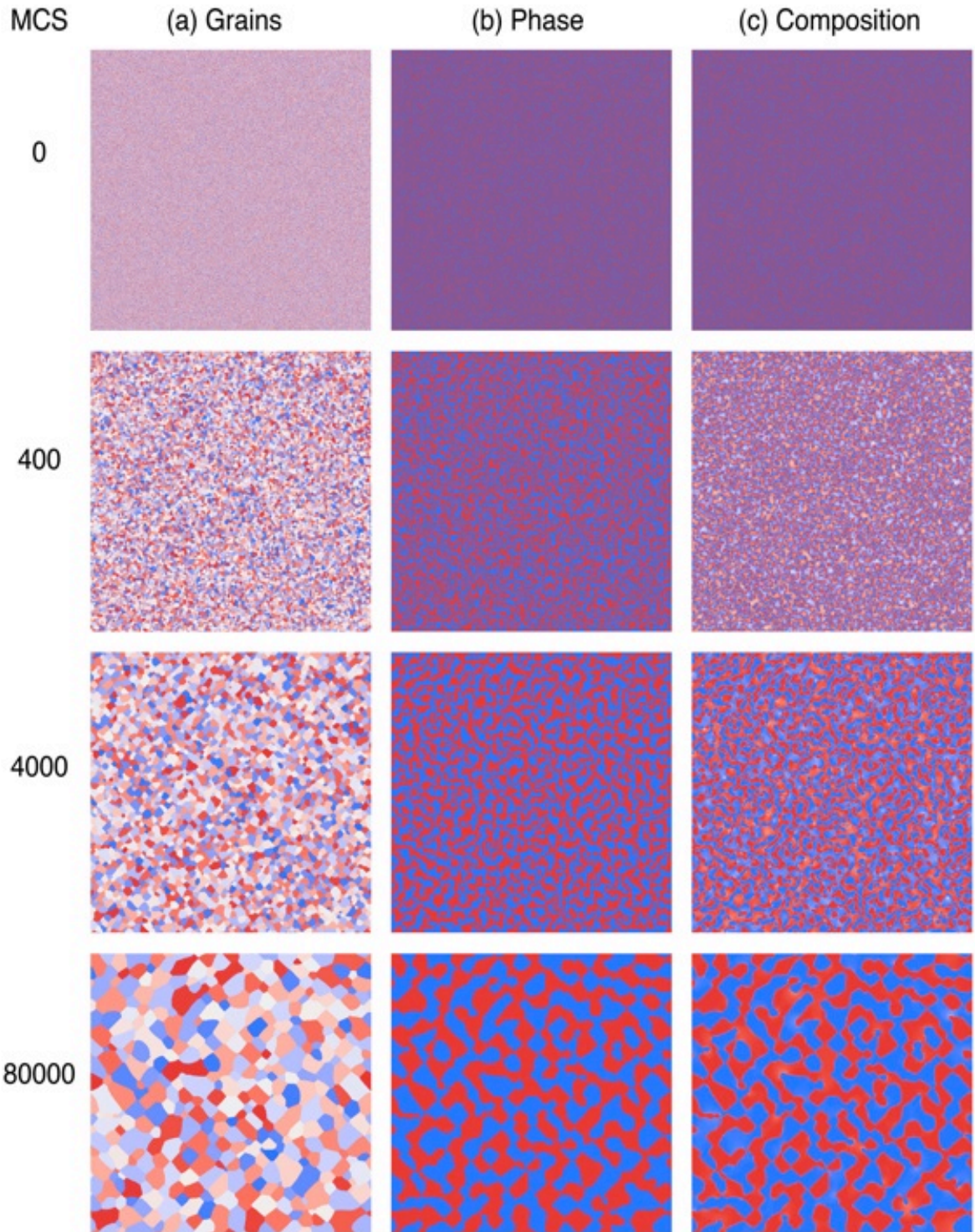


Figure 2.5. Snapshots of the (a) grain structure, (b) phase structure and (c) composition at various times for the two-component, two-phase system. The snapshots show grain and phase coarsening that tracks with the composition map, with each of the phases having compositions near the equilibrium values. α -phase grains, phase membership, and composition range are indicated by shades of blue; β -phase by shades of red.

As mentioned, the composition gradients track the phase boundaries quite closely. In addition, the composition values are close to their equilibrium values inside large phase regions. Both of these characteristics are seen more clearly in Figure 2.6, which plots the composition and phase along a line across the microstructure as indicated by the inset. A clear composition gradient and transition between equilibrium values occurs at each phase boundary. However, some phase boundaries and neighboring regions have composition levels that are above or below the equilibrium value due to the fact that movement of phase boundaries requires the redistribution of the composition and this is a time-dependent process.

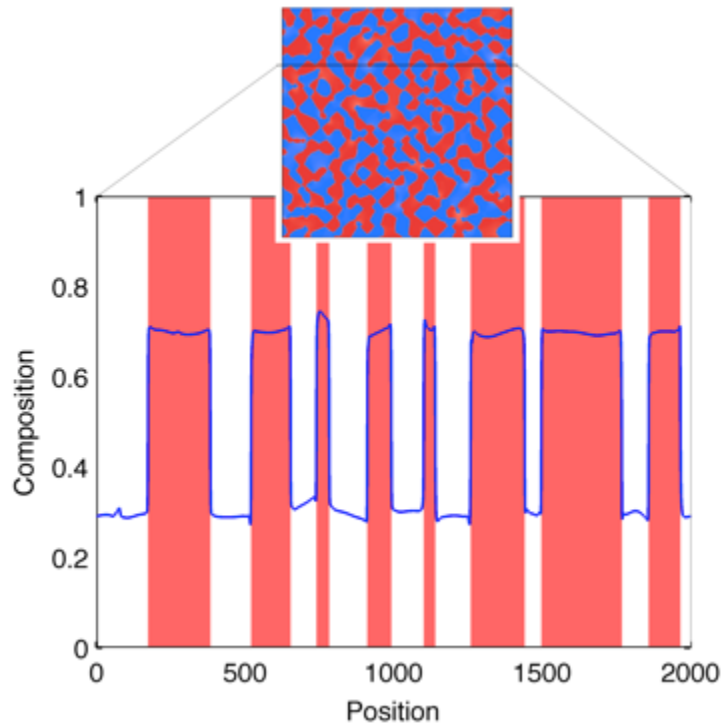


Figure 2.6. Snapshot of the phase and composition through the microstructure at a given position as indicated by the inset. The composition gradients track the phase boundaries quite well, with the individual phases each near their equilibrium composition values of 0.3 and 0.7. Deviations from these values are largely the result of the phase coarsening which necessitates diffusion of the composition such that some areas of the microstructure temporarily deviate from their equilibrium values.

The grains within each phase region grow until they can no longer grow and are pinned by the phase boundary. Taking all this into account, it is clear that the hybrid Potts-phase field model for the two-phase, two-component system shows grain and phase growth that is diffusion limited. This limitation on the coarsening leads to an exponent $n \cong 1/3$ relating the average grain size and time.

To confirm that coarsening in such a system, where grain growth and phase coarsening is driven by the reduction in total interfacial energy, but the kinetics are controlled by long range diffusion, we derive a simple analytic model for the grain growth exponent. This 2D-microstructure can be idealized as shown in Figure 2.7 with the α - and β -phases forming lamellar structures with locally varying curvatures. In this example, the local curvature is proportional to the average grain size, R , within each phase. The solubility of

the B-component in the α -phase and A-component in the β -phase is a function of the local curvature given by the Gibbs-Thomson equation, of which the small number approximation is

$$C_r = C_\infty \left(1 + \frac{2\gamma\Omega_m}{k_B T r} \right) \quad \text{Eq. 2-17}$$

where r is the local radius of curvature, and C_r , and C_∞ are the solubility of the minor component at a surface with radius of curvature r and a flat surface, respectively. γ is the interfacial energy between the two phases and Ω_m is the molar volume. Thus the solubility of A in the β -phase will be higher at the high curvature regions and will diffuse through the β -phase to regions of lower curvature as shown in Figure 2.7. Simultaneously, B will diffuse through α -phase from region of high curvature to those of lower curvature. Due to the symmetry of the free energy functions for the two phases and equality of the mobility values used, the coarsening rate of the two phases will be identical. The diffusion distance is proportional to the average grain size R in these simulations, and the proportionality constant is given as n . The average grain size for both phases is the same as the simulation shown in Figure 2.5, which has 50% of each phase near its equilibrium composition with the same mobilities for all interfaces. Thus, the coarsening of both phases and grain growth within each of the phases will have the same kinetic rates.

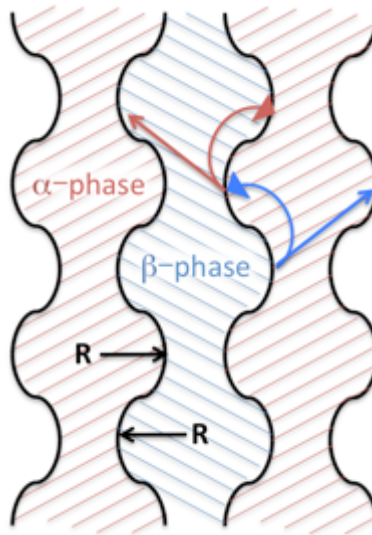


Figure 2.7. Two-phase system illustrating the diffusion of species from high curvature regions to low curvature regions according to the Gibbs-Thomson equation. The higher solubility of the A-component (shown in red) in the β phase (shown in blue) at surfaces of high positive curvature will drive diffusion of A to regions of high negative curvature, where the B-component on the other side is in a region of high positive curvature and is diffusing away. The diffusion kinetics limit the rate of microstructural coarsening.

Grain growth at the phase boundaries will be the limiting factor and this will occur as the flux by diffusion brings mass to the grain surface. Assuming that the grain area in 2D can be approximated by a circle of radius R with equivalent area, the rate of grain growth is

$$\frac{d(\pi R^2)}{dt} = 2\pi R \frac{dR}{dt} = J \cdot A \quad \text{Eq. 2-18}$$

where J is the flux and A is the area of the grain perimeter in 2D where the flux deposits material for grain growth. Assuming that the grains have a constant fraction g of their length as the phase boundary the surface area can be approximated by a circle of equivalent size, $A = 2\pi gR$, where the out-of-plane dimension has a value of 1.

The flux to the grain surface is given by an approximation of Fick's first law (**Equation 2-9**)

$$J = -D \frac{\partial C}{\partial x} = -D \frac{\Delta C}{\Delta x}. \quad \text{Eq. 2-19}$$

The change in concentration ΔC is the difference in solubility between the areas of high curvature and low curvature given by **Equation 2-17**. From the idealized microstructure shown in Figure 2.7, the high curvature areas have radii of curvature that are directly proportional to the grain size, b/R , where b is a proportionality constant. The low curvature areas have the same curvature, but are negative. The distance between the high- and low-curvature areas, Δx , is also proportional to the grain size, R , using the constant m ,

$$D \frac{\Delta C}{\Delta x} = -D \left(\frac{2C_{\infty} \gamma b \left(\frac{1}{R} - \frac{-1}{R} \right)}{mR} \right) = \frac{-4bDC_{\infty} \gamma}{mR^2} \quad \text{Eq. 2-20}$$

By substituting J into the **Equation 2-17** we get

$$\frac{dR}{dt} = \frac{-4bDC_{\infty} \gamma g}{mR^2} \quad \text{Eq. 2-21}$$

which, when integrated, becomes

$$R^3 - R_o^3 = kt. \quad \text{Eq. 2-22}$$

where k is a constant defined as $k = -BDC_{\infty} \gamma$ where B is a constant that consolidates all the geometric constants, g , m , and b . Thus, diffusion controlled grain growth by an Ostwald ripening-type mechanism gives a grain growth exponent of $n = 1/3$ which is consistent with, and verification of, our numerical simulation results.

Phase transformation and nucleation: Phase transformations are often processes in which microstructure and composition cannot be decoupled. Nucleation of a second phase of a different composition followed by its growth is one such phase transformation. The hybrid model framework is well-suited to address these types of problems.

While nucleation events can be simulated by both the Potts model and the phase field model, the hybrid model provides a superior description. In the case of the Potts model, nucleation is simulated directly by introducing a nucleus, by changing a site to a new spin, in a manner consistent with the physical phenomena it is mimicking, (Rollett et al., 1992; Duff & Peters, 2009; Madison et al., 2012). In the case of the phase-field model, nucleation is simulated by introducing random fluctuations, often termed noise. However, these fluctuations are computationally intensive and do not afford direct control over the nucleation event. In contrast, the hybrid Potts-phase field model combines the robust ability of the Potts model to simulate nucleation as an individual site change with the local composition driving the nucleation. In the example presented here, the nucleation and growth of a new phase is simulated to show how phase transformations can be studied with the hybrid model.

The hybrid model has been adapted to simulate nucleation by allowing nucleation events to occur with a prescribed frequency. A nucleation event in this framework attempts a spin change to the new phase at a site. In other words, a certain fraction of the attempted spin changes will change a site's spin from an α -phase to a β -phase or *vice versa*. Growth of the new phase will then be dictated by the microstructural and compositional evolution detailed in previous sections (microstructure and composition evolution by the Potts model and the Cahn-Hilliard equation, respectively and iteratively). Due to the subsequent microstructural evolution, there may be continued growth of the nucleated site or the nucleated site may be consumed by surrounding grains and disappear as an unsuccessful nucleation event.

Nucleation is demonstrated by simulating a case where the two-phase system presented above is quenched to freeze in a non-equilibrium phase and composition. In other words, the simulation was initialized with a super-saturated single-phase microstructure that is far from equilibrium. In fact, the entire simulation starts as tiny, single-site grains of the β phase with a composition of 0.4 as shown in Figure 2.8. The ideal evolution of this simulation would be to nucleate the α phase and then grow the fraction of that phase until each phase achieves its equilibrium composition. Continuing the simulation past complete phase transformation leads to grain growth and phase coarsening.

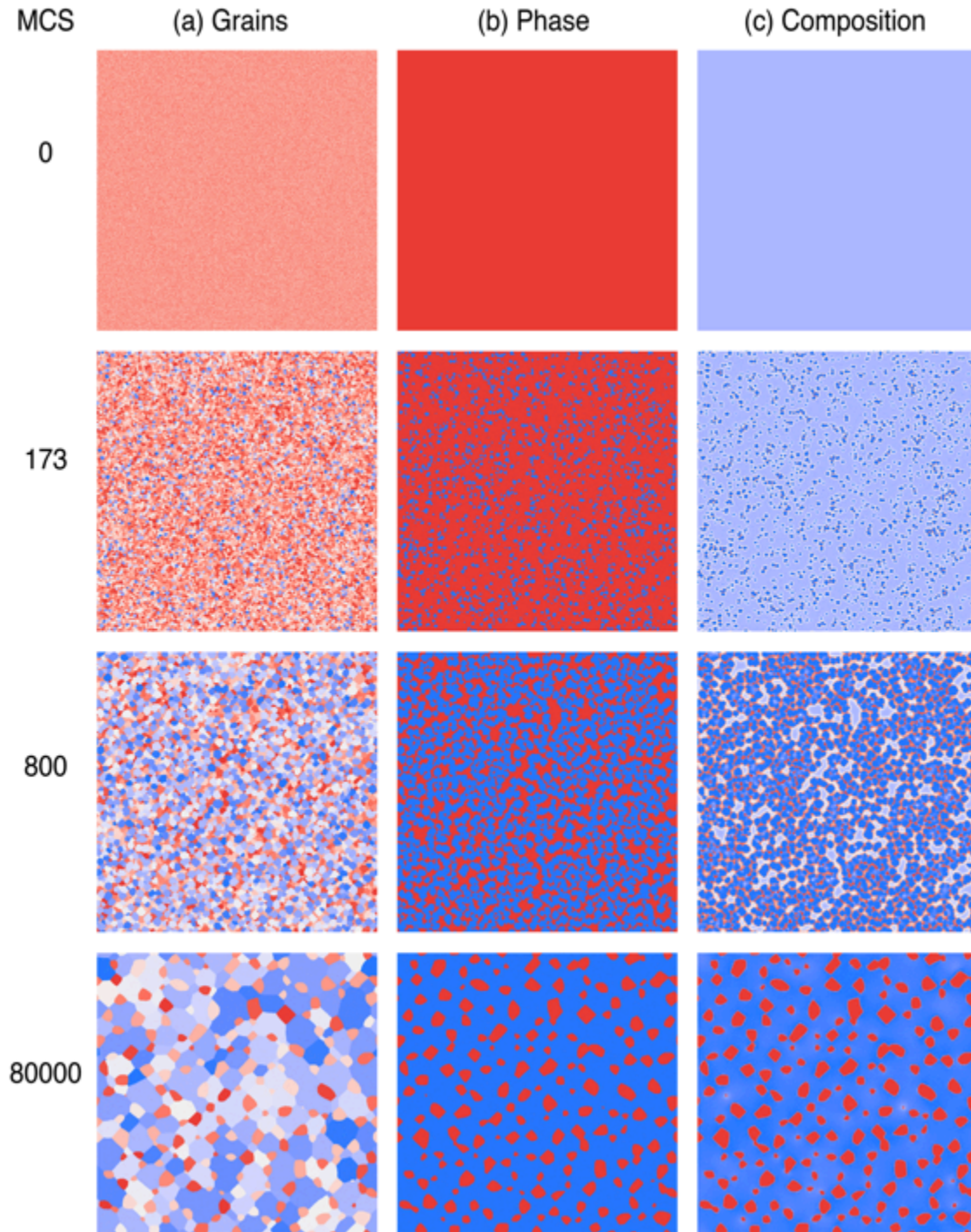


Figure 2.8. Snapshots of the (a) grain structure, (b) phase structure and (c) composition at various times for nucleation and phase transformations in the model two-component, two-phase system. The initial conditions involve a single phase at a compositions far from equilibrium. Nucleation is then prescribed at a given rate that results in the nucleation of the second phase which grows and consumes the majority of the system. α -phase grains, phase membership, and composition range are indicated by shades of blue; β -phase by shades of red.

The nucleation implementation is tested by running a 2D simulation of 2,000 by 2,000 sites for 80,000 MCS. The simulation variables are identical to those defined in section 5.1 with the initial conditions as described above. The nucleation rate for these simulations is set at 0.005 (0.5% of the sites attempt a phase change during each MCS).

The simulation results are shown in Figure 2.8. The grain structure, phase and composition distributions are shown as the simulation progresses. The system starts as one phase with a composition that is not at its equilibrium value. The coloring of the phase matches the coloring of the composition when that phase is near its equilibrium composition. By $t = 173$ MCS, it can be seen that numerous α phase grains have nucleated and have grown to the point that they begin to coalesce to form phase regions. Diffusion in the system quickly brings the α -regions to their equilibrium composition, $C_\alpha = 0.3$. As these α regions change composition from 0.4 to 0.3, they must reject the excess B component to the surrounding neighborhood, allowing the β phase to move towards its equilibrium composition, $C_\beta = 0.7$. In the following snapshot at $t = 800$ MCS, it can be seen that the α phase begins to dominate the microstructure and the remaining β phase is shrinking into smaller regions. Finally, near the end of the simulation, it can be seen that the two phases are very near their equilibrium composition values and the area fraction of the α phase is converging on the expected value of 75%, which is expected from the tie-line construction analysis of the phase diagram.

The combination of the stochastic nucleation with the compositional energetics allows the system to simulate the accurately the phase transformations, satisfying this verification of the model implementation. The system moves towards its lowest energy state, which is a coarsened microstructure with the appropriate volume fractions of a two-phase system with each phase at its equilibrium composition.

Discussion of model verification and validation: The hybrid Potts-phase field modeling framework provides a robust and efficient method to treat coupled microstructural and compositional evolution. Combining the two frameworks allows an efficient treatment of microstructural evolution, when compared with phase field methods, while preserving the detailed description required to track continuum properties, a function not readily available in Potts models. The integrated approach developed here has been implemented into the SPPARKS code. An important aspect of the implementation of the new hybrid model is verification, and the verification of this new capability was described and documented.

The model was systematically verified by incrementally studying each aspect of the coupled diffusion and microstructural evolution process. First the interface and its structure were simulated and characterized, then a simple diffusion couple with known analytical solutions were simulated, grain growth kinetics with the accompanying microstructural features were examined and finally nucleation of the new phase and its subsequent growth, with growth controlled by diffusion, were characterized. All the verification test results showed excellent agreement with analytic solutions. The composition and phase gradient at an infinite interface were characterized by allowing a grain and a phase boundary to come to equilibrium with each other. The interface has the mixed characteristic of a sharp phase boundary characteristic of the Potts model and a diffuse smooth boundary found in the phase field analog. The interfacial energy was

calculated in non-dimensional units and shown to be consistent for such a system. The diffusion across a diffusion couple of different compositions and different phases were compared. Again the agreement of the test simulations with the analytic result, an error function, was excellent. Furthermore, correct treatment of diffusion in different phases was demonstrated by solving the diffusion equation using gradients in chemical potential rather than in composition. The topological characteristics, composition and phase distribution and grain growth in single and two-phase systems were studied. Again, they were verified to perform as expected. The composition had gradients at phase boundaries and not at grain boundaries. The solubility and therefore the gradients were larger in high curvature regions. And, lastly, the grain growth kinetics of the test simulations were correctly consistent with $n = 2$ for curvature-driven grain growth and $n = 3$ for diffusion-controlled grain growth.

As discussed previously, the derivation of free-energy functionals for any phase field system is not a straightforward process. The hybrid framework requires a free-energy functional that pairs the two and derivation of this free-energy functional will require the same expertise as in phase field models. However, the difficulty is decreased somewhat because the microstructural features are completely characterized by a single integer value at each site rather than several phase fields, each of which increases the complexity of the energy functional and the numerical solution. In addition, it is noted that while the free energy functional employed here only couples composition with phase boundaries, it is possible to define a free-energy functional that couples composition with grain boundaries as well.

The application of the hybrid framework to real material systems will require matching thermodynamic and kinetics quantities defined here to those of the real system. In order to do this, the bulk and interfacial energies must be available for the system. The bulk, chemical free energy, E_v , can be defined by analytical or experimental free energy functions. The interface energies defined by γ and κ_c can be matched to experimental measurements of energy and chemical gradients at the interface. The kinetic rates are defined by diffusion coefficients and boundary mobilities, and must be matched for the two methods by fitting both M_c and the rate of grain growth between the two models. Defining these variables will introduce time scale into the simulation. Once all these values are known, the model results should allow accurate simulation of real systems. Validation of the methods here would accumulate from systematic application of the new hybrid framework to multiple real systems and comparisons to experiments, and would, in principle, probe both the fidelity of the physical approximations embodied in the mesoscale approach, and the accuracy of the underlying physical parameters. In future work, applications of the new capability to validation problems and particularly to metallic nuclear fuels would assess the physical uncertainties associated with these simulations. The current report provides the foundation, a verification of the methods and the implemented code, and an understanding of the sources of numerical uncertainties.

In a test of the two-phase grain growth shown here, it was found that while scaling the interface and bulk energies relative to one another did increase or decrease the rate of the microstructural evolution, the grain growth exponent remained the same ($n = 1/3$), indicating that the coarsening remains limited by diffusion in the numerical simulations.

The ability to couple microstructural and compositional evolution into a single framework make the hybrid Potts-phase field model ideal for the study of diffusional phase transformations. The complexity of studying simultaneous microstructural and compositional evolution requires a large number of order parameters to designate different grains and has hindered the number of attempts to do so (Chen, 2002; Fan et al, 1997; Lee et al, 2007). Phase field models have been used extensively to study phase transformations and have done so particularly well (Chen, 2002; Boettinger et al., 2002; Mecozzi et al., 2011; Yamanaka et al., 2008; Singer et al., 2009). However, these typically focus on the diffusional phase transformations in a small volume with very few grains or microstructural features (2 to 10 grains). They do not typically study larger microstructural volumes consisting of many (100 or more) grains. The new hybrid model will combine many of the capabilities of the phase field method with the computational efficiency of the Potts model to simulate the large microstructural networks necessary to better understand phase transformations. Furthermore, as shown in this work, the ability to simulate the nucleation process in the present framework is improved when compared with phase field models, which require indirect nucleation by introducing random fluctuations in the order parameters (Castro, 2003). Nucleation by this method is computationally intensive and affords little control of the nucleation simulation. The Potts model, in contrast, can simulate nucleation very efficiently (Madison et al., 2012), but has difficulty with the compositional dependence. Hence the hybrid model combines the two to give a robust simulation method for nucleation limited by diffusion.

2.6 Summary and Conclusions

The hybrid Monte Carlo Potts-phase field model has been described in detail in this chapter and we have shown that it has the capability to simulate the coupled evolution of microstructure and composition and is well suited to apply to simulate the precipitation of δ -ZrH_{1.5} in Zr-based claddings. The model is efficient because the microstructure is modeled by Monte Carlo Potts methods while the composition is modeled by the phase field method. This efficiency will allow this model to be applied to much larger volumes of claddings than other microstructural models enabling characterization on the engineering scale. The coupling between the microstructure and composition occurs through a free-energy functional that can be extended and modified to capture different phenomena and processes including those that are active in Zr-based claddings. The framework has been incorporated into the open-source SPPARKS code, maintained by Sandia National Laboratories.

The hybrid modeling framework applied to a simple two-phase, two-component system has been verified to capture

- Grain growth and phase coarsening
- Coupling between phase and composition
- Fickian diffusion of species
- Diffusion-limited grain growth
- Phase transformations to a second phase by nucleation and growth of the stable phase from a super-saturated single-phase

The hybrid Potts-phase field modeling framework is efficient, versatile and easily extensible to incorporate different phenomena. The development and implementation of the coupled microstructure-composition mesoscale simulations was accompanied with description of the associated V&V process, consistent with a V&V strategy specifically adapted for subcontinuum scale simulations (Schultz, 2012). The V&V processes described here lay a foundation for applications of the new capabilities to modeling LWR fuels and other metallic alloy systems, with quantitative confidence. For the medium level of rigor demanded of this activity, the V&V process was not onerous, but required capture and documentation of the standard due diligence performed in developing a new physical model at the mesoscale, and mapping onto an appropriately designed V&V strategy. The more strenuous challenges for V&V of the new capability lie ahead, when the new capability is applied to simulations of real material systems such as Zr-based cladding, and the V&V process must provide credible assessments of the uncertainties in the simulations, which must additionally incorporate the physical uncertainties in the methods and the materials data used to inform the model simulations. The adaptation of this model to simulate precipitation of δ -ZrH_{1.5} in Zr-based claddings will be described in the next and the exercises to verify and validate this model will also be presented.

2.7 References

- Allison, J., D. Backman, and L. Christodoulou (2006). Integrated computational materials engineering: A new paradigm for the global materials profession, *JOM* **58**: 25-27.
- Allison, J. (2011). Integrated computational materials engineering: a perspective on progress and future steps, *JOM* **63**: 15-18.
- Anderson, M.P., D.J. Srolovitz, G.S. Grest, P.S. Sahni (1984). Computer-simulation of grain-growth .1. Kinetics, *Acta Metall.* **32**: 783-791.
- Asta, M., C. Beckermann, A. Karma, W. Kurz, R. Napolitano, M. Plapp, G. Purdy, M. Rappaz, and R. Trivedi (2009). Solidification microstructures and solid-state parallels: Recent developments, future directions, *Acta Mater.* **57**: 941-971.
- Boettinger, W., J. Warren, C. Beckermann, and A. Karma (2002). Phase-field simulation of solidification, *Ann. Rev. Mater. Res.* **32**: 163-194.
- Braginsky, M., V. Tikare, and E. Olevsky (2005). Numerical simulation of solid state sintering, *International Journal of Solids and Structures* **42**: 621-636.
- Castro, M. (2003). Phase-field approach to heterogeneous nucleation, *Phys. Rev. B* **67**: 035412.
- Chen, L.Q. (2002). Phase-field models for microstructure evolution, *Ann. Rev. Mater. Res.* **32**: 113-140.
- Du, Q., W.J. Poole, M.A. Wells, and N. Parson (2011). Microstructural modeling of the homogenization heat treatment for AA3XXX alloys, *JOM* **63**: 35-39.
- Duff, N., and B. Peters (2009). Nucleation in a Potts lattice gas model of crystallization from solution, *J. Chem. Phys.* **131**: 184101.
- Emmerich, H. (2003). *The Diffuse Interface Approach in Materials Science*. Berlin: Springer-Verlag.

- Fan, D.N., and L.Q. Chen (1997). Diffusion-controlled grain growth in two-phase solids, *Acta Mater.* **45**: 3297-3310.
- Grest, G., M. Anderson, D. Srolovitz, and A. Rollett (1990). Abnormal grain-growth in 3-dimensions, *Scripta Metall. Mater.* **24**: 661-665.
- Hassold, G., I. Chen, and D. Srolovitz (1990). Computer-simulation of final-stage sintering .1. Model, kinetics, and microstructure, *J. Am. Ceram. Soc.* **73**: 2857-2864.
- Holm, E., J. Glazier, D. Srolovitz, and G. Grest (1991). Effects of lattice anisotropy and temperature on domain growth in the 2-dimensional Potts-model, *Phys. Rev. A* **43**: 2662-2668.
- Holm, E. A., and C. Battaile (2001). The computer simulation of microstructural evolution, *JOM* **53**: 20-23.
- Holm, E. A., G. Hassold, and M. A. Miodownik (2001). On misorientation distribution evolution during anisotropic grain growth, *Acta Mater.* **49**: 2981-2991.
- Holm, E. A., M. Miodownik, and A. Rollet (2003). On abnormal subgrain growth and the origin of recrystallization nuclei, *Acta Mater.* **51**: 2701-2716.
- Humphreys, F. J., and M. Hatherly (2004). *Recrystallization and Related Annealing Phenomena*. Oxford: Elsevier.
- Janssens, K. G. F., D. Raabe, E. Kozeschnik, M. A. Miodownik, and B. Nestler (2007). *Computational materials engineering: an introduction to microstructure evolution*. Boston: Elsevier Academic Press.
- Lee, S.-B., J. M. Rickman, and A. D. Rollett (2007). Three-dimensional simulation of isotropic coarsening in liquid phase sintering I: A model, *Acta Mater.* **55**: 615-626.
- Madison, J. D., V. Tikare, and E. A. Holm (2012). A hybrid simulation methodology for modeling dynamic recrystallization in UO₂ LWR nuclear fuels, *J. Nucl. Mater.* **425**: 173-180.
- Mecozi, M. G., J. Eiken, M. Apel, and J. Sietsma (2011). Quantitative comparison of the phase-transformation kinetics in a sharp-interface and a phase-field model, *Computational Materials Science* **50**: 1846-1853.
- Miodownik, M., J. Martin, and A. Cerezo (1999). Mesoscale simulations of particle pinning, *Philos. Mag. A* **79**: 203-222.
- Miodownik, M., E. Holm, and G. Hassold (2000). Highly parallel computer simulations of particle pinning: Zener vindicated, *Scripta Mater.* **42**: 1173-1177.
- Nestler, B., and A. Wheeler (2000). A multi-phase-field model of eutectic and peritectic alloys: numerical simulation of growth structures, *Physica D* **138**: 114-133.
- Oberkampff, W.L., M. Pilch, and T. G. Trucano (2007). *Predictive Capability Maturity Model for Computational Modeling and Simulation*. SAND Report 2007-5948. Albuquerque, NM: Sandia National Laboratories.
- Olmsted, D. L., D. Buta, A. Adland, S. M. Foiles, M. Asta, and A. Karma (2011). Dislocation-pairing transitions in hot grain boundaries, *Phys. Rev. Lett.* **106**: 046101.

- Plimpton, S. J., C. Battaile, M. Chandross, E. A. Holm, A. Thompson, V. Tikare, G. Wagner, E. Webb, and X. Zhou. *Crossing the Mesoscale No-Man's Land via Parallel Kinetic Monte Carlo*. Sandia Report: 2009-6226, Albuquerque, NM: Sandia National Laboratories.
- Raabe, D. (2000). Scaling Monte Carlo kinetics of the Potts model using rate theory, *Acta Mater.* **48**: 1617-1628.
- Rollett, A. D., M. J. Luton, and D. J. Srolovitz (1992). Microstructural Simulation of Dynamic Recrystallization, *Acta Metall. Mater.* **40**: 43-55.
- Rollett, A., D. Srolovitz, and A. Karma (2002). Editorial: Microstructural evolution based on fundamental interfacial properties, *Interface Science* **10**: 119-119.
- Schultz, P. A. (2012). *Subcontinuum-scale Verification and Validation Strategy*, SAND Report 2012-9257, Albuquerque, NM: Sandia National Laboratories.
- Singer, H. M., I. Singer, and A. Jacot (2009). Phase-field simulations of alpha -> gamma precipitations and transition to massive transformation in the Ti-Al alloy, *Acta Mater.* **57**: 116-124.
- SPPARKS website: <http://spparks.sandia.gov/>
- Steinbach, I. (2009). Phase-field models in materials science, *Model. Simul. Mater. Sc.* **17**: 073001.
- Tikare, V., and J. Cawley (1998a). Numerical simulation of grain growth in liquid phase sintered materials - I. Model, *Acta Mater.* **46**: 1333-1342.
- Tikare, V., and J. Cawley (1998b). Numerical simulation of grain growth in liquid phase sintered materials - II. Study of isotropic grain growth, *Acta Mater.* **46**: 1343-1356.
- Tikare, V., M. Miodownik, and E. Holm (2001). Three-dimensional simulation of grain growth in the presence of mobile pores, *J. Am. Ceram. Soc.* **84**: 1379-1385.
- Tikare, V., M. Braginsky, and E. Olevsky (2003). Numerical simulation of solid-state sintering: I, sintering of three particles, *J. Am. Ceram. Soc.* **86**: 49-53.
- Tikare, V., M. Braginsky, D. Bouvard, and A. Vagnon (2010). Numerical simulation of microstructural evolution during sintering at the mesoscale in a 3D powder compact, *Computational Materials Science* **48**: 317-325
- Tonks, M. R., D. Gaston, P. C. Millett, D. Andrs, and P. Talbot (2012). An object-oriented finite element framework for multiphysics phase field simulations, *Computational Materials Science* **51**: 20-29.
- Wu, F. Y. (1982). The Potts-model, *Rev. Mod. Phys.* **54**: 235-268.
- Wu, K.-A., A. Adland, and A. Karma (2010). Phase-field-crystal model for fcc ordering, *Phys. Rev. E* **81**: 061601.
- Yamanaka, A., T. Takaki, and Y. Tomita (2008). Multi-phase-field modeling of diffusive solid phase transition in carbon steel during continuous cooling transformation, *J. Crystal Growth* **310**: 1337-1342.

3. ADAPTION OF HYBRID POTTS-PHASE FIELD MODEL TO SIMULATE δ -ZrH_{1.5} PRECIPITATION IN Zr-BASED CLADDINGS

The objective of this model is to predict the precipitation and reorientation of hydride precipitates in Zr-based claddings of used fuel rods after removal from cooling pools and drying during an indeterminately long period of dry-storage. The hybrid Potts-phase field model is ideally suited for simulation of δ -ZrH_{1.5} precipitation in α -Zr matrix as it captures the two dominant features of this phase transformation. The model can simulate microstructural evolution accompanying a phase transformation, which occurs, by nucleation and growth as well as the composition evolution of a diffusive phase transformation with diffusion-controlled kinetics. Furthermore, the model can simulate a sufficiently large volume with the ability to resolve individual precipitates to obtain engineering-scale behavior of the hydride precipitation. While the basic model has been developed and validated, it must be further developed and adapted to simulate the details of δ -ZrH_{1.5} precipitation in an α -Zr matrix with the thermodynamic, kinetics and crystallographic details specific to this materials system. This chapter will describe the development and modification made to the hybrid model, and justify the need for the modifications.

The exact process to be simulated is the precipitation of hydrides following the drying cycle. The regulatory temperature limit for drying the fuel is 400°C. For the purposes of simulations, we assume that the drying temperature will be this regulatory limit, but this is easily modified to any drying temperature in the simulations that are specific to a particular cladding type. Following the drying cycle the temperature immediately drops and then decays very slowly over many months and years. Hansen (2012) estimated the temperature profile of a fueled cladding by analyzing the heat conduction in a two-dimensional cylinder. He assumed the drying temperature was 400°C. The temperature profile he obtained is shown in Figure 3.1, a plot of the cladding temperature starting from the end of the drying cycle when dry storage begins. As one can see as soon as the drying cycle is terminated, the temperature drops very quickly to approximately 320°C and then gradually decays over a period of years. For demonstration purposes, we simulate this condition by starting the simulation at 400°C, drop the temperature immediately to 300°C. At this point, the zirconium matrix is supersaturated with hydrogen. The temperature is held constant at 300°C while the hydrides precipitate. The development of the hybrid model to simulate a variety of claddings with variation in their composition and microstructures over the temperature range of interest is described in this chapter.

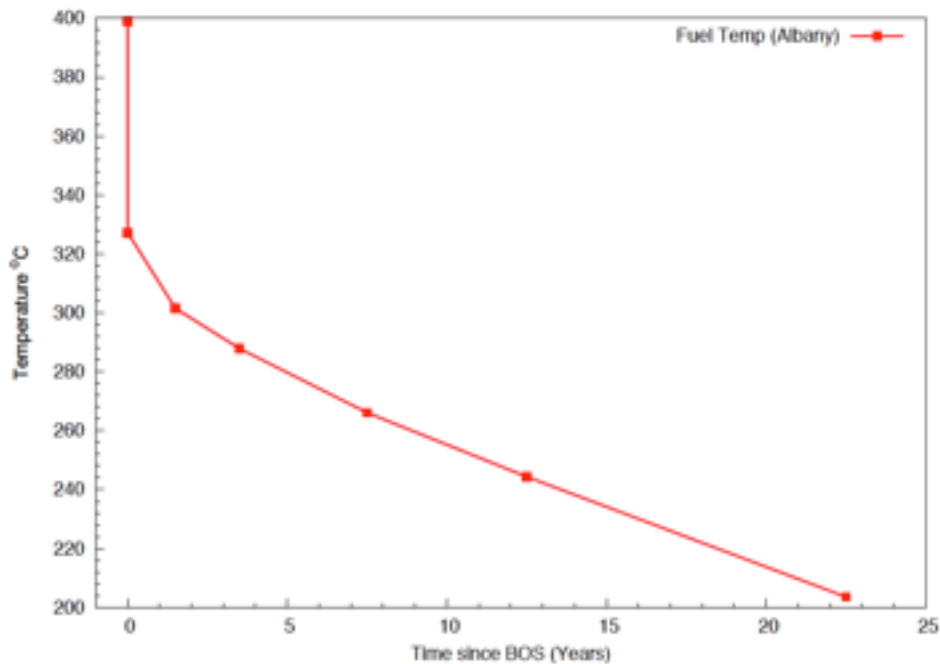


Figure 3.1. Estimated cladding temperature after drying during dry-storage (Hansen, 2012).

3.1 Zirconium-Based Cladding Composition and Microstructure

The model must capture the underlying microstructure with detailed representation of the grain structure, defect distribution and composition of the zirconium claddings as they are critical features of the hydride formation and reorientation behavior. The hydride orientation and morphologically characteristics have, in turn, been shown to have a large influence on the fracture behavior of clads (Kearns & Woods, 1966; Bai et al., 1994a; Bai et al., 1994b). Thus it is important to know the microstructure including the grain size and shape, grain shape texture, crystallographic texture, the type and number of defects, and the organization and distribution of defects. It has been shown by many that microstructure of zirconium alloys is a function of the alloy composition and the fabrication process from ingot to rolling and the subsequent heat treatments (Kearns & Woods, 1966; Chauvy et al., 2006). Figure 3.2 illustrates the wide range of Zircaloy-2 grain sizes and shapes that are obtained at different hot-rolling conditions (Chakravarty et al., 2010). These microstructures are of the alloy before heat treatments for recovery, recrystallization or stress annealing (Humphreys & Hatherly, 2004). It is expected that these anneals will result in further changes to the microstructure. Recovery is the process by which dislocation move and tangle to form cell walls within grains. The interior regions of the recovered cells have a much lower density of dislocations with small misorientation angles between neighboring cells. Recrystallization is the process of nucleating new defect free grains that grow and consume the highly worked, highly deformed grains after hot rolling with the recovered cell structures serving as the nuclei. Thus recrystallization typically results in smaller grains that may or may not be equiaxed depending on the particular nucleation conditions. Stress annealing typically does not

result in significant change to the microstructure as no new grains are formed. There may be some grain growth, but the primary effect of annealing is to relieve some of the stress at a temperature where some diffusive processes become active. Since the model must be sufficiently versatile to simulate hydride precipitation in a variety of Zr-based matrices, this section will very briefly review the variation in Zr-based claddings and conclude by describing and demonstrating the incorporation of a particular Zircaloy-4 cladding.

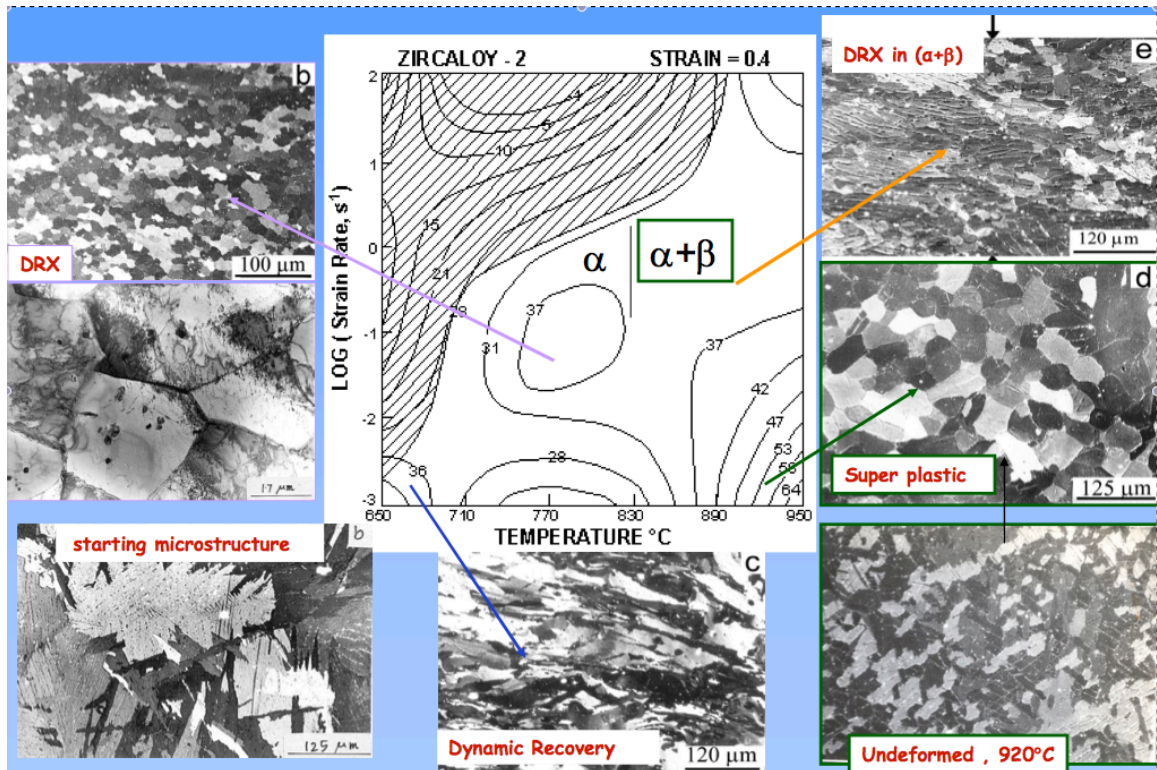


Figure 3.2. A wide range of grain sizes and shapes are obtained depending on the hot-rolling temperature and strain rate used to form Zircaloy-2 claddings (Chakravartty et al., 2010).

The current stockpile of used fuel is clad by a number of different zirconium alloys. Boiling water reactor fuels rods are clad with Zircaloy-2 fully recrystallized (RXA) or Zircaloy-2 stress relief annealed (SRA) and pressure water reactors with Zircaloy-4 SRA, Zirlo™ SRA, Zirlo™ partially recrystallized (pRXA) or M5™ RXA (Geelhood and Byere, 2012). Zircaloy-4 has reduced Fe and Ni to reduce oxidation and thus limit H-pickup by the clad. There is some data to indicate that reducing Ni in Zircaloy-4 does not change oxidation behavior, but does reduce H-pickup (Sabol, 2005). The alloy composition of these claddings is given in Table 3.1.

Table 3.1. Alloy composition given in weight % (Whitmarsh, 1962; Allegheny Technologies; Natesan & Soppet, 2004)

	Sn	Fe	Cr	Ni	Nb	Zr	Impurities
Zircaloy-2	1.2 -1.7	0.07-0.2	0.05-0.15	0.03-0.08		Bal.	Al,B,C,Cd,Co, Cu,H,Hf,Pb, Mg,Mn,N,Si, Na,Ti,W
Zircaloy-4	1.2-17	0.12-0.18	0.05-0.15	<0.007		Bal.	Same as Zr-2
Zirlo™	0.7 to 1.0	0.11	<0.01		1.0		C,O,H,Hf, N,Si,Ta,W
M5™					0.8 to 1.2		

The underlying microstructure of the fresh claddings is generally not available. The pilgering process used to form claddings imparts large amounts of strain with the associated dislocations and other defects rendering ineffective the traditional metallographic and etching techniques used to delineate grain boundaries (Danielson & Sutherlin, 2004). Thus very little data about Zr-based cladding microstructure, particularly grain size and shape is available. Some information about the grain size and texture can be indirectly obtained from some works that characterize other properties such as fatigue (Lin & Haicheng, 1998), hydride embrittlement (Bai et al., 1994a), hydride precipitation (Bai et al., 1994b) super plasticity (Garde et al., 1978) and swelling (Murgatroyd & Rogerson, 1980) as a function of microstructure. Lin and Haicheng (1998) report on fatigue characteristics of fresh, unirradiated or hydrided Zircaloy-4 SRA and show scanning electron microscopy (SEM) and transmission electron microscopy (TEM) micrographs. From these micrographs the grain size of Zircaloy-4 appears to be approximately 8 to 10 μm as shown in Figure 3.3. More recently, electron backscatter diffraction and related techniques have yielded some data on cladding microstructures (Qin et al., 2011; Kiran Kumar et al., 2010; Santisteban et al., 2010; Abe & Furugen, 2010). These show a slightly elongated grain structure in the rolling direction (RD) with a nominal grain size of approximately 10 μm in that direction. One of the better examples found in the literature is shown below in Figure 3.4. Characterization of this image and other examples found showed an average elongation of approximately 2 \times in the RD as compared to the normal- and transverse-directions.



Figure 3.3. SEM of fatigued Zircaloy-4 (Lin & Haicheng, 1998).

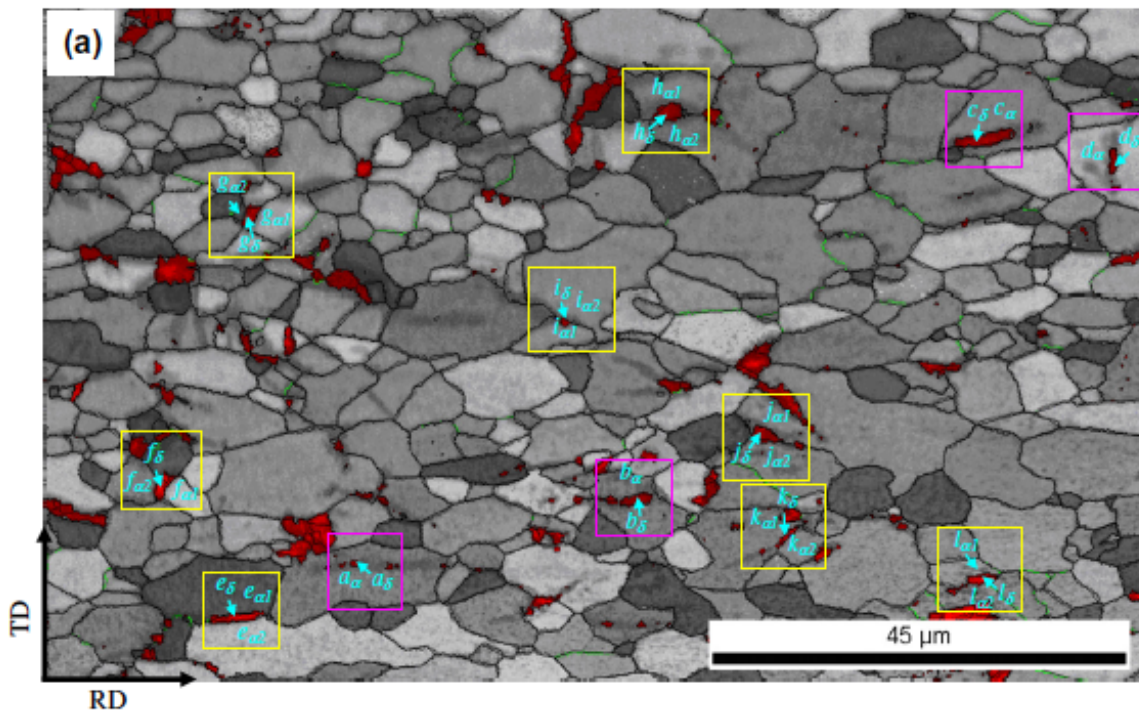


Figure 3.4. Electron backscatter diffraction (EBSD) image showing a typical grain structure of Zircaloy-4 (Qin et al., 2011).

The pilgering process used to form Zr-based claddings, imparts not only grain shape texture, but also crystallographic texture as the rolling processes compress the sheet in the normal direction (ND) and constrain it in the transverse direction (TD) so that the basal poles tend to be parallel to the ND. Much more data exists on the crystallographic texture of Zircaloy-4 as X-ray and neutron diffraction are effective method to obtain these and the highly worked nature of claddings does not distort these data or interfere with texture measurements. Furthermore, these data are sufficiently quantified to implement into

synthetically generated microstructures. Crystallographic texture is described by Kearns numbers for the three principal directions in the Zircaloy samples, i.e., f_N (normal), f_T (transverse) and f_R (rolling), defined as a weighted average of the intensity of the basal plane normals oriented with respect to the sample's principal direction; the sum of the Kearns number is $f_N + f_T + f_R = 1$. Kearns numbers calculated from orientation distribution function (ODF) texture data obtained at 100°C by neutron diffraction for as-manufactured Zircaloy-4 are: $f_N = 0.54$, $f_T = 0.28$ and $f_R = 0.18$ (Fong, 2013). These values are in close agreement with the Kearns numbers for as-received Zircaloy-4 determined earlier by Coleman and coworkers (Coleman et al., 2010) using X-ray diffraction methods, i.e., $f_N = 0.56$, $f_T = 0.29$ and $f_R = 0.15$ for Atucha claddings and $f_N = 0.65$, $f_T = 0.30$ and $f_R = 0.05$ for Ziratec claddings.

Although the 3D strain history of fabrication will ultimately play a role in their texture and properties and the subsequent formation of oriented hydrides within the Zr matrix (Kearns & Woods, 1966; Louthan & Marshall, 1963; Marshall, 1967), the similarity between Kearns numbers strongly suggests that all these Zircaloy-4 claddings have the same type of texture. X-ray and electron back-scattering diffraction studies (Kiran Kumar et al., 2010), as well as neutron scattering investigations (Fong, 2013; Wang et al., 2013), have shown that typical cold-worked and stress-relieved or hot-rolled and annealed Zircaloy-4 claddings are characterized by a strong (0002) basal plane texture, with double pole maxima inclined typically by ca. $\pm 30^\circ$ from the ND and extended along the TD, while a preferential {10-10} prismatic orientation is seen along the RD as shown in Figure 3.5. The basal pole orientation of Zircaloy-4 appears to differ only slightly with manufacturing process variables such as the number of cold reductions and intermediate anneals (Fong, 2013).

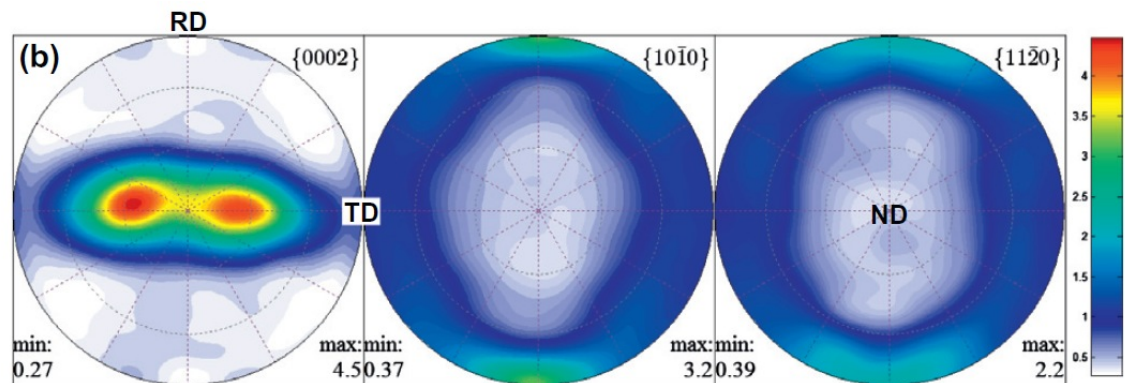


Figure 3.5. Texture of a hot-rolled and annealed Zry-4 plate represented by experimental basal {0002} and prism {10-1 0} and {11-2 0} pole figures, with the rolling direction (RD), transverse direction (TD) and normal direction (ND) indicated (Wang et al., 2013).

Other evidence to show that texture in the different Zircaloy-4 claddings is similar is the Hill numbers. From the ODF texture data, the three mechanical tensile anisotropic factors proposed by Hill (Hill, 1948) and designated as F , G , and H can be derived. For isotropic materials, $F = G = H = \frac{1}{2}$. Fong (Fong, 2013) determined Hill's anisotropy factors from the neutron-diffraction ODF of as-manufactured Zircaloy-4: $F = 0.76$, $G = 0.54$ and $H = 0.20$. Hunt and Newell (Hunt, 1975; Hunt & Newell, 1979), reported very similar Hill's numbers for the Zircaloy-4 that they examined: $F = 0.76$, $G = 0.56$ and $H = 0.18$.

In addition to the basic grain structure of Zr-based claddings, the composition can be varied with many alloying elements. The role of other alloying elements, Sn, Ni, Fe, Nb and Cr shown in Table 3.1, is not well understood. At the low levels added in zirconium alloys, Sn (Abriata et al., 1983) form a solid solution with Zr so to a first approximation, we can assume that it does not affect the hydriding behavior significantly. Likewise, Fe (Pelton et al., 1983; Okamoto, 2006) also forms a solid solution with Zr at level < 0.70 wt% and so to a first approximation we will neglect its effect on hydride formation. Similarly, Cr (Okamoto, 1993) and Ni (SGnucl-SGTE, 2004) form solutions with Zr. While each of these additions individually forms a single phase solid solution with Zr, when added in combinations their phase equilibria compositions are less clear. Zircaloy-2 and Zircaloy-4 are known to form Laves phases, $ZrFe_2$ and $ZrCr_2$ (Perez, 2006), two polymorphs of $ZrCr_2$ (Krasevec, 1981) and ternary phases such as $Zr(Cr,Fe)_2$ (Van der Sande & Bement, 1974) and $Zr_2(NiFe)$ (Chemelle et al., 1983; Arias et al., 1987) although their binary phase equilibrium diagrams suggest otherwise. These precipitates are small with sizes of couple 100 nm. Nb additions to ZirloTM and M5TM are known to exceed the solubility limit and form other phases (Okamoto, 1992; Hari Kumar et al., 1994). Characterization of microstructure and phases in the Zr-Nb-Fe system with some O present show the existence of $Zr(Nb,Fe,Cr)_2$ and $(Zr,Nb)_4Fe_2$ (Barberis et al., 2004). Zr with 1.2 to 0.35 wt% Sn-Nb-Fe form a Laves phase $Zr(Nb,Fe)_2$ and other phases such as $(Zr,Nb)_2Fe$ and $(Zr,Nb)_2(Fe,Nb)$ depending on the its time-temperature history (Shishov et al, 2005). The Zr with 0.05 to 1.0 wt% Sn-Nb-Fe-Cr alloy system has been shown to have $Zr(Fe,Cr)_2$ and Zr-Nb-Fe precipitates (Liu et al., 2005). Finally Motta et al. have compiled a list of precipitates found in several Zr alloys showing a variety of precipitates depending on the exact alloy composition (Motta et al., 2007). Their data are shown in Table 3.2. In summary, there is a vast amount of data on the phases formed by a variety of zirconium alloys, particularly Zircaloy-2 and Zircaloy-4. However, the majority is not direct studies of phase equilibrium or phase stability. The majority of the data is supporting characterization of other properties. The challenge is compiling these data and reducing them to materials characteristics of the different phases at different compositions for use in predictive models.

Table 3.2. Zr-based alloys with the precipitates found in them characterized by Motta and co-workers (Motta et al., 2007)

Alloy system	Composition (wt%)	Precipitate Crystal structure
Zr-Nb	x=0.2, 0.4, 1.0, 1.5, 2, 5%	<i>hcp</i> Zr(Nb,Fe) ₂ , <i>bcc</i> β-Nb and orthor Zr ₃ Fe, except Zr0.2Nb, Where no precipitates are present and only minor peaks in Zr0.4Nb
ZrNbSn ZrSn	Zr0.4Nb0.4Sn and Zr0.4Nb0.2Sn Zr0.4Sn, Zr1.2Sn	Similar to 0.4Nb No precipitates
Zr-Fe-Cr	Zr-0.4Fe-0.2Cr and Zr-0.2Fe-0.1Cr (two processing temperatures: 580°C (L) and 720°C (H)) Zr-1.0Fe-0.5-Cr Zr0.6Fe-0.3Cr	Cubic C15 (low processing Temperature) and hex. C14 (high processing temperature) Zr(Cr,Fe) ₂
Zr-Cr-Fe	Zr0.5Cr, Zr-0.5Cr-0.2Fe, Zr-1.0Cr, Zr-1.0Cr-0.2Fe	Cubic ZrCr ₂ and cubic Zr(Cr,Fe) ₂
Zr-Fe-M	Zr-0.6Fe Zr0.6Fe-0.6Nb Zr0.6Fe-0.3Mo Zr1.0Fe	Othor. Zr ₃ Fe β-Nb + <i>hcp</i> ZrNbFe Cubic ZrMo ₂ and Ortho Zr ₃ Fe Ortho. Zr ₃ Fe
Zr-Cr-M	Zr-1.0Cr-0.5Fe Zr1.0Cr-0.5Mo	C14 hex. Zr(Cr, Fe) ₂ Cubic ZrCr ₂
Zr-Cu-Mo	Zr-0.5Cu, Zr -0.5Cu-0.5Mo Zr-1.0Cu, Zr-1.0Cu-0.5Mo	Tet. Zr ₂ Cu and cubic ZrMo ₂ when Mo present
Reference Alloys	Sponge Zr, Crystal bar Zr, Zircaloy-4	No precipitates for pure Zr <i>hcp</i> c14 Zr(Cr,Fe) ₂ for Zircaloy-4

3.1.1 Generating a Digital Microstructure

The assumption made in this work is that the underlying grain structure of the clad is not significantly altered by the relatively low temperatures that it experiences after fuel rod fabrication. This is a well-founded assumption and if necessary can be easily tested experimentally; however, during normal operation, the cladding is not expected to experience temperatures higher than 350°C and the regulatory temperature limit during drying after removal from spent fuel pools for cooling is 400°C. Even if off-normal conditions subject the cladding to temperatures as high as 500°C, no grain growth, recovery, recrystallization or other microstructural evolution is expected to occur. The defects formed by neutron irradiation during in-pile service may be modified and will be the topic of a later section (reference section). Thus, we use the as-fabricated grain structure and texture, and crystallographic texture for the cladding microstructure during long-term dry storage.

Two methods to generate the grain size and shapes were used. The first was using the Potts model and the second a software package, Dream3D (Jackson, 2013). The standard Potts model, described in detail in other works (Holm & Battaile, 2001; Holm et al., 1991), was used to generate a topologically-correct, equi-axed 3D grain structure by performing grain growth simulations. This equi-axed grain structure was numerically elongated in the RD so that grains were 2x longer in the RD as shown in Figure 3.6a. The other method used a Dream3D, a free open and modular software package that allows users to construct microstructures digitally as shown in Figure 3.6b. The rolled synthetic microstructure had an average grain size of 10 μm with a standard deviation of 1μm. While there are little data on grain size, there is even less information on grain size distributions and their standard deviations. Thus, the choice of standard deviation is estimated from existing knowledge of rolled metals. The average elongation in the rolled direction of the synthetic microstructure is also 2× as compared to the transverse and NDs; this is based on simple measurements of the microstructures from the published literature.

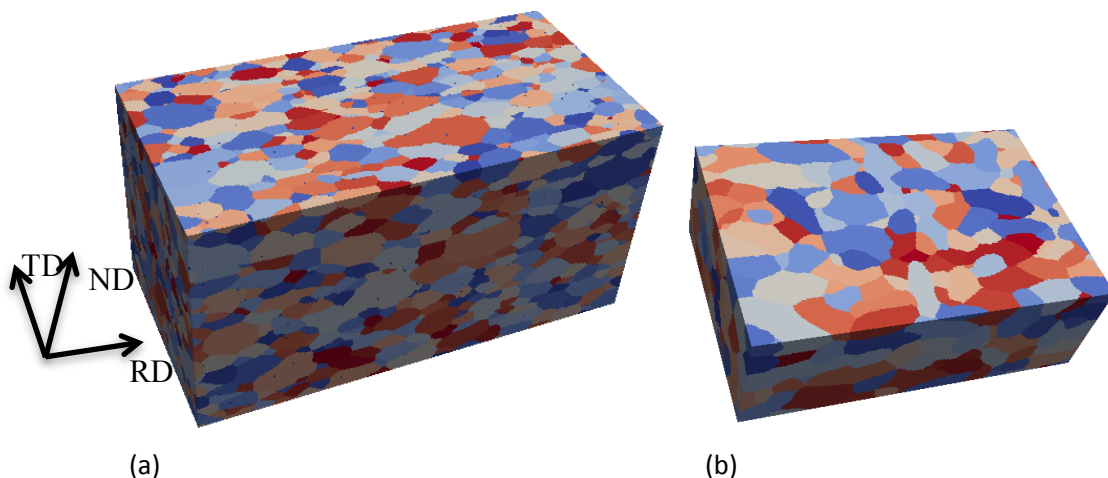


Figure 3.6. Synthetically generated microstructure for Zircaloy-4 using (a) standard Potts model and (b) Dream3D. RD, ND and TD are the rolling direction, normal direction and transverse direction.

The orientations of the grains were assigned stochastically using the information from the Kearns numbers. As noted earlier, the three Kearns numbers give the weighted average of the intensity of the basal plane normals oriented in the three principal directions. Based on the data presented above, we estimate the frequency ratio of grain basal poles pointing in the normal to transverse to RDs to be 3 : 1.5 : 1. A function to approximate these frequency ratios with the overall characteristics shown in Figure 3.7 was constructed as

$$F = 0.9 + \frac{(.00515(\phi - 5)^3 - (\phi - 19)^2)\cos(0.78\theta)}{1169} \quad \text{Eq. 3-1}$$

where θ is the rotation around the TD axis and ϕ is the rotation around the RD axis. The function is plotted in Figure 3.7. This distribution is similar to the characteristics given in Figure 3.5, but the plotting coordinates are different; Figure 3.5 are pole projections, while Figure 3.7 is plotted on orthogonal axes. The basal plane orientation with the highest frequency of occurrence is at $\theta = 30$ and $\phi = 0$. This estimate is for model demonstration purpose and will be refined and adjusted for the various Zircaloy-4 as more specific information becomes available.

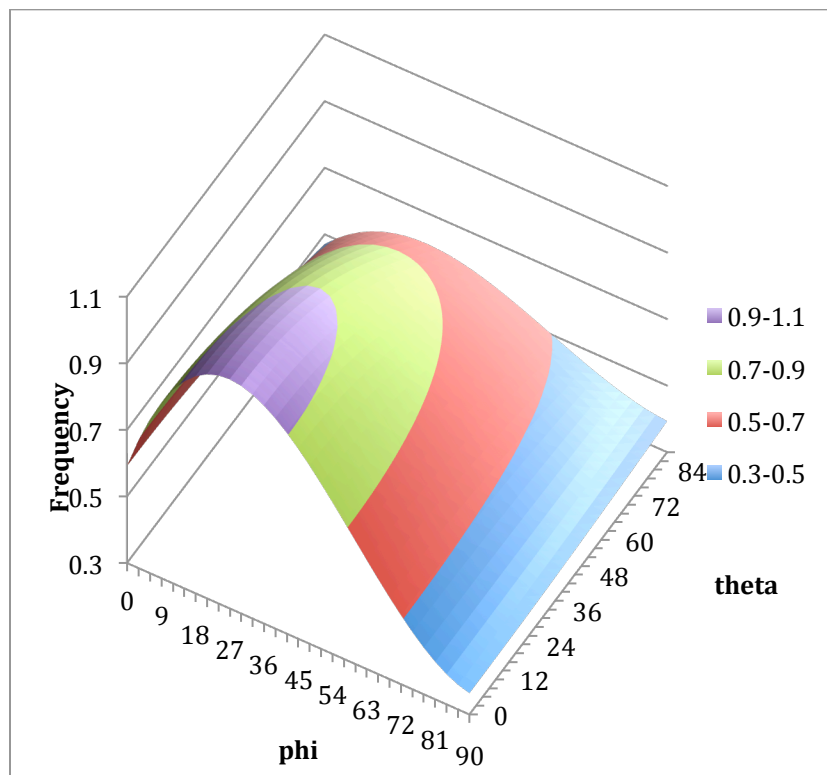


Figure 3.7. The frequency of basal pole orientation as a function of rotation around the transverse direction, θ , and the rolling direction, ϕ .

The generation of 3D, synthetic, Zircaloy-4 microstructures has been demonstrated here with the well-characterized grain size and shapes, grain texture and crystallographic texture to match a data obtained experimentally and published in the open literature. These methods can be adapted to generate the underlying microstructure of any Zr-based claddings as data on their microstructure becomes available.

3.2 Phase Stability and Thermodynamics of Zirconium-Based Cladding

The hybrid model, as described in Chapter 1, is a rigorous thermodynamic model and requires knowledge of the phases present in the system and their free energies as a function of composition and temperature. This section describes the phase stability diagram of the Zr-H system, the phases that occur in claddings under dry-storage conditions, their crystal structures and free energies, as well as the incorporation of these materials physics into the hybrid model.

However, before proceeding to the Zr-H materials system, it should be noted that the alloying elements added to the different Zr-based cladding, described in Table 3.1 and the resulting second phase precipitates, described in Table 3.2 will not be addressed at this time. Accurate information about the phase stability and free energy curves of the various phases are essential for developing predictive hydride formation and reorientation capability. The model minimizes free energy along paths that are determined by the starting composition distribution in the microstructure. Thus, it is important to have good free energy functions that describe thermodynamics of the system. We will start with known free energy curves for the Zr-H system and add the other components with information available in the literature and thermodynamic databases. The minor components are thought to influence the oxidation behavior, which influences the amount of hydrogen uptake. It is not expected to influence the hydride formation and reorientation directly, rather details of kinetics and perhaps some morphology as the precipitates may influence nucleation sites. These refinements will be added as the details become available, but for now, the Z-H will be treated.

The general phase diagram for Zr-H system has been known since the 1950's. The outlines given by Beck (Beck, 1962) in Figure 3.8 and confirmed by Zuzek et al. (Zuzek et al., 1990) in Figure 3.9 as shown below have largely remained unchanged, however the structure and stability of the exact phases has been the subject of much debate (Northwood & Kosasih, 1983). The α -phase is a hexagonal (HCP) low-temperature phase with some solubility of H, which increases with temperature as shown in Figure 3.8 and Figure 3.9. The higher temperature phase, β -phase, is stable at temperatures higher than the eutectoid and is typically not seen in claddings. While the early literature characterized it as body-centered cubic (BCC), it is now largely accepted to be orthorhombic. As hydrogen content increases, the δ -ZrH_{1.5} phase starts to form (Bradbrook et al., 1972; Ells, 1968) and at even higher hydrogen contents the ϵ -ZrH₂ forms. Under certain conditions, another metastable phase γ -ZrH has been reported to form (Root et al., 2003). These phases and their crystal structures are shown in Figure 3.10, Figure 3.11, and Figure 3.12 and will be discussed in more detail in the next section.

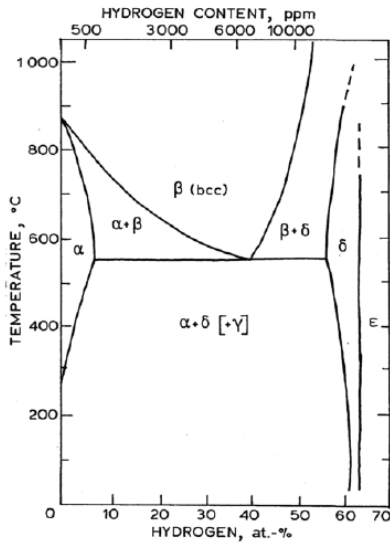


Figure 3.8. Phase diagram for Zr-H Binary System.

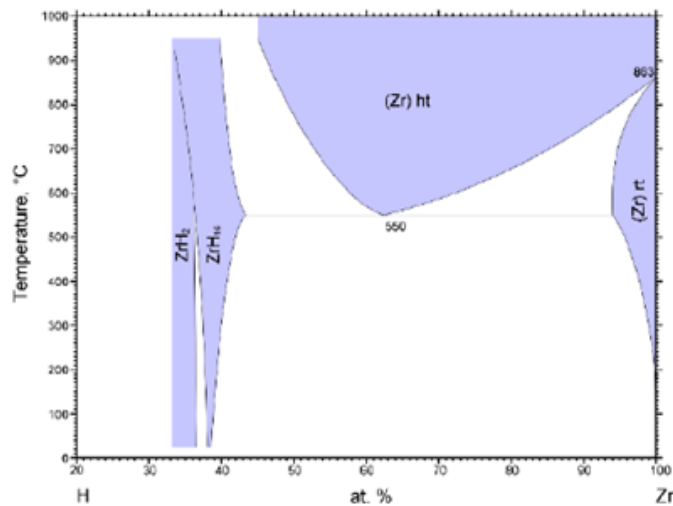


Figure 3.9. An early Zr-H phase diagram proposed by Beck (Beck, 1962).

3.2.1 Generating Free Energies

While the crystal the equilibrium phases and their crystal structure are well characterized, the free energies of the phases are required for simulation of the precipitation by the model. We restrict the model to just two components, Zr and H, for now for model development and demonstration purposes to make the thermodynamic calculations tractable. We consider the two components, Zr-H, in the composition and temperature ranges of interest for nuclear fuel applications, the crystal structure and free energies were calculated using *ab initio* calculations using density functional theory (DFT) and computational thermodynamics using CALPHAD-type (CALculation of PHase Diagrams) calculations. The supercell total energy calculations with DFT were used to determine the crystalline structure of the various Zr-H phases. The DFT calculations were based on the generalized gradient approximation for exchange and correlation, and plane

waves (Payne et al., 1992). A more detailed description of the computational DFT work is provided in a separate report (Glazoff, 2013).

A self-consistent description of phase equilibria in multi component systems and thermodynamic properties of materials was used to bridge between phase equilibria and thermodynamic properties of Zr-H. In this work, commercial databases for zirconium alloys TTZR1 (ThermoTech Ltd.) and binary alloys TCBIN (ThermoCalc AB) were used. These databases and the ThermoCalc version S software were used to generate data on the thermodynamic properties of hydrides, in particular, partial molar enthalpy and entropy of hydrogen. The obtained results were consistent with the constructed phase diagrams and property diagrams. All results were critically evaluated in light of the existing experimental data.

The equilibrium crystalline structures of HCP Zr and its three hydrides are depicted in Figure 3.10 and Figure 3.11, respectively. In all cases, the equilibrium lattice parameters were determined by total energy relaxation technique of the lattice parameters and corresponding atomic positions.

The low temperature α -phase of Zr has HCP structure characterized by the 2/1 ratio of tetrahedral and octahedral interstitial positions per unit cell. The lattice parameters were determined in this work as $a = 3.2276 \text{ \AA}$ and $c = 5.1516 \text{ \AA}$, space group P63/mmc, see Figure 3.10. These results are in excellent agreement with experimental data reported in the literature.

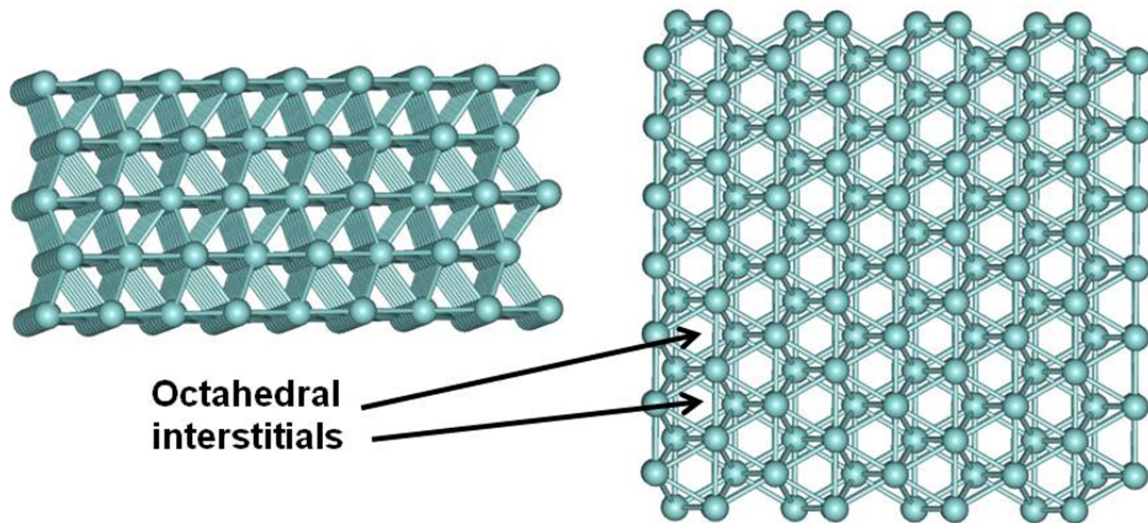


Figure 3.10. Hexagonal (hcp) Zr structure (different views): (a) in the direction perpendicular to the (0001) axes; (b) in the direction of the (0001) axes. Zr atoms are shown in cyan color; octahedral interstitials are indicated by arrows.

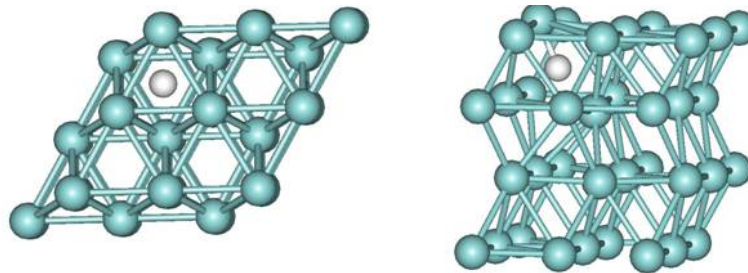


Figure 3.11a & b. HCP Zr with a dissolved hydrogen in the (a) octahedral site or (b) forming a metastable Zr-H-Zr bond (Glazoff, 2013).

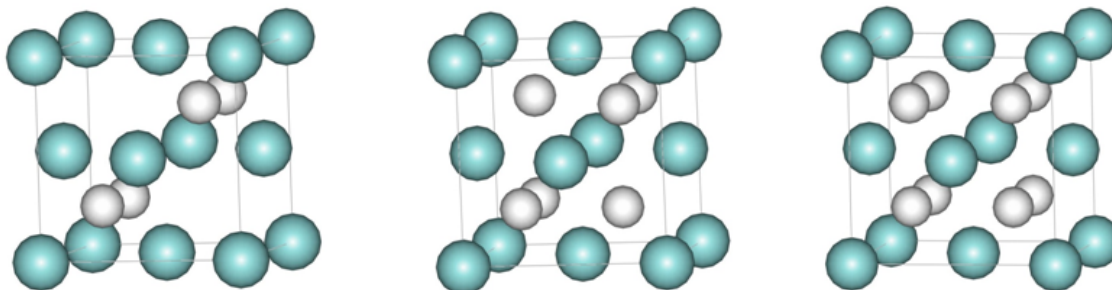


Figure 3.12a-c. The compounds (a) γ -ZrH, (b) δ -ZrH_{1.5} and (c) ϵ -ZrH₂ are orthorhombic, cubic and tetragonal respectively. Teal colored spheres represent Zr and while H atoms (Glazoff, 2013).

There are three distinctly different types of zirconium hydride structures described in the literature: γ -ZrH, δ -ZrH_{1.6-1.7} (which occurs as off-stoichiometric, but was modeled in this work as ZrH_{1.5}) and ϵ -ZrH₂ (Blomquist et al., 2010). In Figure 3.13, the results of first principles calculations yielding the three energy relaxed crystal lattice structures are presented. Again these results are in excellent agreement with those reported in the literature.

The values of the Gibbs free energy computed at T=800 K are illustrated in Figure 3.13; these values lie in the range from 20,000 J/mol to ~ 8,000 J/mol. This reference range will be useful when we discuss existing data on partial molar enthalpy of hydrogen in different zirconium alloys, as well as for determining the driving forces of hydride formation. The corresponding numerical data are used for phase field calculations of zirconium hydride microstructure evolution by fitting these tabulated data and directly using the numerical data and will be described later.

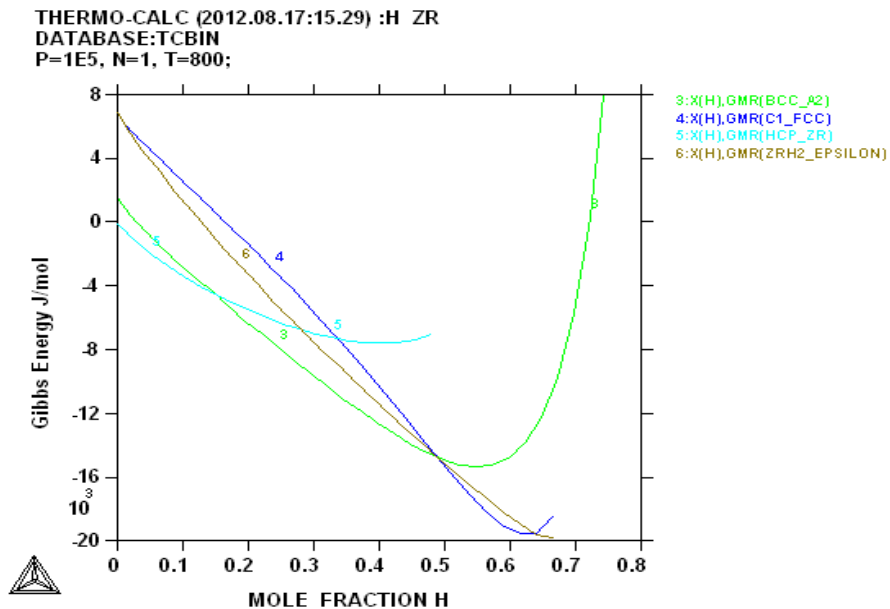


Figure 3.13. The Gibbs free energy of the several phases in the Zr H system as a function of the hydrogen mole fraction at 800 K. The light blue curve, labeled 3, and the dark blue curve, labeled 4, are the free energies of the phases of interest, namely α -Zr and δ -ZrH_{1.5}, respectively.

The phase diagram for the hydrogen mole fraction varying from 0 to 0.1 is given in Figure 3.14. It provides an estimate of the hydride dissolution at temperature 550°C as corresponding to ~0.054 mole fraction of hydrogen. Also, a distinctive feature of this diagram is the retrograde solubility above 550°C, with a minimum corresponding to ~600°C. Again, these results correspond well to the existing experimental data (Ostberg, 1962; Yamanaka et al., 1997; Zuzek et al., 1990) giving confidence in the thermodynamic calculations.

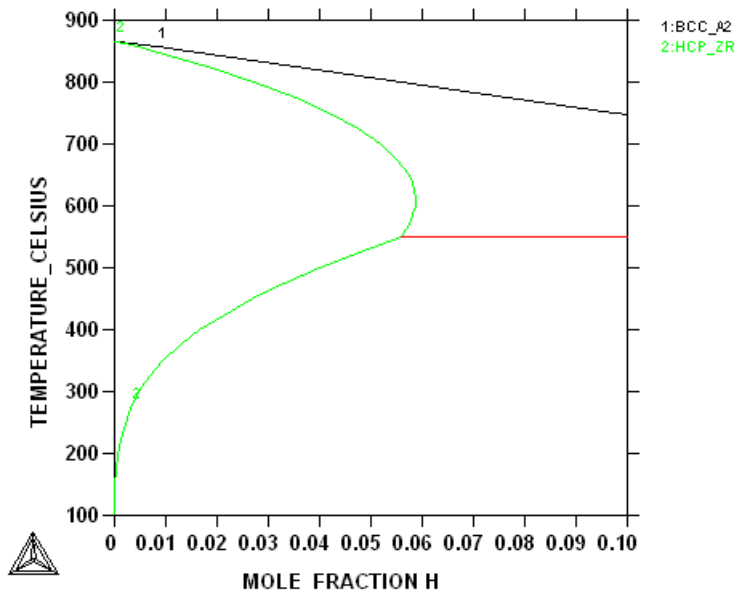


Figure 3.14. Portion of the Zr-H phase diagram showing a detailed view at the Zr-rich region.

The free energy data for the α -Zr and δ -ZrH_{1.5} phases at 300°C plotted in Figure 3.13 were fitted using polynomials of the fifth order as shown in Figure 3.15. The fitted free energy functions at 300°C are

$$E_{\alpha\text{-Zr}} = 2.135026x^5 - 16.96998x^4 + 7.119466x^3 - 1.541714x^2 - 0.297439x + 0.3679003 \quad \text{Eq. 3-2}$$

for the α -Zr phase, and

$$E_{\delta\text{-ZrH}_{1.5}} = 2.135026x^5 - 0.6183701x^4 - 0.6586253x^3 + 0.6083004x^2 - 0.4182968x + 0.2992497 \quad \text{Eq. 3-3}$$

for the δ -ZrH_{1.5} phase. The free energies for the γ -ZrH and ϵ -ZrH₂ are included for completeness, but not used for the demonstration purposes of this report. The use of just the δ -ZrH_{1.5} phase and its free energy is justified in the next Section 3.3. In addition to these fitted polynomials, the model has been developed so that the free energies can be directly obtained from the numerical data by local interpolation to the exact composition.

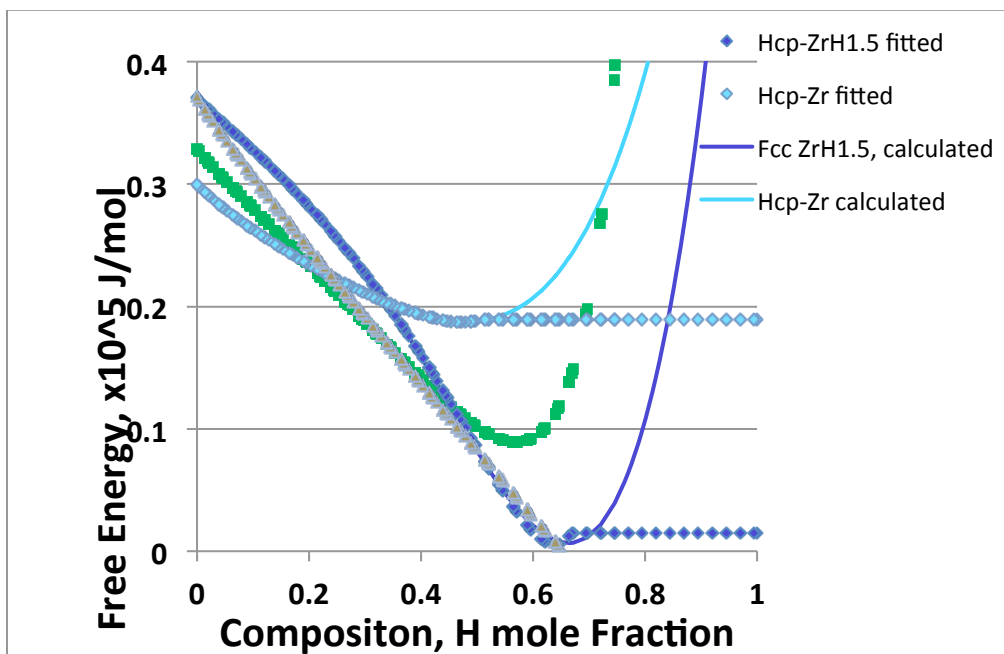
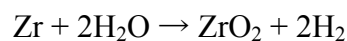


Figure 3.15. Free-energy curves for the Zr-H system at 300°C.

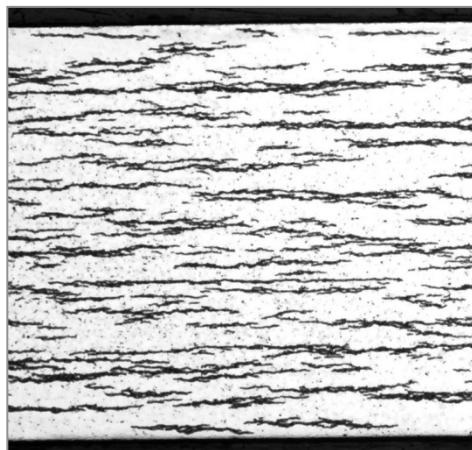
3.2.2 δ -ZrH_{1.5} Precipitation

The formation of hydride precipitates in clad is a well-known and well-documented phenomenon. Zr-based claddings oxidize while in the reactor as



This reaction produces a surface oxide layer and H₂ gas. Some portion, estimated to be 5 to 20%, of the hydrogen gas released by this reaction is absorbed by the clad and diffuses into the clad. The absorption process is typically called hydrogen uptake. Depending on

the alloy composition, temperature and amount of H absorbed, the H can stay dissolved in the cladding or it can precipitate forming zirconium hydride precipitates when the solubility limit is exceeded. Neutron irradiation of the cladding during reactor service increased the solubility of hydrogen solubility in the α -Zr matrix and depending on the composition and microstructure of the cladding, the precipitates may or may not form during fuel service in reactor. The morphology of the $ZrH_{1.5}$ precipitates that form during service in reactor is characterized by the needles aligned as shown in Figure 3.16a (Hanson et al., 2011; Birk et al., 2012). If the hydrides do precipitate in reactor, they are thought to precipitate at defects and grain boundaries that are preferentially aligned along the circumferential direction of the clad as shown in Figure 3.16. The circumferentially oriented hydrides form in reactor when the internal stress applied by the swelling fuel is countered by the coolant pressure. When the used fuel rods have completed their service life, they are stored in cooling pools for some years. The temperature of the claddings is much lower while in the spent fuel cooling pools and hydride precipitates definitely form during this phase with the circumferentially oriented hydrides as shown in Figure 3.16. When the storage pool approaches capacity, the assemblies are transferred to dry storage casks. Before sealing, they go through a drying operation where the decay heat of the fuel is not cooled and the fuel assembly temperature is allowed to reach as high as 400°C. During the drying stage, due to the temperature increase, some of the hydride precipitates, shown in Figure 3.16, redissolve into the zircaloy clad. Upon cooling and subsequent dry-storage, the hydrides reprecipitate but are reoriented along the radial direction as shown in Figure 3.17. The alignment is due to the stress state of the clad. With the coolant no longer applying a compressive stress, the swelled fuel pellets cause a tensile hoop stress in the clad. The hydride precipitates form perpendicular to this hoop stress. This orientation is undesirable as the oriented precipitates act as stress concentrators and may lead to fracture of the clad during long-term storage. The phases, composition and morphology of the hydride precipitates have been the subject of many studies; they will be reviewed briefly here and the model development to incorporate these hydride characteristics will be described.



300 um

Figure 3.16. ZrH precipitates in zircaloy cladding have a characteristic morphology. They align themselves to form platelets in the radial direction of the cylindrical clad.

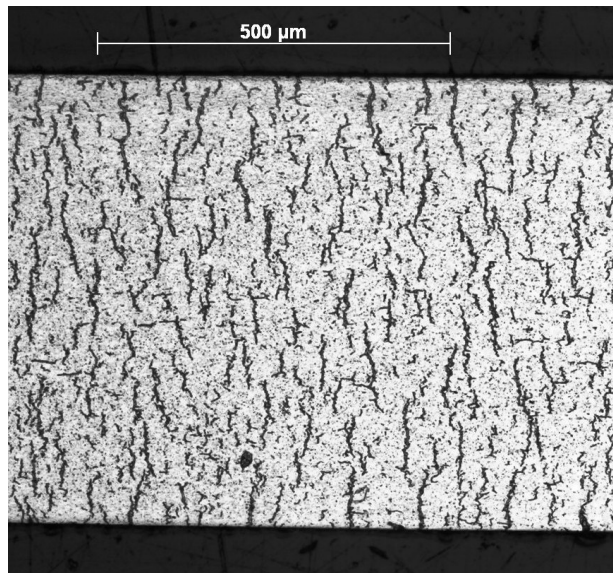


Figure 3.17. The ZrH precipitates have oriented themselves in the axial direction due to the hoop stresses present in the clad.

In Section 2.2.1, the first-principles and thermodynamic calculations show three phases of zirconium hydride with free energies that are close together as seen in Figure 3.13. Their minima occur at similar compositions and the free energy curves intersect with no hydride phase having a dominant energy advantage over the others. While the free energy data shown in Figure 3.13 are for a temperature $T = 300^{\circ}\text{C}$, the free energies for $T = 350$ and 400°C are very similar. Furthermore, all three phases have been observed under different conditions and there are some contradictory data suggesting that $\delta\text{-ZrH}_{1.5}$ may not be the hydride phase that is precipitating as described later in this section. After careful review of the published data, for this demonstration, we have chosen to not simulate the $\gamma\text{-ZrH}$ and $\varepsilon\text{-ZrH}_2$ phases and thus their free energies and phase structures are not included in the model. However, the thermodynamic data and model capability is being developed, so that should the presence and behavior of the $\gamma\text{-ZrH}$ and $\varepsilon\text{-ZrH}_2$ phases become significant to hydriding of Zr-based claddings, they can be included. This choice to discard $\gamma\text{-ZrH}$ and $\varepsilon\text{-ZrH}_2$ phases is justified in the following.

As already described, at reactor-operating temperature, the zirconium cladding absorbs hydrogen and forms hydride precipitates when the hydrogen solubility limit is exceeded. The zirconium matrix is the HCP α phase (P63/mmc, $a = 3.2276 \text{ \AA}$ and $c = 5.1516 \text{ \AA}$) with one Zr atom at (0.333, 0.666, 0.25). For the sake of simplicity, the other alloying elements are ignored. At reactor fuel cladding temperature, which are typically 340°C at the outer tube diameter and $\sim 370\text{-}380^{\circ}\text{C}$ at the inner tube diameter, the hydrogen solubility ranges between 100-150 wt. ppm (Kearns, 1967; Motta & Chen, 2012).

Below 550°C , three hydride phases have been experimentally observed in the phase diagram of the zirconium-hydrogen system over the composition range 0-60 at.% of hydrogen: the stable face-centered cubic (FCC) $\delta\text{-ZrH}_{1.6-1.7}$ typical has Zr/H ratio of ~ 1.66 (CaF_2 prototype structure with space group Fm $\bar{3}$ -m; $a = 4.778 \text{ \AA}$; $V = 109.07 \text{ \AA}^3$ as shown in Figure 3.12b) (Beck, 1962) the stable face-centered tetragonal (FCT) $\varepsilon\text{-ZrH}_{1.74-2}$

(ThH₂ prototype structure with space group I4/m mm; a = 4.9689 Å, c = 4.4497 Å as shown in Figure 3.12c) (Zuzek et al., 2000), and the metastable ordered FCT γ -ZrH (space group P42/n; a = 4.596 Å, c = 4.969 Å; V = 103.72 Å³) (Sidhu et al., 1963). More careful characterization by inelastic neutron scattering of ZrH showed that the γ -phase possesses a small orthorhombic distortion (space group Cccm; a = 4.549 Å, b = 4.618 Å, c = 4.965 Å as shown in Figure 3.12a) (Kolesnikov et al., 1994). Despite multiple recent attempts to synthesize the pure phase γ -ZrH (Bashkin et al., 1992; Kolesnikov et al., 1994), no one has successfully produced a bulk specimen consisting entirely of the γ -hydride phase, even when hydrogenating specimens to 1:1 stoichiometric composition of this phase. This observation seems to confirm the metastable character of the γ -hydride phase at temperature below the eutectoid temperature. The FCT ε -hydride phase is usually not formed for hydrogen compositions in zirconium alloys of practical interest in nuclear applications (Puls, 2012), and is therefore not of direct interest for the topic of this report. Recently, it was also suggested by Zhao and coworkers (Zhao et al., 2008) that another metastable coherent trigonal phase dubbed ζ , with probable stoichiometry ZrH_{0.25-0.5} and ZrH_{0.5} being the most frequent composition (space group P3m1; a = 3.3 Å, c = 10.29 Å), could exist based on results from electron precession microdiffraction and electron energy loss spectroscopy, however this phase has not yet been confirmed by other research groups. The exact nature, role and occurrence of the γ -phase within the α -Zr matrix remains controversial (Lanzani & Ruch, 2004). They reported stable δ phase and metastable γ -phase differ only in the degree of ordering of the hydrogen atoms on tetrahedral sites, which in turn affects the hydride composition. In the δ phase, four H atoms randomly occupy the eight available tetragonal (0.25, 0.25, 0.25) sites, while in the γ -phase hydrogen atoms occupy the tetrahedral sites on alternating (110) planes (Zr atoms are at the (0.25, 0.25, 0.25) sites and H atoms at (0, 0, 0) and (0, 0, 0.5)). Metallographic studies of specimens in the composition range ZrH_{1.47-1.57} showed that the γ -hydride phase appeared as banded precipitates of lenticular shape embedded in the majority δ -hydride phase (Barraclough & Beevers, 1970). These specimens showed some structural instability since re-examination of these specimens after 6 months revealed additional γ -hydride precipitates formed at the α/δ boundaries while small, globular precipitates of α -Zr were found at the δ grain boundaries (Puls, 2012). The metallographic evidence obtained by Barraclough and Beevers (Barraclough & Beevers, 1970) indicates that the γ -hydride phase forms in δ -hydride by a shear mechanism, with the banded structure indicating that this shear is relieved by alternate twinning of the lattice in opposite directions. The suggestions by both Beck (Beck, 1962), and Barraclough and Beevers (Barraclough & Beevers, 1970) that the formation of the γ -hydride phase (and the ε -hydride phase) in δ -hydride occurs essentially by a martensitic type transformation are supported by the analyses and experimental results of Cassidy and Wayman (Cassidy and Wayman, 1980a, 1980b). However, in contrast to a strictly diffusionless martensitic transformation, these invariant plane strain transformations must be accompanied by a change in hydrogen composition. The need for a composition change creates some uncertainty in their analyses to determine the habit planes of the product γ -hydride precipitates (and ε -hydride precipitates) of these transformations as it is not clear if the composition change occurs before, during or after the transformation. In recent years, contradictory statements have emerged concerning the stability of the γ -phase and possible phase transitions between the δ - and γ -phases: for example,

Steuwer and coworkers (Steuwer et al., 2009) suggested, based on X-ray diffraction observation, that a $\delta \rightarrow \gamma$ stress-induced martensitic transformation occurs via ordering of the hydrogen atoms, akin to a Snoek-type relaxation, while the conventional view is that if the metastable γ -hydride phase forms at all, it transforms into the stable δ phase, i.e., $\gamma \rightarrow \delta$ (Northwood & Kosasih, 1983; Lanzani & Ruch, 2004). Some of these controversies may be ascribed to the fact that conventional laboratory-based techniques used in the study of these hydride phases are essentially surface techniques. They provide very little information about the micromechanical properties of the hydrides, their crystallography and their relationship with the matrix in the bulk (Une et al., 2004), where additional constraints are likely to change any transformation properties compared to those occurring at the surface. As pointed out by Lanzani and Ruch (Lanzani & Ruch, 2004), the elusive metastable γ -phase is observed mostly after rapid quenching of the Zr alloy sample (e.g., $>10 \text{ K min}^{-1}$) (Bradbrook et al., 1972; Ells, 1968), but eventually transforms into the δ -phase at temperatures in excess of 150°C (Nath et al., 1973). Based on their experimental results, as well as on previous experiments, these authors also concluded that γ is indeed metastable in typical nuclear-grade zirconium alloys such as Zircalloys, while it might be stable in higher purity zirconium ($>98\text{-}99\%$), as proposed earlier by Beck (Beck, 1962) and Mishra and co-workers (Mishra et al., 1972).

Indeed, recent experimental investigations of Zircaloy-4 showed that only the δ hydride phase is present in this material over a large range of temperature and hydrogen loading relevant to nuclear application (Kiran Kumar et al., 2010; Santisteban et al., 2010). Since the purpose of the present research is to investigate nuclear-grade zirconium alloys, this study can be limited only to the study of the formation, evolution and properties of the stable δ -phase within the α -Zr matrix.

Numerous studies have reported that the δ -ZrH_{1.5} phase grows into grains along particular habit planes of the α -Zr matrix and various habit planes have been proposed: the prism plane of $\{101\bar{0}\}$ (Liu et al., 2008), the pyramidal plane of $\{101\bar{1}\}$ (Une & Ishimoto, 2009), the basal plane (0001), $\{101\bar{7}\}$ (Westlake, 1968; Roy & Jacques, 1969), and twinning planes of $\{101\bar{2}\}$, $\{112\bar{1}\}$ and $\{112\bar{2}\}$ (Kunz & Bibb, 1960) of the HCP α -Zr matrix. However the most commonly reported orientation relationship between matrix and precipitate has been (0001) α -Zr// (111) δ -ZrH_{1.5} orientation relationship (Ells, 1968; Perovic et al., 1983). Recently, EBSD characterization of textured Zircaloy-4 sheets showed that the hydrides and the matrix have the (0001) α -Zr// (111) δ -ZrH_{1.5} orientation relationship at all locations sampled (Kiran Kumar et al., 2010). The orientation of the precipitate phase with respect to the matrix is illustrated in Figure 3.18, note the precipitates grow in the basal plane with the direction $[11\text{-}20] \alpha\text{-Zr} // [1\text{-}10] \delta\text{-ZrH}_{1.5}$.

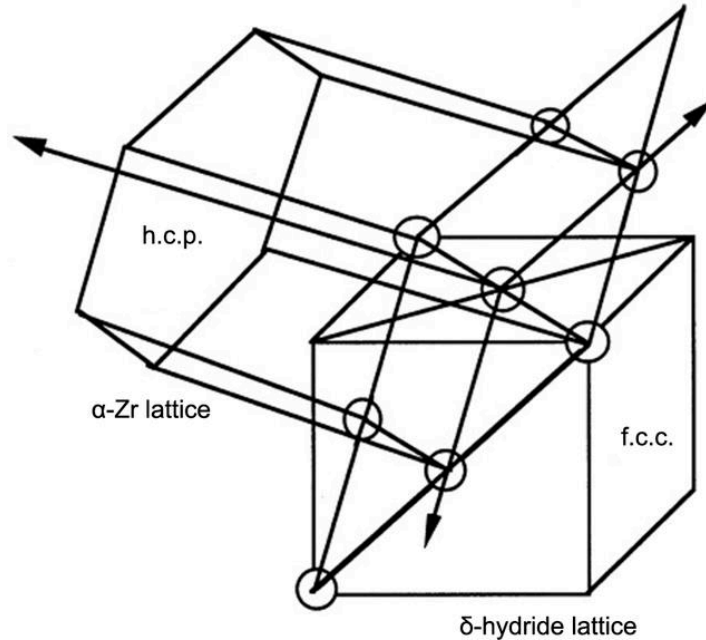


Figure 3.18. A schematic diagram showing the orientation of $\delta\text{-ZrH}_{1.5}$ precipitates with respect to the $\alpha\text{-Zr}$ matrix grain (IUCR, 2014; Li et al., 1999).

Another, key feature of the $\delta\text{-ZrH}_{1.5}$ precipitation in $\alpha\text{-Zr}$ is that a volumetric dilation of 17% occurs. The exact strain accompanying the $\alpha\text{-Zr}$ to $\delta\text{-ZrH}_{1.5}$ transformation has been calculated from the lattice parameters of the two phases (Carpenter, 1973) to be

$$\varepsilon = \begin{bmatrix} 0.048 & 0 & 0 \\ 0 & 0.048 & 0 \\ 0 & 0 & 0.072 \end{bmatrix}$$

As the largest strain occurs orthogonal to the basal plane of the $\alpha\text{-Zr}$ and the smaller strains occur in the basal, but orthogonal to each other, the precipitates have been thought to be disc-shaped. The literature overwhelmingly refers to the $\delta\text{-ZrH}_{1.5}$ precipitates as platelets. However, almost all the TEM micrographs published in the open literature show needle-like precipitates as shown in Figure 3.19 and Figure 3.20 (Perovic et al., 1982). However, the discussion of precipitate shape in the literature continues to suggest that the individual precipitates are platelets.

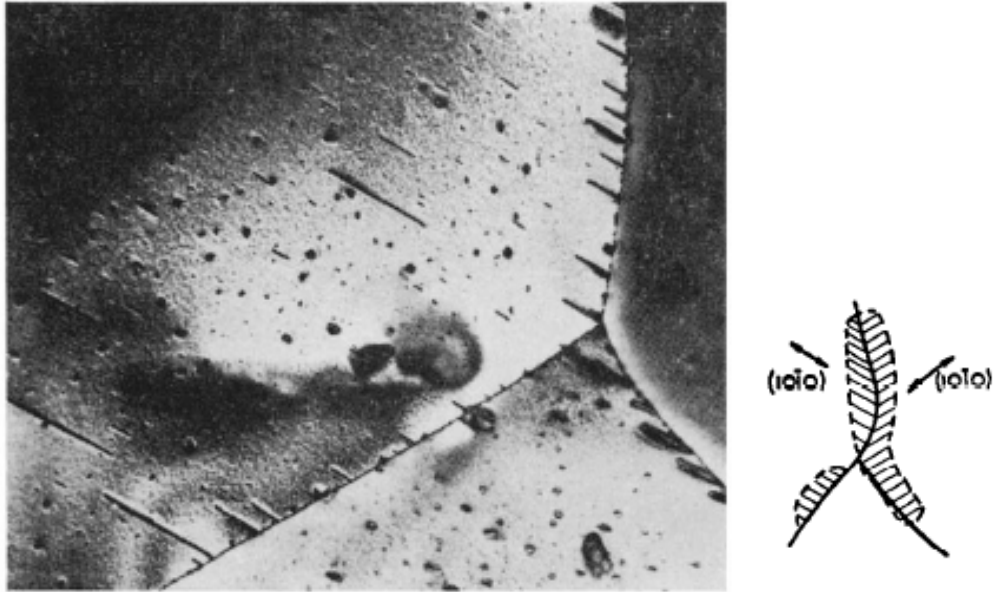


Figure 3.19. Preferential precipitation of hydrides on grain boundaries shown in SEM (left) and schematically (right) (Ells, 1968).

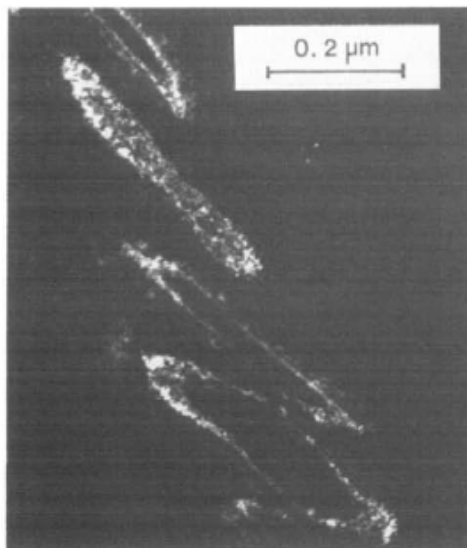


Figure 3.20. $ZrH_{1.6}$ precipitates with needle-like morphology align to form a larger plate (Perovic et al., 1983).

3.2.3 Modeling δ - $ZrH_{1.5}$ Precipitation

Generalizing the equation of state to multiple components: The hybrid model is described in detail in Chapter 1 for a simple two-component, two-phase materials systems. In this section, we develop it further to generalize it to apply to more complex materials system. The framework of the model will be described and it will be left in a state that can be further developed in the future to add the complexity of thermodynamic, kinetic and crystallographic behavior specific to hydride precipitation in Zr-based claddings. We start with the hybrid equation of state, **Equation 2-5** in Chapter 2 is repeated here for convenience.

$$E_{hybrid} = \sum_{i=1}^N \left(E_v(q_i, C_i) + \sum_{j=1}^n J(q_i, q_j) + \kappa_C (\nabla C_i)^2 \right) \quad \text{Eq. 3-4}$$

This equation gives the total free energy of the system at each volume element or pixel as a function of its local microstructure and composition. The first term, E_v , is the volumetric chemical free energy as a function of the local phase q_i and composition C_i would be calculated using **Equations 3-2 and 3-3** for the α -Zr matrix and δ -ZrH_{1.5} precipitate, respectively. Or alternatively, E_v would be looked up and interpolated using the numerical data described in Figure 3.15. The second two terms define the interfacial energy at either a grain boundary between α -Zr grains or the interface between α -Zr matrix and δ -ZrH_{1.5} precipitate. The J term gives the energy associates with the microstructural change at the interface and the $\kappa_C (\nabla C_i)^2$ term gives the energy associated with the compositional gradient at interfaces. While this thermodynamic description of the volumetric free energy works well, we have generalized it to enable its extension to multiple components in the following way. Instead of using kinetic compositional evolution equation given in **Equation 2-7**, we use the more general form

$$\frac{\partial C}{\partial t} = \nabla \cdot M \nabla \frac{\delta E}{\delta C} \quad \text{Eq. 3-5}$$

where C is the phase-field representing the composition, M is the mobility and E is the total free energy, previously given by **Equation 3-4**, and t is time. However, an alternative method to define and calculate the volumetric free energy, E_v , for a binary system with two components and two phases is

$$E_v = \mu_1 C_1 + \mu_2 C_2 \quad \text{Eq. 3-6}$$

where μ_1 and μ_2 , are the chemical potential of components 1 and 2, respectively, in that phase. This change was motivated to ensure that the model can be developed to incorporate more complex chemistry and phases of Zircalloys, as this information is generated. This formulation is more flexible as it can be generalized to multiple components as (Cogswell & Carter, 2011; Cox et al., 2013)

$$E_v = \sum_{i=1}^q \mu_i C_i \quad \text{Eq. 3-7}$$

Using mass conservation $C_1 + C_2 = 1$ and substituting for in **Equation 3-6**, one gets

$$\frac{\partial E_v}{\partial C_2} = (\mu_2 - \mu_1) \quad \text{Eq. 3-8}$$

When the free energy is known, the chemical potentials of the component 1 and 2 in a given phase can be shown to be

$$\mu_1 = E - \frac{\partial E}{\partial C_2} C_2$$

$$\mu_2 = E + (1 - C_2) \frac{\partial E}{\partial C_2}$$

Eq. 3-9

The free energy E in **Equation 3-9** is calculated using either **Equation 3-2 or 3-3**, depending on the local phase. Or, it is interpolated using the numerical data generated by Thermo-Calc calculations directly. In addition to the volumetric free energy, an interfacial free energy E_i term exists in the traditional phase field model

$$E_i = \kappa (\nabla C)^2$$

Eq. 3-10

The variational derivative of the total free energy with respect to composition is

$$\frac{\delta E}{\delta C} = \mu + \kappa \nabla^2 C$$

Eq. 3-11

To reiterate, the complete definition of the chemical potential is used in **Equation 3-8** in anticipation of additional components and phases to be treated in the future. Thus, evolution of the composition is treated by **Equation 2-4** using the variational derivative in **Equation 3-11** with the free energies of the two phases, α -Zr and δ -ZrH_{1.5} given by **Equations 3-2 and 3-3**.

With this basic change to the hybrid model, the remainder of the developments and adaptation will be described next. The microstructure of the zircaloy matrix and hydride precipitates is evolved using Monte Carlo Potts techniques. The microstructural feature or state is identified by a unique integer identifier q that designates a discrete quantum of material of a particular orientation and phase occupying that site. This set of states q 's evolves to simulate microstructural evolution to minimize the overall free energy of the system along particular microstructural paths. Individual changes to the state q at all the sites are attempted. The change is carried out using the Metropolis algorithm. The probability of the change P is calculated using Boltzmann statistics, where the probability of change is a function of the change in energy ΔE , i.e.,

$$P = \exp\left(-\frac{\Delta E}{k_B T}\right) \quad \text{for } \Delta E > 0$$

$$P = 1 \quad \text{for } \Delta E \leq 0$$

Eq. 3-12

The change in energy, $\Delta E = E_{final} - E_{initial}$, is calculated using **Equation 3-4**. If the probability $P = 1$, the change is carried out. If $P < 1$, then a random number R that is evenly distributed from 0 to 1 is chosen. If $R \leq P$, then the site is changed to its new state. In this way, the microstructure is evolved, while it is directly coupled to the compositional evolution through the equation of state given by **Equation 3-4**. The units of time in the simulations are MCS; 1 MCS is when each site in the simulation has attempted a change. After each MCS, the composition of the system is evolved using

Equation 3-5 at each grid point of the same grid used for the microstructural evolution. A simple Euler solution with forward differentiation in time to the partial differential equation was implemented.

δ -ZrH_{1.5} precipitate crystallography and shape: The first two characteristics of δ -ZrH_{1.5} precipitation behavior to be implemented in the model were the crystallographic alignment and the needle-like shape of the precipitates. The crystallographic alignment of the precipitates with the matrix as shown in Figure 3.18 with the precipitates aligned in the basal plane as (0001) α -Zr// (111) δ -ZrH_{1.5} and direction of the two crystals aligned with [11-20] α -Zr // [1-10] δ -ZrH_{1.5} was incorporated in the model by assigning orientation to the α -Zr grain in the three different spatial directions, namely, the basal plane of each grain is defined by its normal and then the three [11-20] directions in that plane are assigned. These directions, at 120° to each other, are selected at random within each plane. Thus, a precipitate that nucleates will have an energetic penalty to grow in any other direction. This condition is introduced by modifying **Equation 3-12** to

$$P = \exp\left(-\frac{\Delta E + E_p}{k_B T}\right) \quad \text{for} \quad \Delta E + E_p > 0$$

$$P = 1 \quad \text{for} \quad \Delta E + E_p \leq 0$$

Eq. 3-13

where E_p is the energy cost for a hydride precipitate to grow in any other direction than the three favored directions. While it is not yet clear if the growth of the δ -ZrH_{1.5} precipitations in these favored directions is thermodynamically driven to lower its overall energy or kinetically driven by fast growth in that particular direction, for the purposes of this demonstration the former is chosen. However, the kinetically favored crystallographic alignment is unlikely as the volumetric strain described in the previous section suggests an energetically driven process. If necessary, the model can be easily adjusted to make the growth direction favored by kinetics by introducing a mobility term \mathcal{M} before the exponent that is a function of orientation ω as $\mathcal{M}(\omega)$ and deleting the energetic term E_p . The needle-like shape of the precipitate was incorporated by selecting a growth rate G that is much faster in the [11-20] directions, when $\omega = 0, 120$ and 240° . The model was finally modified so that the precipitate growth is governed by

$$P = G(\omega) \exp\left(-\frac{\Delta E + \Delta E_p}{k_B T}\right) \quad \text{for} \quad \Delta E + \Delta E_p > 0$$

$$P = G(\omega) \quad \text{for} \quad \Delta E + \Delta E \leq 0, \quad P = 1$$

Eq. 3-14

δ -ZrH_{1.5} precipitation in a single crystal of α -Zr: The first simulation to be performed with the crystallographic alignment and needle-like precipitates was in a single crystal of α -Zr with periodic boundary conditions in all three directions. The starting composition of the single crystal is a supersaturated solution of H in the α -Zr matrix and allowed to come to equilibrium by nucleation and growth of the δ -ZrH_{1.5}. Nucleation sites are randomly chosen in the single crystal and the nucleation rate is constant. The constant

nucleation rate is implemented by simply attempting nucleation of a $\delta\text{-ZrH}_{1.5}$ precipitates at randomly selected site. The nucleation occurs if the Metropolis algorithm with the probability given by **Equation 3-13** is successful. The simulated growth of $\delta\text{-ZrH}_{1.5}$ precipitates in a single crystal of $\alpha\text{-Zr}$ is shown in Figure 3.21 from two different angles, looking down at the basal plane and at an oblique angle. All precipitates that nucleated and grew are imaged. The different colors simple designate different precipitates. Thus contiguous features of the same color are a single precipitate.

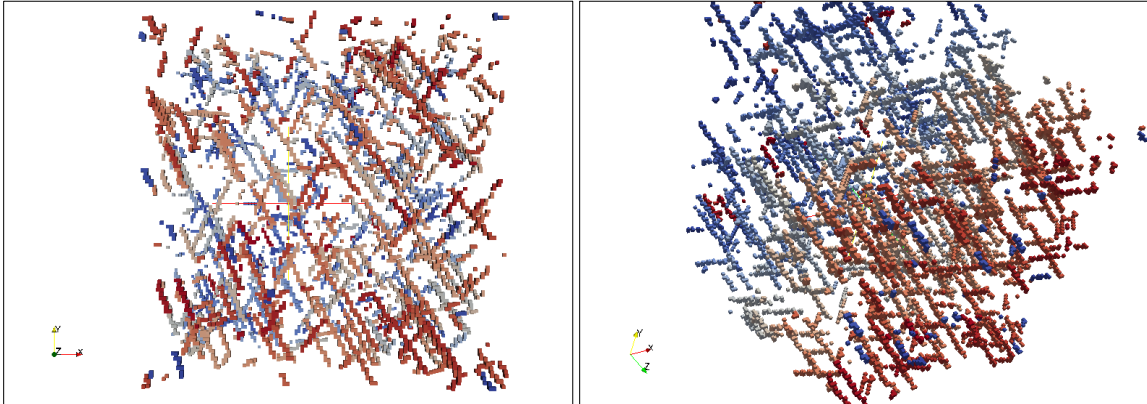


Figure 3.21. Growth of hydride precipitates in a single crystal of $\alpha\text{-Zr}$. The same set of precipitates is shown from two different directions. As one can see the precipitates are needle-like in shape and have three different orientations in the same plane.

$\delta\text{-ZrH}_{1.5}$ precipitation in a polycrystalline of $\alpha\text{-Zr}$: A polycrystalline microstructure generated by normal grain growth, shown in Figure 3.22, is topologically correct with grain boundaries and grain vertices having correct connectivity. It is also equi-axed as would be expected for normal grain growth. The grains are randomly oriented, but the precipitates within each grain are oriented in the basal plane along the preferred growth directions. This version of the simulation used the simpler definition of the variational derivative of the free energy,

$$\frac{\delta E}{\delta C} = \frac{dE_v}{dC} + \kappa \nabla^2 C$$

Eq. 3-15

with quadratic fitting of the free energy curves in Figure 3.22. Again, periodic boundary conditions in all three directions were used. The starting composition was a supersaturated solution of H in $\alpha\text{-Zr}$ with uniform distribution of H in the microstructure. $\delta\text{-ZrH}_{1.5}$ precipitates grew by nucleation and growth with the crystallographic growth preference and needle-like shape described earlier in this section. Nucleation of precipitates was attempted at randomly selected sites at a constant nucleation rate. The resulting precipitate growth is shown in Figure 3.23 from two different angles. All the precipitates in the polycrystalline are shown. As one can see, the orientation of the precipitates is not regular as seen in Figure 3.21, where all the precipitates form within a single grain. In this simulation, the precipitates in Figure 3.23 within each grain align themselves in the three preferred directions of the basal plane, but the basal plane orientation changes from grain to grain, thus the precipitates in the overall structure have many different orientations.

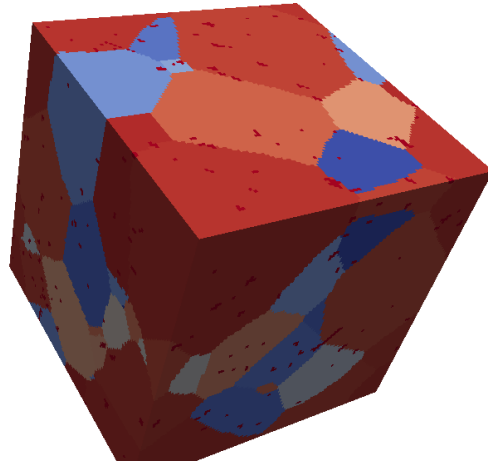


Figure 3.22. Starting microstructure for the hydride precipitation simulations.

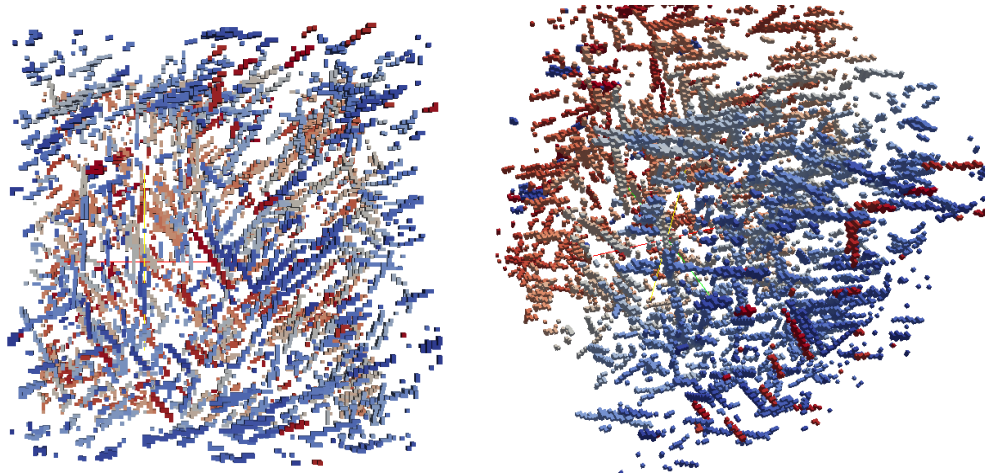


Figure 3.23. All in the precipitates in the polycrystalline are imaged and shown from two different angles.

Effect of stress on δ -ZrH_{1.5} precipitation in a polycrystalline of α -Zr: Another simulation was performed from the same underlying cladding microstructure (shown in Figure 3.22), one with a constant, uni-axial stress applied. Since the model is not yet coupled to a mechanics model, the stress applied was a simple, constant, uni-axial tensile stress that did not change with the nucleation and growth of precipitates. The hybrid model is an energy minimization model and tensorial quantities such as stress and strain cannot be directly incorporated. The stress was introduced in the simulation by adding a strain energy term E_s to the free energy given in **Equation 3-4**. The strain energy of the precipitate was related to the direction of applied stress as

$$E_s = \varepsilon \sin(\phi - 45)$$

Eq. 3-16

where ε is a constant and is a function of the applied stress and strain accompanying hydride nucleation or growth and ϕ is the misorientation angle between the direction of the applied stress and precipitate growth direction. Note in this method of calculation, precipitates that are perpendicular to the applied stress direction have an energetic

advantage to nucleate and grow; while those parallel to the applied stress have an energetic penalty and those at 45° are not affected by the applied stress.

The results of these simulations are shown in Figure 3.24, all precipitates are imaged at the same two angles as that in Figure 3.23. By careful examination of Figure 3.23 and Figure 3.24, it can be seen that there are some precipitates that are oriented vertically in Figure 3.23, the simulation with no applied stress; while there are no precipitates that are oriented vertically in Figure 3.23, simulation with an applied tensile stress in the vertical direction. Furthermore, there are more precipitates that are oriented more than 45° from the applied stress direction and these appear to be longer. This is supported by an analysis of precipitate size distribution for the two cases of applied stress and no stress, shown in

Figure 3.25. The same data are plotted on a log scale and linear scale for the number of precipitates of a given size. The linear plot shows that in the case where there is no stress in the cladding sample, many small precipitates are present. The log plot shows that the cladding with uniaxial stress applied consistently has more precipitates that are larger. It is clear why a larger number, but smaller precipitates formed when no stress was applied in the simulations; since a smaller number of precipitates that are favorably oriented nucleate and grow, the hydrogen diffuses preferentially to these sites allowing them to grow larger. A review of the literature did support the biased orientation of the precipitates as expected; however, no experimental evidence was found to support the observation that the precipitates may be larger when perpendicular to the applied stress. This may be due to the fact that this aspect of precipitate growth has not been examined experimentally or it may be that other factors such as the compressive stress field that, no doubt, forms around the precipitates may limit their growth under any stress condition. A more evolved model that can couple the local micro-stresses may be able to answer these questions.

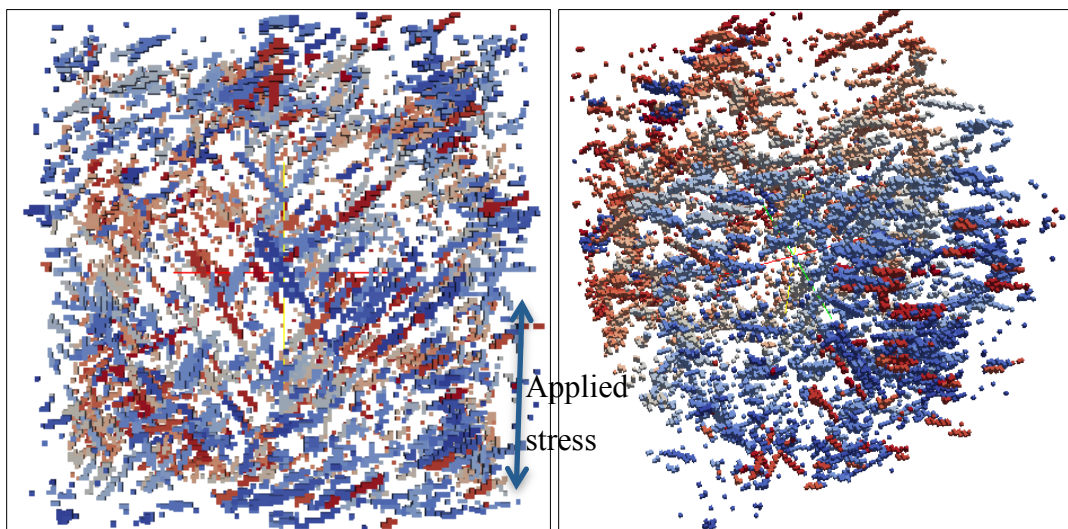
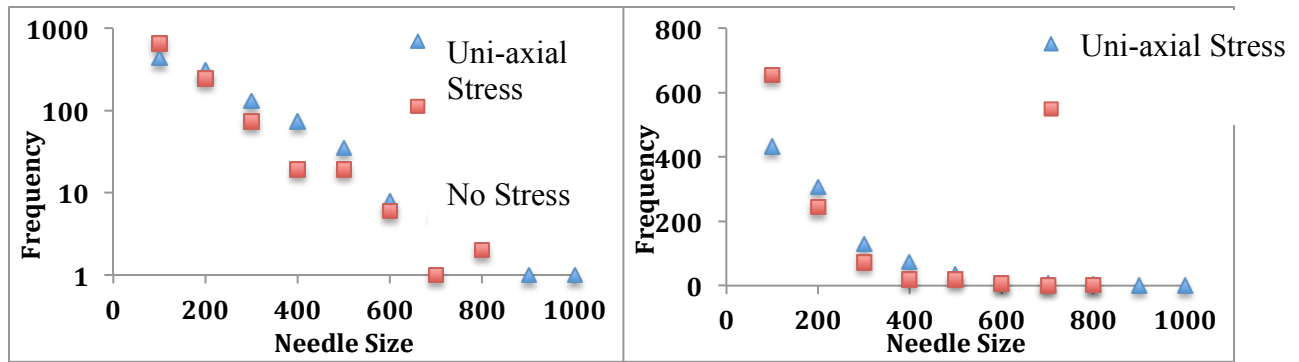


Figure 3.24. The same simulation was run with an uni-axial, constant stress applied.



Uni-axial Stress

No Stress

Figure 3.25. Precipitation size distribution in a polycrystalline Zr-matrix with randomly oriented grains for the case of no applied stress and application of a constant, uni-axial stress. The same data are shown on a log- and normal-plots. The log plot shows the data more clearly for larger needle sizes and the linear plot shows the data more clearly for the smaller shorter needles.

The results presented in Figure 3.23, Figure 3.24, to Figure 3.25 are consistent with expected behavior for needle-like δ -ZrH_{1.5} precipitates forming in an α -Zr matrix. The crystallographic orientation of the precipitates in the matrix has been demonstrated. The methodology for incorporating stress effects on nucleation and growth of the precipitates has also been demonstrated. Furthermore, the model accurately shows that when fewer precipitates can nucleate, the individual precipitate grow larger in size as diffusion of H preferentially occurs to the nucleated precipitates. These results verify that the hybrid model with these physics is working correctly.

Incorporation of grain geometric and crystallographic texture: A second set of simulations used the rolled microstructures generated as described in Section 3.1.1. In these simulations the grains had an average elongation of 2 \times in the RD as compared to the transverse and NDs and the α -Zr grains have orientation with preferred orientation of the basal poles with frequency given by **Equation 3-1** and Figure 3.7. The simulation used periodic boundary conditions in all three directions. The starting composition was over-saturated with all the hydrogen dissolved in the α -Zr matrix at a temperature of 400°C, the temperature was reduced to 300°C and held constant during the simulation. The nucleation attempt rate was constant throughout the simulation. The results of this simulation are presented in this section. Relatively small simulations with limited number of grains were performed to demonstrate model capability. The microstructure generated using Dearm3D, shown in Figure 3-26, has elongated grains in one direction and not in the others. This orientation is selected for illustration purposes.

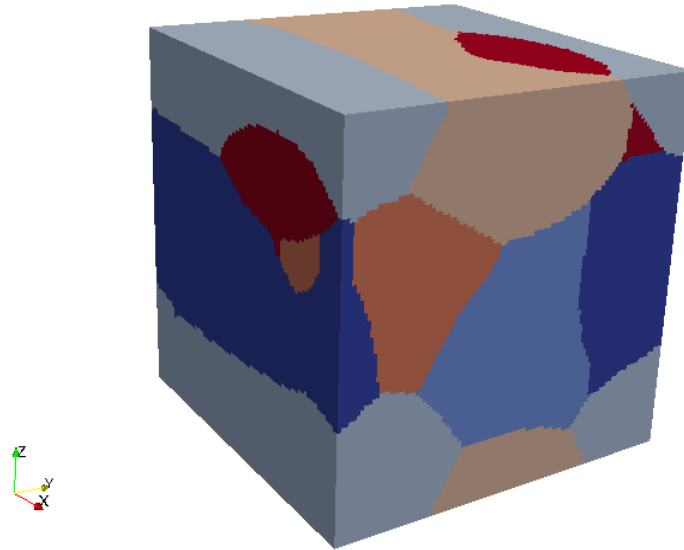


Figure 3.26. Input microstructure with basal orientation stochastically assigned using Equation 3-1 for small simulations with seven grains. The grains are elongated in the X-direction, which is also the rolling direction for the purposes of this illustration.

Two different simulations using this rolled starting microstructure were performed and are shown here. In one, the nucleation sites are predominantly near the grain boundary as observed experimentally (Bradbrook et al., 1972; Ells, 1968; Qin et al., 2011). In this simulation, probability of a nuclei forming near a grain boundary is 80% and anywhere in the microstructure, the probability is 20%. In the other simulation, the nucleation sites for precipitates can occur with equal probability anywhere in the grain structure; in other words, nucleation sites such as dislocation loops are evenly distributed. The nucleation and growth of precipitates with preferred nucleation sites at grain boundaries is shown in Figure 3.27. The same microstructures are shown from two different angles, an oblique angle and one along the RD of the cladding. As noted before, the nucleation attempt rate is constant. In the early stages, nucleation and growth occur concurrently, that is to say as nuclei are forming they start to grow immediately, while other nuclei continue to form. In the intermediate stages, nucleation decreases and the growth of the precipitates dominates. At the end, the exiting nuclei continue to grow with virtually no new nuclei forming until hydrogen in the matrix is depleted to its solubility limit. This behavior is expected; although the nucleation attempt rate remains constant, the success rate of nucleation will continually decrease as the matrix is depleted of hydrogen. As the matrix is depleted of hydrogen, the driving force for nucleation will also decrease. The view shown in Figure 3.27d, e and f, looking down the RD roughly orthogonal to the grain boundaries, clearly shows that precipitates are nucleating and growing primarily near grain boundaries. While it is not clear from these pictures, precipitates do not cross grain boundaries as the crystallographic direction changes in the neighboring grains. This is consistent with the fact that precipitates grow along particular crystallographically-favored directions. The growth of precipitates in this demonstration is controlled by diffusion of hydrogen to the precipitates. Diffusion-limited kinetics in this model has been investigated for simple geometries in previous work, reviewed extensively in Chapter 1, and shown to be simulated correctly.

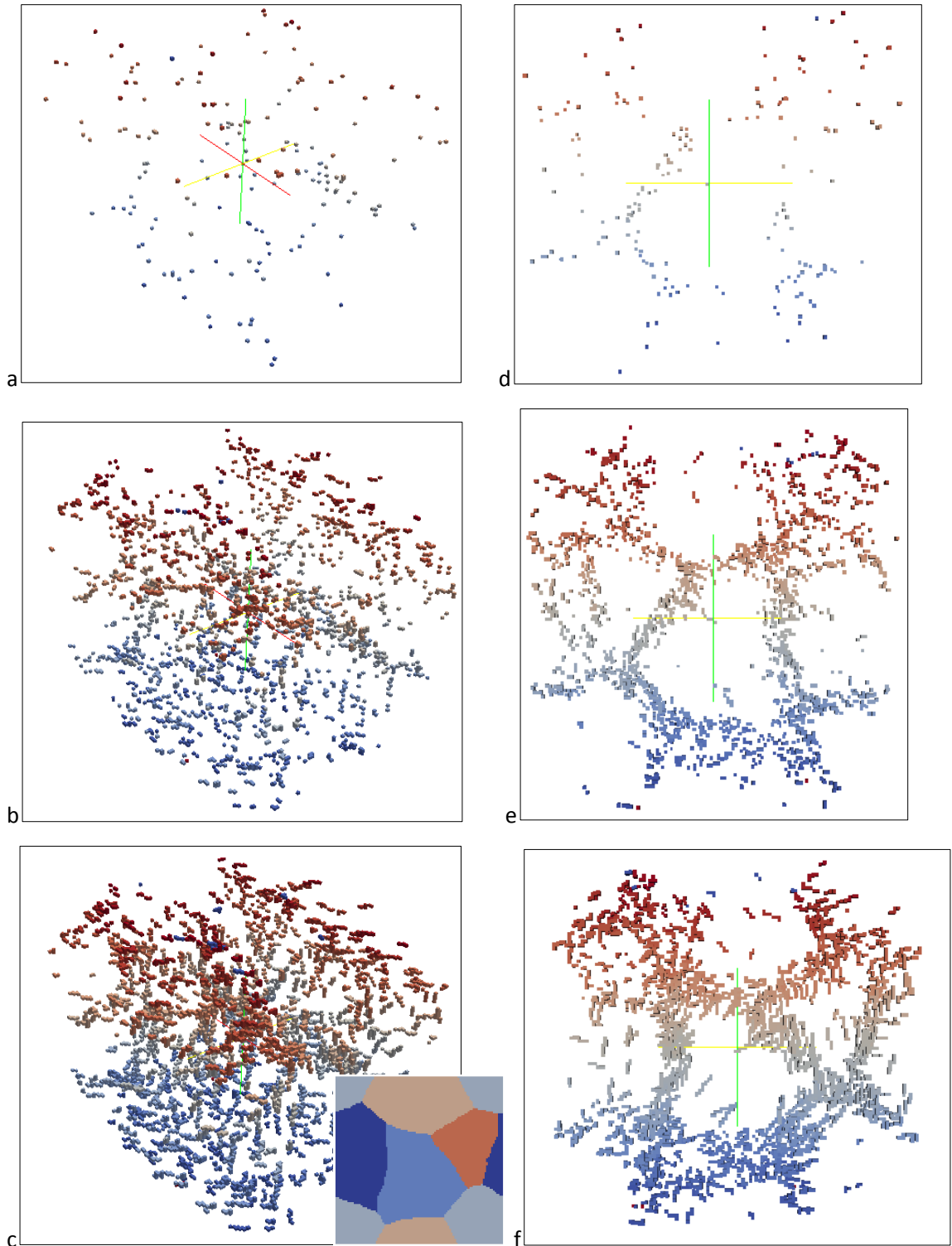


Figure 3.27a, b, and c. Nucleation and growth of $\delta\text{-ZrH}_{1.5}$ precipitates at time = 3, 27 and 520 Monte Carlo Steps (MCS). Nucleation sites are at predominantly at grain boundaries, which is very clearly illustrated in d, e and f. where the same precipitates seen in a, b and c are imaged, but now looking down the rolling direction. The inset between c and f is provided to show the grain boundaries at the surface of the sample and is the same microstructure shown in Figure 3.26.

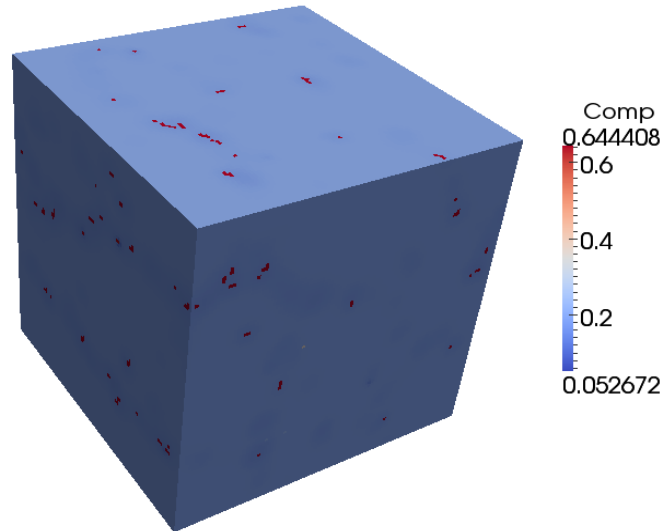


Figure 3.28. The distribution of hydrogen on the surfaces of the microstructure. Unlike, the precipitates only the hydrogen content on the surfaces can be imaged. Hydrogen concentrations are highest in the δ -ZrH_{1.5} precipitates and the matrix is depleted.

Since, we assume that the kinetics of precipitation growth is controlled by hydrogen diffusion from the matrix to the precipitate, the distribution of hydrogen in the matrix should be highest in regions away from the precipitate, decrease as the precipitate surface is approached and then increase sharply at the precipitate surface. This distribution is clearly shown in Figure 3.28, the distribution of hydrogen in the rolled microstructure corresponding to precipitates in Figure 3.27c. The hydrogen concentration is highest in the precipitates and corresponds to a stoichiometry of ZrH_{1.6}, which is very close to that observed experimentally. The composition of the δ -ZrH_{1.5} precipitates in Figure 3.28 is off-stoichiometry, which shows that the hybrid model is working correctly. While the minima in the free energy for the δ -phase is at ZrH_{1.5}, the tangent construction giving the composition of δ -phase at equilibrium with the α -Zr matrix is higher in hydrogen content at ZrH_{1.6}. Again this is verification that the model is correctly simulating the composition evolution accompanying the phase transformation of α -Zr with dissolved H to δ -ZrH_{1.5}.

The hydrogen content in the matrix is depleted with the highest depletion close to the precipitate surface and increases in the matrix away from precipitates. This type of compositional profile is expected in diffusion-controlled phase transformation such as in the one being simulated here. In order to show the hydrogen distribution more clearly, the hydrogen distribution in a 2D slice through the cladding shown in Figure 3.27 and Figure 3.28 is shown in Figure 3.29, grain structure with precipitates is shown in Figure 3.29a, with the corresponding hydrogen distribution in Figure 3.29. The red features are the precipitates in the microstructure in Figure 3.28a and the high hydrogen content of the hydrides in Figure 3.29b. The composition distribution shows high H-content in the precipitates, as expected, with a sharp decrease in hydrogen in the matrix immediately surrounding the precipitate and a gradual increase in regions away from the precipitate. Since this is a 2D slice through the 3D microstructure, the regions with depleted hydrogen in Figure 3.29b without corresponding precipitates in the same locations in Figure 3.29a are near precipitates either above or below the slice that is imaged here. It worth noting that in these simulations diffusion-controlled kinetics is assumed for the

purpose of demonstrating the model; however, should interfacial-reaction be identified later as the limiting process for precipitate growth, the code for this process has already been written and verified.

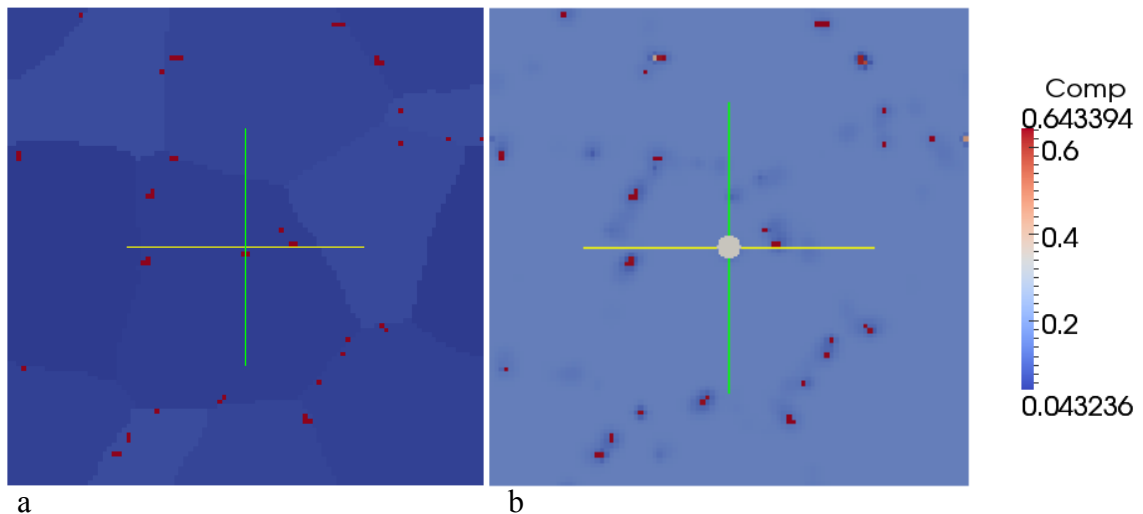


Figure 3.29. A slice through the microstructure shown in Figure 3.27 and Figure 3.28. (a) the grain structure shown in blue with red precipitates and (b) the composition corresponding to this slice. The red in (b) are regions of high hydrogen content as shown in the scale to the right, which is where the precipitates are located.

The simulation showing nucleation of hydride precipitates randomly distributed in the microstructure with equal probability of occurring anywhere is shown in Figure 3.30. Again, a similar trend is seen. At first nucleation events predominate and as these first nuclei grow, others precipitates continue to nucleate at a slower rate and finally growth of existing precipitates dominates. This occurs for the same reason as before, the driving force for precipitate nucleation decreases with decreasing hydrogen content in the matrix. The hydrogen composition gradients in the microstructure are consistent with diffusion-controlled precipitate growth as shown in Figure 3.31. As noted before, precipitates do not cross grain boundaries as the crystallographic orientations in adjacent grains change. While the overall hydride precipitation behavior is similar between the two cases, the precipitates grow more quickly in the spatially randomly nucleating precipitates as shown in Figure 3.32, a comparison of total precipitate formation by precipitate volume for the two cases considered. The precipitate formation growth for the randomly distributed nuclei is faster than for the precipitates that nucleate near the grain boundaries. This difference in behavior is explained by the diffusion distance for hydrogen. As the precipitates cluster near the grain boundaries, the diffusion distance for hydrogen from the grain centers to the precipitates becomes longer, thus increasing diffusion times and reducing the rate of precipitate nucleation and growth. Again, this is consistent with diffusion-controlled precipitate growth kinetics.

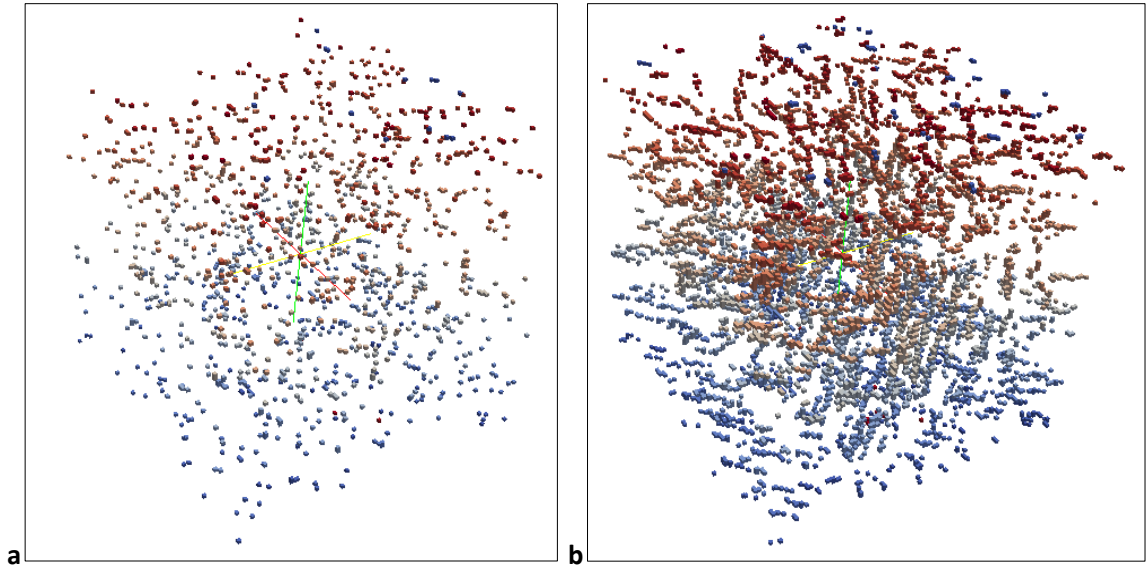


Figure 3.30. Nucleation of precipitation in this simulation occurs with equal probability in any location. Precipitates at time = 5 and 330 MCS are shown here. The subsequent growth is controlled by diffusion.

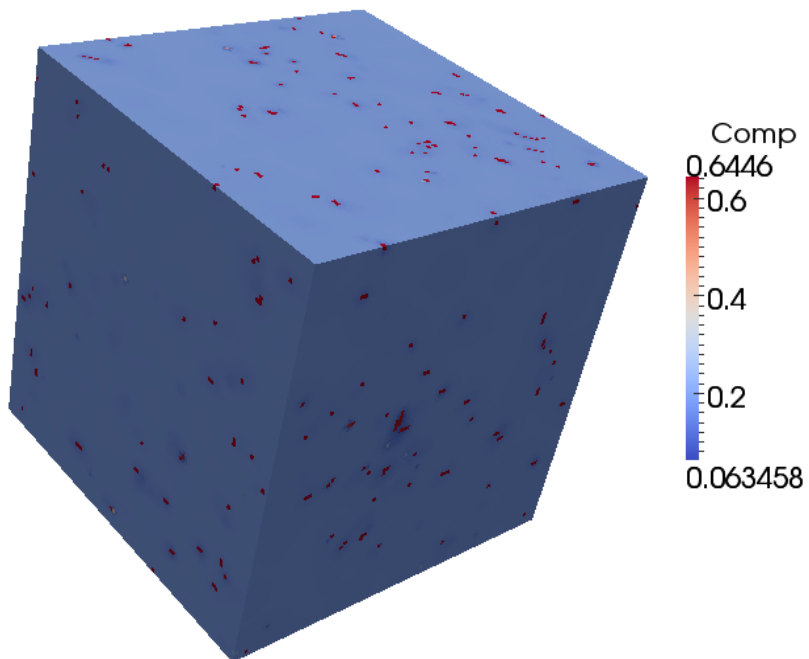


Figure 3.31. The distribution of hydrogen in the microstructure for the simulation results shown in Figure 3.30.

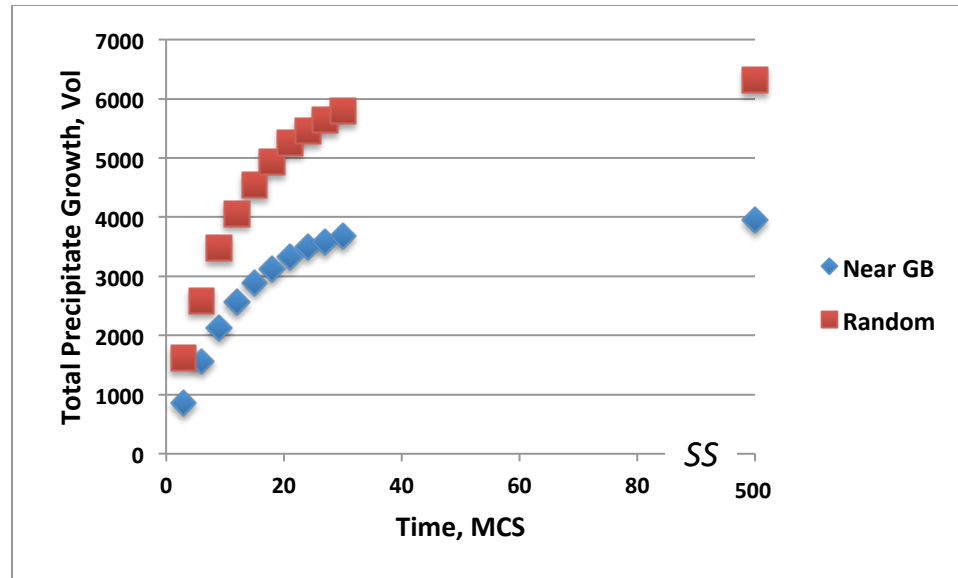


Figure 3.32. A comparison of total precipitate formation for the two cases where nucleation occurs randomly with uniform probability anywhere in the grains and nucleation occurs preferentially at the grain boundaries.

3.3 Summary and Conclusions

The simulation of δ -ZrH_{1.5} precipitation in α -Zr matrix by nucleation and growth in a Zircaloy-4 microstructure has been developed and demonstrated using the hybrid Potts-phase field model. All the basic microstructural evolution processes necessary to simulation hydride precipitation were incorporated into the model and demonstrated. The results of the model show good qualitative agreement with experimental observations. The underlying microstructures of Zr-based claddings can be computationally generated to match the available experimental data on the specific systems; this capability was demonstrated on rolled Zircaloy-4 microstructure with geometric elongation and crystallographic orientation to match the data available about these features. The thermodynamic free energies were obtained using CALPHAD-type calculations for α -Zr, δ -ZrH_{1.5}, γ -ZrH and ϵ -ZrH₂ phases. The calculated free energies for α -Zr and δ -ZrH_{1.5} phases were used for the hydride precipitate formation simulations. At the present time, the other two hydride phases, γ -ZrH and δ -ZrH₂, were not considered in the precipitation simulations, since a review of experimental data indicated that these do not contribute to hydride formation in the claddings during dry storage conditions. The model uses the full chemical potential of the two phases with both components in preparation for the more complex compositions that will be simulated in the near future. The phase transformation from α -Zr to δ -ZrH_{1.5} leading to precipitation by nucleation and growth of precipitates can be simulated. The nucleation rate and subsequent growth of the precipitates is controlled by diffusion of hydrogen. The growth of the precipitates occurred in energetically favorable crystallographic directions. While it is not clear that the growth occurs in particular directions due to thermodynamics of the precipitate growth, this method was chosen for demonstration. However, should the kinetics of precipitate growth prove to be the controlling factor that determines the precipitate growth, the model can be modified to simulate the kinetic mechanism. The needle-like shape of

precipitates was incorporated by biasing the growth rate in the long direction. The nucleation sites of the precipitates, dislocation loops or other defects, can be distributed to match those in the actual materials. We have demonstrated this by allowing nucleation to occur with equal probability anywhere in the grains or predominantly near grain boundaries. Lastly, the effect of applied stress on orienting the precipitate growth was demonstrated. While a very simple, constant, uni-axial stress was used to simulate the preferred growth, it is sufficient to demonstrate the model capabilities. A true micro-mechanical model that can calculate the local complex stress resulting from precipitate growth will be incorporated in the near future.

The hydride growth and reorientation model is built as an extension module for SPPARKS. SPPARKS (Plimpton et al., 2009; SPPARKS) is an acronym for stochastic parallel particle kinetic simulator. SPPARKS is a kinetic Monte-Carlo (KMC) code that has algorithms for both rejection-free KMC and rejection KMC also called Metropolis Monte Carlo. SPPARKS is distributed as an open source code. It is highly versatile, supports a number of different applications, can be extended to add new functionalities and is able to run in serial or in parallel. The parallel version uses the MPI to perform concurrent computations over all processors while minimizing communication overhead between processors. The necessary solvers for treating the partial differential equation **Equation 3-5** are incorporated into the hydride extension module within SPPARKS.

The development of the hybrid model, the methodology to generate and input the initial microstructure, the methodology to generate free energies as a function of composition and temperature to simulate hydride precipitation in Zr-based claddings have been demonstrated in this chapter. In the next chapter, V&V of the model will be demonstrated.

3.4 References

Abe, H., and M. Furugen (2010). Method of Evaluating Workability in Cold Pilgering of Zirconium Alloy Tube, *Mater. Trans.* **51**: 1200-1205.

Abriata, J.P., J.C. Boicich, and D. Arias (1983). The Sn-Zr System, *Bull. Alloy Phase Diagrams* **4**: 147-154.

Allegheny Technologies. "Reactor Grade Zirconium Alloys for Nuclear Waste Disposal" Technical Data Sheet, Allegheny Technologies;
www.alleghenytechnologies.com/wahchang.

Arias, D., T. Palacios, and C. Turrillo (1987). Composition of Precipitates Present in Zircaloy-2 and 4, *J. Nucl. Mater.* **148**: 227-229.

Bai, J.B., C. Prioul, and D. Francois (1994a). Hydride Embrittlement in Zircaloy-4: Part I. Influence of Microstructure on the Hydride Embrittlement in Zircaloy-4 at 20°C and 350°C, *Met. & Mater. Trans. A* **25**: 1185-1197.

Bai, J.B., N. Ji, D. Gilbon, C. Prioul, and D. Francois (1994b). Hydride Embrittlement in Zircaloy-4 Plate: Part II. Interaction between the Tensile Stress and the Hydride Morphology, *Met. & Mater. Trans. A* **25**: 1199-1208.

Barracough, K.G., & C.J. Beevers (1970). Some Observations of the Phase Transformations in Zirconium Hydrides, *J. Nucl. Mater.* **34**, 125-134.

- Barberis, P., D. Charquet, and V. Rebeyrolle (2004). Ternary Zr_Nb_Fe(O) system: phase diagram at 850°C and corrosion behavior in the domain Nb < 0.8%, *J. Nucl. Mater.* **326**: 163-174.
- Bashkin, I.O., V.Yu. Malyshev, and M.M. Myshlyaev (1992). Reversible $\gamma \rightarrow \alpha + \delta$ transformation in zirconium deuteride, *Soviet Physics Solid State* **34**: 1182-1184.
- Beck, R.L. (1962). Zirconium-hydrogen phase system, *Trans. ASM* **55**: 542-555.
- Birk, S., H. Hanson, S. Marschman, B. Sindelar, K. Sorenson, and J. Wagner (2012). *Used Nuclear Fuel Storage and Transportation Research, Development and Demonstration Plan*, FCRD-FCT-2012-000053.
- Blomquist, J., J. Oloffson, A.-M. Alvarevol, and C. Bjerken (2010). Structure and Thermodynamic Properties of Zirconium Hydrides from First Principles. Preprint, University of Malme, Sweden.
- Bradbrook, J.S., G.W. Lorimer, and N. Ridley (1972). The Precipitation of Zirconium Hydride in Zirconium and Zircaloy-2, *J. Nucl. Mater.* **42**: 142-160.
- Carpenter, G.J.C. (1973). The Dilatational Misfit of Zirconium Hydride Precipitated in Zirconium, *J. Nucl. Mater.* **48**: 264-266.
- Cassidy, M.P., and C.M. Wayman (1980a). The Crystallography of Hydride Formation in Zirconium: I. The $\delta \rightarrow \gamma$ Transformation, *Metall. Trans. A* **11**: 47-56.
- Cassidy, M.P., and C.M. Wayman (1980b). The Crystallography of Hydride Formation in Zirconium: II. The $\delta \rightarrow \epsilon$ Transformation, *Metall. Trans. A* **11**: 57-67.
- Chakravartty, J.K., R. Kapoor, A. Sarkar, and S. Banerjee (2010). Dynamic Recrystallization in Zirconium Alloys, *Journal of ASTM International*, **7**: DOI: 10.1520/JAI103003
- Chauvy, C., P. Barberis, and F. Montheillet (2006). Microstructure transformation during warm working of β -treated lamellar Zircalloy-4 within the upper α -range”, *Mater. Sci. & Eng. A* **431**: 59-67.
- Chemelle, P., D.B. Knorr, J.B. Van Der Sande, and R.M. Pelloux (1983). Morphology and Composition of Second Phase Particles in Zircaloy-2, *J. Nucl. Mater.* **113**: 58-64.
- Cogswell, D., and W.C. Carter (2011). Thermodynamic phase-field model for microstructure with multiple components and phases: The possibility of metastable phases, *Phys. Rev. E.* **83**: 061602.
- Coleman, C.E., V. Grigoriev, V. Inozemtsev, V. Markelov, M. Roth, V. Makarevicius, Y.S. Kim, K.L. Ali, J.K. Chakravartty, R. Mizrahi, and R. Lalgudi (2010). The effect of microstructure on delayed hydride cracking behavior of zircaloy-4 fuel cladding—an international atomic energy agency coordinated research program, *J. ASTM Int.*, **7**: DOI: 10.1520/JAI103008.
- Cox, J.J., E.R. Homer, and V. Tikare (2013). Coupled microstructural-compositional evolution informed by a thermodynamic database using the hybrid Potts-phase field model, *Mater. Res. Soc. Symp. Proc.* 1524, DOI:10.1557/opl.2013.165 (2013).

- Danielson, P.E, and R.C. Sutherlin (2004). Metallography and Microstructures of Zirconium, Hafnium, and Their Alloys, Metallography and Microstructures, *ASM Handbook*, ASM International, **9**: 942–958.
- Ells, C.E. (1968). Hydride Precipitates in Zirconium Alloys (A review), *J. Nucl. Mater.* **28**: 129-151.
- Fong, R.W.L. (2013). Anisotropy factors from texture and mechanical strain in Zircaloy-4 fuel sheaths. *J. Nucl. Mater.* **440**: 288-297.
- Garde, A.M., H.M. Chung, and T.F. Kassner (1978). Micrograin Superplasticity in Zircaloy at 850°C, *Acta Metal.* **26**: 153-166.
- Geelhood, K., and C. Byere (2012). *Hydrogen in Nuclear Fuels Cladding*, presented at Cladding Hydride Modeling Meeting, February 2012, Sandia National Laboratories, Albuquerque, NM.
- Glazoff, M.V. (2013). Modeling of Some Physical Properties of Zirconium Alloys for Nuclear Applications in Support of UFD Campaign, IN/EXT-13-29581
- Hansen, G. (2012). 2D multimaterial heat conduction in cylindrical geometry with source, unpublished work.
- Hanson, B., H. Alsaed, C. Stockman, D. Enos, R. Meyer, and K. Sorenson (2011). *Gap Analysis to Support Extended Storage of Used Nuclear Fuel*, FCRD-USED-2011 000136, PNNL-20509.
- Hari Kumar, K.C., P. Wollants, and L. Delaey (1994). Thermodynamic assessment of the Ti-Zr system and calculation of the Nb-Ti_Zr phase diagram, *J. Alloys & Compounds* **206**: 121-127.
- Hill, R. (1948). A theory of the yielding and plastic flow of anisotropic metals, *Proc. Roy. Soc. A, London*, **193**: 281-297.
- Holm, E., J. Glazier, D. Srolovitz, and G. Grest (1991). Effects of lattice anisotropy and temperature on domain growth in the 2-dimensional potts-model, *Phys. Rev. A* **43**: 2662-2668.
- Holm, E.A., and C. Battaile (2001). The computer simulation of microstructural evolution, *JOM* **53**: 20-23.
- Humphreys, F.J., and M. Hatherly (2004). *Recrystallization and Related Annealing Phenomena*. Oxford: Elsevier.
- Hunt, C.E.L. (1975). *Anisotropic theory and the measurement and use of the anisotropic factors for Zircaloy-4 fuel sheaths*, in Transactions, 3rd Int. Conf. on Structural Mechanics in Reactor Technology, London, UK, **1**: Paper C 2/9.
- Hunt, C.E.L., and W.G. Newell (1979). Effect of β -phase heat treatment on the subsequent α -phase ballooning behavior of Zircaloy-4 fuel sheaths, in: Zirconium in the Nuclear Industry (4th Conf.), *ASTM STP* **681**: 447–464.
- IUCR (2014). <http://journals.iucr.org/j/issues/2014/01/00/he5611/he5611fig7.html>
- Jackson, M.A, (2013). Digital Representation Environment for Analyzing Microstructure in 3D, <http://dream3d.bluequartz.net/>

- Kearns, J.J., and C.R. Woods (1966). Effect of Texture, Grain Size, and Cold Work on the Precipitation of Oriented Hydrides in Zircaloy Tubing and Plate, *J. Nucl. Mater.* **20**: 241-261.
- Kearns, J.J. (1967). Terminal Solubility and Partitioning of Hydrogen in the Alpha Phase of Zirconium, Zircaloy-2 and Zircaloy-4, *J. Nucl. Mater.* **22**: 292-303.
- Kiran Kumar, N.A.P., J.A. Szpunar, and Z. He (2010). Preferential Precipitation of Hydrides in Textured Zircaloy-4 Sheets, *J. Nucl. Mater.* **403**: 101-107.
- Kolesnikov, A.I., A.M. Balagurov, I.O. Bashkin, et al. (1994). Neutron Scattering Studies of Ordered γ -ZrD. *J. Phys: Condensed Matter* **6**: 8977-8988.
- Krasevec, V. (1981). Transmission electron microscopy study of particles in Zircaloy-2, *J. Nucl. Mater.* **98**: 235-237.
- Kunz, F.W., & A.E. Bibb (1960). Habit Plane of Hydride Precipitation in Zirconium and Zirconium-Uranium, *Transactions of the American Institute of Mining and Metallurgical Engineers* **218**: 133-135.
- Lanzani, L., and M. Ruch (2004). Comments on the Stability of Zirconium Hydride Phases in Zircaloy, *J. Nucl. Mater.* **324**: 165-176.
- Li, H. J., D. Dunne, and N. Kennon (1999). Factors influencing shaper memory effect and phase transformation behavior of Fe-Mn-Si based shape memory alloys, *Mater. Sci. Eng. A*, **273**: 517-523.
- Lin, X., and G. Haicheng (1998). High cycle fatigue properties and microstructure of zirconium and zircaloy-4 under reversal bending, *Mater. Sci. & Eng. A* **252**: 166-173.
- Liu, W., Q. Li, B. Zhou, Q. Yan, and M. Yao (2005). Effect of heat treatment on the microstructure and corrosion resistance of a Zr-Sn-Nb-Fe-Cr alloy, *J. Nucl. Mater.* **341**: 97-201.
- Liu, Y.Z., Q. Peng, W.J. Zhao, and H.M. Jiang (2008). Hydride Precipitation by Cathodic Hydrogen Charging Method in Zirconium Alloys, *Mater. Chem. & Phys.* **110**: 56-60.
- Louthan, M.R., and R.P. Marshall (1963). Control of Hydride Orientation in Zircaloy, *J. Nucl. Mater.* **9**: 170-184 (1963).
- Marshall, R.P. (1967). Control of Hydride Orientation in Zircaloy by Fabrication Practice, *J. Nucl. Mater.* **24**: 49-59.
- Mishra, S., K.S. Sivaramakrishnan, and M.K. Asundi (1972). Formation of the Gamma Phase by a Peritectoid Reaction in the Zirconium-Hydrogen System, *J. Nucl. Mater.* **45**: 235-244.
- Motta, A.T., A. Yilmazbayhan, M.J. Gomes da Silva, R. J. Comstock, G.S. Was, J.T. Busby, E. Gartner, Q. Peng, Y.H. Jeong, and J.Y. Park (2007). Zirconium alloys for supercritical water reactor applications: Challenges and possibilities, *J. Nucl. Mater.* **371**: 61-75.
- Motta, A.T., and L.-Q. Chen (2012). Hydride Formation in Zirconium Alloys, *JOM* **64**: 1403-1408.

- Murgatroyd, R.A., and A. Rogerson (1980). An Assessment of the Influence of Microstructure and Test Conditions on the Irradiation Growth Phenomena in Zirconium Alloys, *J. Nucl. Mater* **90**: 240-248.
- Natesan, K., and W.K. Soppet (2004). *Hydrogen Effects on Air Oxidation of Zirlo Alloy*, NUREG/CR-6851, ANL-04/14.
- Nath, B., G.W. Lormier, and N. Ridley (1973). Relationship Between Gamma-Hydrides and Delta-Hydrides in Zirconium-Hydrogen Alloys of Low Hydrogen Concentration, *J. Nucl. Mater.* **49**: 262-280.
- Northwood, D.O., and U. Kosasih (1983). Hydrides and delayed hydrogen cracking in zirconium and its alloys," *Int. Mater. Rev.*, **28**: 92-121.
- Okamoto, H. (1992). Nb-Zr, *J. Phase Equilibria* **13**: 577-577.
- Okamoto, H. (1993). Cr-Zr, *J. Phase Equilibria* **14**: 768-768.
- Okamoto, H. (2006). Fe-Zr, *J. Phase Equilibria and Diffusion* **27**: 543-544.
- Ostberg, G. (1962). Determination of Hydride Solubility in Alpha Phase Zirconium, Zircaloy-2, and Zircaloy-4, *J. Nucl. Mater.*, **5**: 208-215.
- Payne, M.C., M.P. Teter, D.C. Allan, T.A. Arias, and J.D. Joannopoulos (1992). Iterative minimization techniques for ab initio total-energy calculations: molecular dynamics and conjugate gradients, *Rev. Mod. Phys.* **64**: 1045-1097.
- Pelton, A.D., L. Leibowitz, and R.A. Blomquist (1993). Thermodynamic analysis of phase equilibria in the iron-zirconium system, *J. Nucl. Mater.* **201**: 218-224.
- Perez, R.J. (2006). *Thermodynamic database for Zirconium Alloys*, Doctoral Thesis, Poyal Institute of Technology Stockholm, Sweden.
- Perovic, V., G.C. Weatherly, and C.J. Simpson (1983). Hydride Precipitation in α/β Zirconium Alloys, *Acta Metall.* **3**: 1381-1391.
- Perovic, V., G.C. Weatherly, and C.J. Simpson (1982). The Role of Elastic Strains in the Formation of Stacks of Hydride Predipitates in Zirconium Alloys, *Scripta Metal.* **16**: 409-412 (1982).
- Plimpton, S.J., C. Battaile, M. Chandross, E.A. Holm, A. Thompson, V. Tikare, G. Wagner, E. Webb, and X. Zhou (2009). *Crossing the Mesoscale No-Man's Land via Parallel Kinetic Monte Carlo*. Sandia Report: 2009-6226, Albuquerque, NM: Sandia National Laboratories.
- Puls, M.P. (2012). *The Effect of Hydrogen and Hydrides on the Integrity of Zirconium Alloy Compounds Delayed Hydride Cracking*. Springer.
- Qin, W., N.A.P. Kiran Kumar, J.A. Szpunar, and J. Kosinski, J. (2011). Intergranular δ -hydride nucleation and orientation in zirconium alloys, *Acta Mater.* **59**: 7010-7021.
- Root, J H., W.M. Small, D. Khatamian, and O.T. Woo (2003). Kinetics of the delta to gamma zirconium hydride transformation in Zr-2.5Nb, *Acta Mater.* **51**: 2041-2053.
- Roy, C., and J.G. Jacques (1969). (1017) Hydride Habit Planes in Single Crystal Zirconium, *J. Nucl. Mater.* **31**, 233-237.

- Sabol, G.P. (2005). Zirlo™ – An Alloy Development Success, *Journal of ASTM International*, **2**: 3-24.
- Santisteban, J.R., M.A. Vicente-Alvarez, P. Vizcaíno, A.D. Banchik, and J.D. Almer (2010). Hydride Precipitation and Stresses in Zircaloy-4 Observed by Synchrotron X-Ray Diffraction. *Acta Mater.* **58**: 6609-6618.
- SGnucl-SGTE (2004). “Ni-Zr” Data from SGnucl-SGTE nuclear database 2004. <http://www.crct.polymtl.ca/fact/documentation/SGnucl/Cr-Ni.jpg>
- Shishov, V.N., M.M. Peregud, A.V. Nikulina, Y.V. Pimenov, G.P. Kobylansky, A.E. Novoselov, Z.E. Ostrovsky, and A.V. Obukhov (2005). Influence of Structure Phase State of Zr Containing Zr Alloys on Irradiation-Induced Growth, *J. ASTM Int.*, **2**: 666-683 (2005).
- Sidhu, S.S., N.S.S. Murthy, F.P. Campos, and D.D. Zaubers (1963). Neutron and X-Ray Diffraction Studies of Nonstoichiometric Metal Hydrides, *Advances in Chemistry Series* **39**: 87-98.
- SPPARKS website: <http://spparks.sandia.gov/>
- Steuer, A., J.R. Santisteban, M. Preuss, M.J. Peel, T. Buslaps, and M. Harada (2009). Evidence of stress-induced hydrogen ordering in zirconium hydrides, *Acta Mater.* **57**: 145–152.
- Une, K., and S. Ishimoto (2009). Crystallographic Measurement of the Beta to Alpha Phase Transformation and Delta-Hydride Precipitation in a Laser-Welded Zircaloy-2 Tube by Electron Backscattering Diffraction, *J. Nucl. Mater.* **389**, 436-442.
- Une, K., K. Nogita, S. Ishimoto, and K. Ogata (2004). Crystallography of Zirconium Hydrides in Recrystallized Zircaloy-2 Fuel Cladding by Electron Backscatter Diffraction, *J. Nucl. Sci. Tech.* **41**: 731-740.
- Van der Sande, J.B., and A.L. Bement (1974). An Investigation of Second Phase Particles in Zircalloy-4 Alloys, *J. Nucl. Mater* **52**: 115-118.
- Wang, Z., U. Garbe, H. Li, R.P. Harrison, K. Toppler, A.J. Studer, T. Palmer, and G. Planchenault (2013). Hydride precipitation and its influence on mechanical properties of notched and unnotched Zircaloy-4 plates, *J. Nucl. Mater.* **436**: 84-92.
- Westlake, D.G. (1968). Habit Planes of Zirconium Hydride in Zirconium and Zircaloy, *J. Nucl. Mater.* **26**: 208-216.
- Whitmarsh, C.L. (1962). Review of Zircaloy-2 and Zircaloy-4 Properties Relevant to N. S. Savannah Reactor Design, ORNL-3281.
- Yamanaka, S., M. Miyake, and M. Katsura, M. (1997). Study on the Hydrogen Solubility in Zirconium Alloys, *J. Nucl. Mater.* **247**: 315-321.
- Zhao, Z., J.-P. Morniroli, A. Legris, A. Ambard, Y. Khin, L. Legras, and M. Blat-Yrieix (2008). Identification and Characterization of a New Zirconium Hydride, *J. Microscopy* **232**: 410-421.
- Zuzek, E., J.P. Abriata, A. San Martin, and F.D. Manchester (1990). H-Zr (Hydrogen-Zirconium), Binary Alloy Phase Diagrams, II Ed., Ed. T.B. Massalski, **2**: 2078-2080.

Zuzek, E, J.P. Abriata, A. San-Martin, and F.D. Manchester (2000). In: Manchester, F.D., editor. *Phase diagrams of binary hydrogen alloys*. Materials Park, OH, ASM International, p. 309.

4. APPLICATION AND VALIDATION OF THE HYBRID POTTS-PHASE FIELD MODEL FOR SIMULATION OF δ -ZrH_{1.5} PRECIPITATION IN THE α -Zr MATRIX

In the previous chapters, the general hybrid model was described, verified and validated, and it was further developed and adapted to simulate hydride precipitation in Zr-based claddings. While the development for adapting the model to simulate the processes specific to hydride precipitation was described piecewise and verification was continuously performed in Chapter 2, the final model will be validated in this Chapter using two cases. The first case will be the simulation of experiments performed by B. Clark and co-workers (Clark et al., 2013; Rajasekhara et al.) on hydride formation during hydrogen charging of Zr-alloys. The second validation case corresponds to the simulation of δ -ZrH_{1.5} precipitate reorientation with and without applied stress. While several published works (Ells, 1968; Louthan & Marshall, 1963; Bradbrook et al., 1972) will be used to validate these results, the primary experiments will be of Colas and co-workers (Colas et al., 2010).

4.1 Case I: δ -ZrH_{1.5} Hydride Formation during Hydrogen Charging

Previous studies, in Zircaloy-2 and Zircaloy-4 cladding materials (Sawatzky, 1960; Gulbransen & Andrew, 1954; Mallett & Albrecht, 1957; Kearns, 1972; Mazzolai & Ryll-Nardzewski, 1976), have examined hydrogen uptake and associated hydride formation under conditions involving extended periods of hydrogen charging for a wide range of temperatures (60 – 700°C) and homogenization treatments lasting for several hours. However, Clark et al., conducted a systematic experimental investigation to examine the hydride formation as a function of alloy composition. They examined Zircaloy-2, Zircaloy-4 and Zirlo™ with similar initial textures and grain sizes, but different compositions. Zirlo™ had a substantially higher niobium concentration relative to other two alloys as described in section 2-1.

Controlled hydrogen uptake in coupons, approximately 25 × 25 × 0.5 mm³ in dimensions, was achieved by aqueous charging these coupons using a process similar to the one described by Hindle et al. (Hindle & Slattery, 1966). Aqueous charging has been shown to be a viable method to introduce hydrogen in metals, and to generate hydrides in Zr-based alloys (Kiran Kumar et al., 2010; Choi et al., 1998; Iyer & Pickering, 1990; Liu et al., 2008) in a manner illustrated in Figure 4.1. The charging was carried out at approximately 90°C and at a nominal 100 mA/cm², which is a reasonable current density to induce perceptible hydrogen uptake within 1000 s (Kiran Kumar et al., 2010). The charging was performed for 100, 300 and 1000 s.

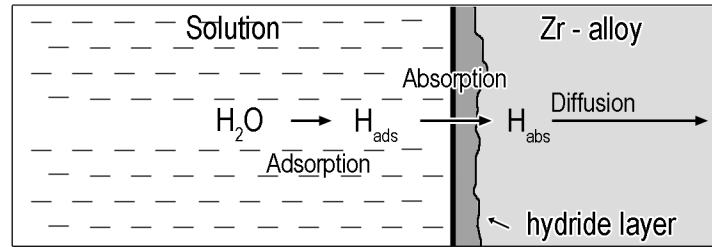


Figure 4.1: Schematic of the aqueous charging procedure used to drive hydrogen into the Zr-alloy at 90°C and current density of 100 mA/cm².

A novel approach was used to characterize the extent of hydrogen uptake, elastic recoil detection (ERD), which has been shown to be effective for depth-profiling light elements such as hydrogen (Tesmer et al., 1995; Khatamian & Manchester, 1989; Whitlow et al., 2000; Doyle & Brice, 1988). The thickness variations in the hydride layers were determined by using TEM on hydrogenated samples. The hydride layer thickness at a hundred equally spaced locations on the sample surface was measured to obtain the average thickness and standard deviation for the hydride layer in each sample. The crystallographic orientation of the hydrides with respect to the matrix in the samples was also investigated.

Overall hydride thicknesses in Zircaloy-2, Zircaloy-4 and ZirloTM, obtained with ERD, are shown in Figure 4.2. For all alloys, the hydride thicknesses increased as a function of charging duration. The hydride thicknesses in Zircaloy-2 and Zircaloy-4 were comparable for all charging durations. ERD results also showed that the hydride thickness in ZirloTM was an order of magnitude lower relative to the other two alloys for all of the charging durations. Selected area diffraction of hydride layer revealed that the hydride forming in all three Zr-alloys was δ -ZrH_{1.5} with FCC crystal structure.

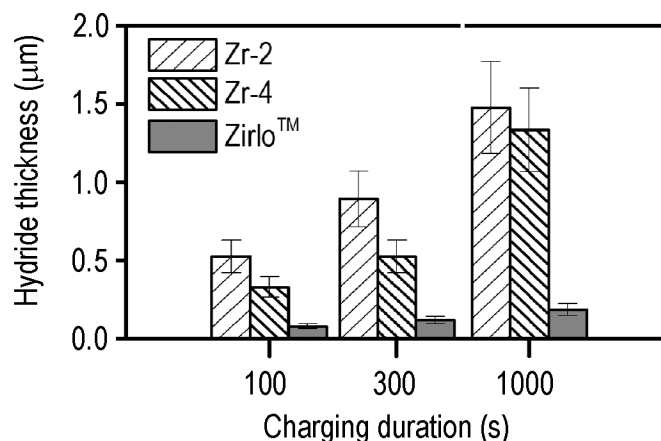


Figure 4.2: Hydride thicknesses as a function of hydrogen charging time measured by ERD on Zircaloy-2, Zircaloy -4 and ZirloTM.

The hydride layer thickness data for the Zircaloy-2 was analyzed in greater depth and fitted to identify the rate-controlling mechanism of the hydride growth layer. These data are plotted in Figure 4.3 on a log-log scale of hydride thickness as a function of hydrogen

charging time. Least-square fitting of these data yields a power law function with the relationship

$$d^2 = At \quad \text{Eq. 4-1}$$

where d is the hydride thickness, t is time and A is a materials constant related to the diffusivity. The exponent 2 indicates that the rate-controlling mechanism for hydride layer formation is diffusion of the hydrogen rather than the rate of phase transformation to form the hydrides which would yield an exponent of 1.

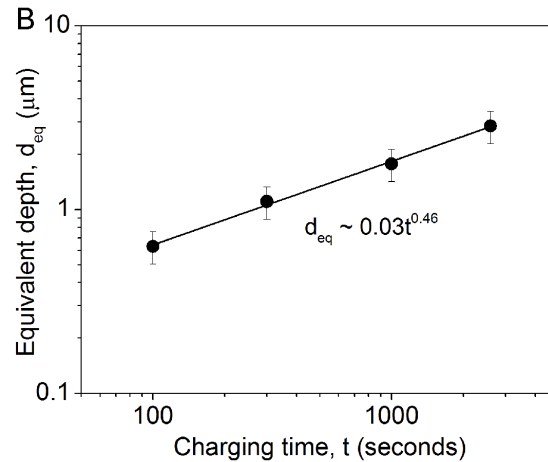


Figure 4.3: Hydride thicknesses as a function of hydrogen charging time measured for Zircaloy-2.

While an average hydride thickness is shown in Figure 4.2 and Figure 4.3, the variation in the hydride layer thickness was large as shown in Figure 4.4, wherein the hydride layer on Zircaloy-2 was imaged after different charging times. Closer examination of the hydride layer at the surface showed that the hydride layer in all three alloys consisted of individual $\delta\text{-ZrH}_{1.5}$ precipitates that the authors termed ‘lathes’, needle-shaped features that grew into the $\alpha\text{-Zr}$ grain. Furthermore, the same alignment orientation discussed in section 2.3, $\delta\text{-ZrH}_{1.5}$ precipitates growing in along the basal plane of the HCP $\alpha\text{-Zr}$ was found in these samples as well. The changes in hydride layer thickness occur with different thicknesses occurring in adjacent grains. Within a single $\alpha\text{-Zr}$ grain, the hydride thickness is nominally uniform, but then changes in adjacent grains. This suggests some crystallographic under-pinning for the hydride layer thickness

The hybrid model developed and described in Chapter 2 will be used to simulate this behavior to validate the model. While, the hydriding reaction is clearly diffusion rate-controlled, the reason for some of the other behaviors such as the variation in the hydride layer thickness is not understood. We will not only validate the model, but also demonstrate how it can be used to gain some understanding of the materials hydriding behavior observed in experiments.

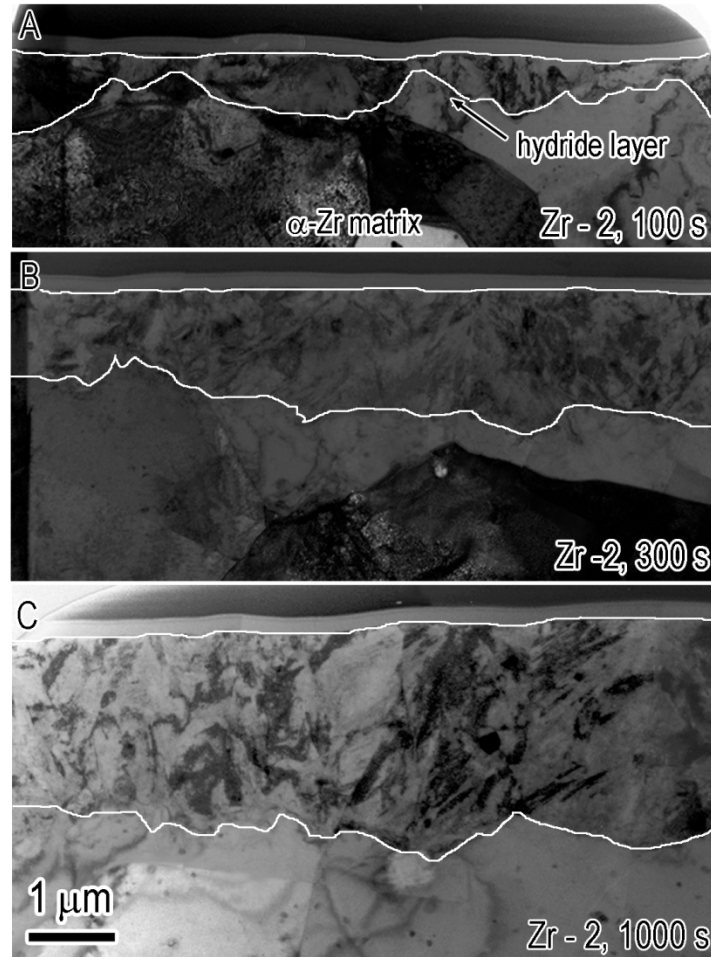


Figure 4.4: TEM micrographs showing hydride layer formation in Zircaloy-2 at 100, 300 and 1000 s of hydrogen charging.

4.1.1 Model Validation

The underlying microstructure for the validation simulation used a simple 2D polycrystalline microstructure, shown in Figure 4.5. Each different colored rectangle is a separate grain and the composition is homogeneously Zr with no H present in the initial microstructure. An infinite source of hydrogen is introduced on the bottom surface of the simulation space. The thermodynamic driving force for diffusion of hydrogen is given by the free energy curves for α -Zr and δ -ZrH_{1.5} in Figure 3.15. Note, that these free energies are for the temperature 300°C, while the hydrogen charging in the experiments were performed at 90°C, as the free energies curves for the two phases were not readily available for 90°C. The only difference in free energies for the two temperatures is expected to be a small relative shift in the minima of the two curves so that the solubility of H in α -Zr would be a little lower at 90°C as compared to 300°C. The overall diffusion behavior or diffusion kinetics for using the higher temperature free energies will not be altered and the validation of the model will remain the same. For these simulations, the volumetric chemical free energy is calculated by **Equation 3-6** and reproduced here for convenience

$$E_v = \mu_1 C_1 + \mu_2 C_2 \quad \text{Eq. 4-2}$$

In these simulations, the calculation of the free energy was performed using the numerical data generated by Glazoff's ThermoCalc calculations (Glazoff, 2013) directly and shown in Figure 4.6. The solid marks are for free energies calculated by ThermoCalc, the others are ones that were fabricated so that the free energies steadily increase away from their minima. This does not affect the thermodynamics or kinetics of the microstructural or compositional evolution, it only defines the equilibrium states by providing minima in free energy corresponding to those states. ThermoCalc was not used to generate the free energies in this region precisely for this reason, only the free energies near the minima are needed to calculate thermodynamic equilibrium states; the exact values of free energies far from the minima do not effect equilibrium phases or compositions. The chemical potentials, μ_1 and μ_2 , were calculated as

$$\mu_1 = E - \frac{\partial E}{\partial C_2} C_2 \quad \text{Eq. 4-3}$$

$$\mu_2 = E + (1 - C_2) \frac{\partial E}{\partial C_2}$$

with $\partial E / \partial C_2$ calculate by numerical differentiation as

$$\frac{\Delta E}{\Delta C_2} \quad \text{Eq. 4-3a}$$

and the free energy at a particular composition $E(C)$ is obtained by linear interpolation between the adjacent two numerical free energy values as

$$E(C) = E(C_1) + \frac{E(C_2) - E(C_1)}{C_2 - C_1} * [C - C_1] \quad \text{Eq. 4-3b}$$

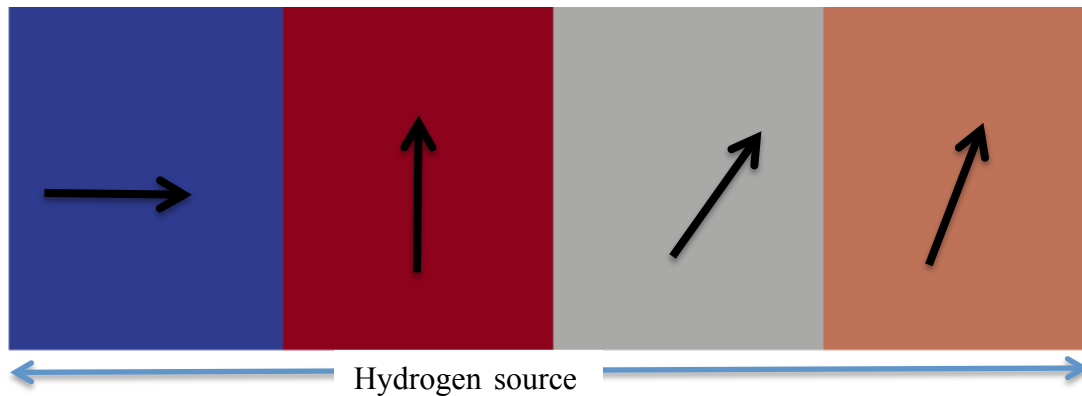


Figure 4.5: The initial microstructure used for the simulation of hydrogen charging of Zr-alloys with hydrogen source at the bottom. The arrows show the direction that is perpendicular to the basal plane.

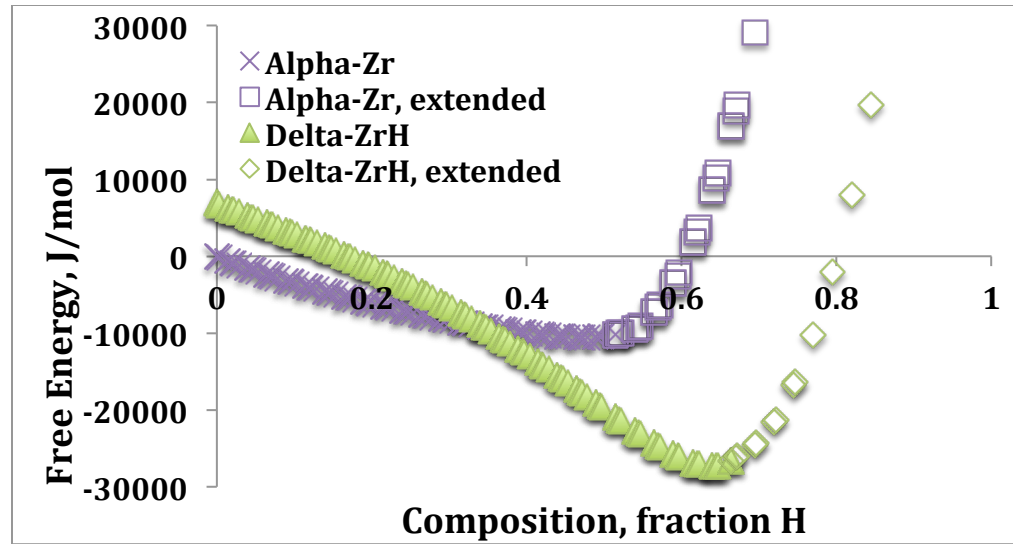


Figure 4.6: The numerical data obtained from ThermoCalc used for determining free energies and chemical potentials.

The simulation was performed with periodic boundary conditions in the X-direction, but not in the Y-direction as an infinite source of hydrogen is introduced at the bottom. Each color in Figure 4.5 is a different grain with the basal plane oriented in different directions to simulate the conditions present in the experiments. The simulation was performed with a uniform nucleation attempt rate with time in the entire microstructure and with a uniform and equal probability of δ -ZrH_{1.5} nucleation attempts in the entire microstructure. Grain growth was enabled between α -Zr grains as well as between δ -ZrH_{1.5} precipitates. At each MCS, 5% of the α -Zr sites, selected at random, attempted to nucleate δ -ZrH_{1.5} precipitates, all sites attempted a grain growth step or a phase growth step. The nucleation rate N is an input variable in the simulation. The Monte Carlo method is used to simulate nucleation. At each site, a random number that was uniformly distributed from $R \in (0, 1)$ was generated. If $R \leq N$, then a nucleation event was attempted by calculating the change in energy for a nucleus to form using the equation of state

$$E_{hybrid} = \sum_{i=1}^N (E_v(q_i, C_i) + \sum_{j=1}^n J(q_i, q_j) + \kappa_c (\nabla C_i)^2) \quad \text{Eq. 4-4}$$

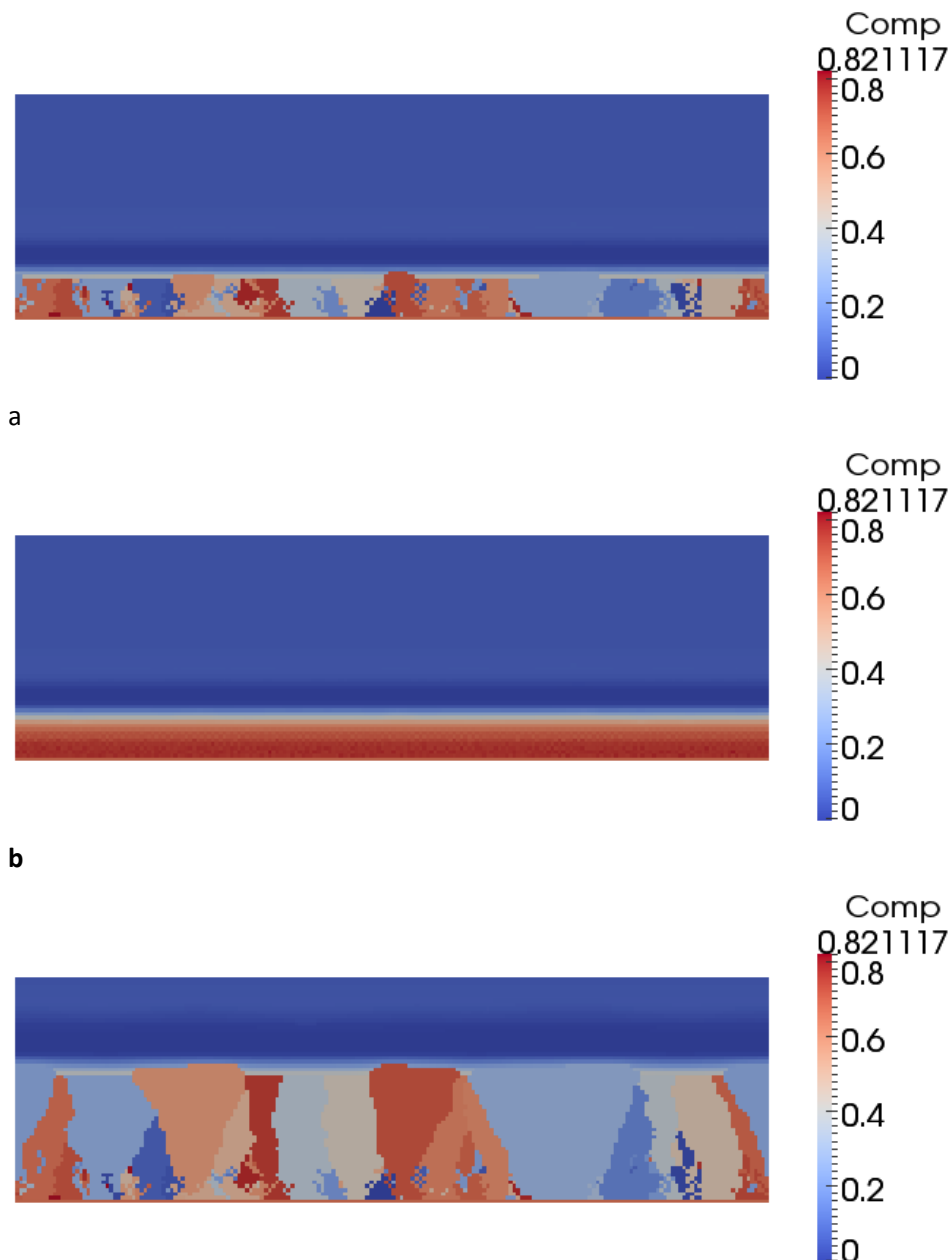
If $\Delta E \leq 0$, then the nucleus of a δ -ZrH_{1.5} precipitate formed. If $R > N$, then a precipitate grow event was attempted. If the site was an α -Zr site, and one of more of its neighbors was a δ -ZrH_{1.5} site, it attempted to phase transform to one of its neighbor selected at random. The change in energy for the precipitate to grow was calculated using **Equation 4-4** and again if the change in the system's energy decreased with $\Delta E \leq 0$, then the precipitate grew. For each MCS, the composition was updated 10 times at each sites using

$$\frac{\partial C}{\partial t} = \nabla \cdot M \nabla \frac{\delta E}{\delta C} \quad \text{Eq. 4-5}$$

The infinite source of hydrogen was simulated by solving the compositional evolution at all sites using **Equation 4-5**, but after each compositional update, the sites at the bottom

line of the simulation was reset to be $C = 0.67$, which is higher in hydrogen than the equilibrium composition of $\delta\text{-ZrH}_{1.5}$ and much higher than that of $\alpha\text{-Zr}$; thus providing a continuous supply of hydrogen for diffusion into the microstructure.

Uniform Diffusion Coefficient: The results of the first simulation with the parameters described above are shown in Figure 4.7, the microstructure and composition at two different times. The starting composition distribution is uniformly $C = 0$ with no H in the $\alpha\text{-Zr}$ cladding with microstructure shown in Figure 4.5. Diffusion of H is constant in all directions and phases in this simulation. The images show the $\delta\text{-ZrH}_{1.5}$ precipitates with the different colors corresponding to different precipitates at the bottom and the coloring in the $\alpha\text{-Zr}$ above indicates the composition as H-content in the $\alpha\text{-Zr}$ phase with the corresponding composition distribution in the entire microstructure.



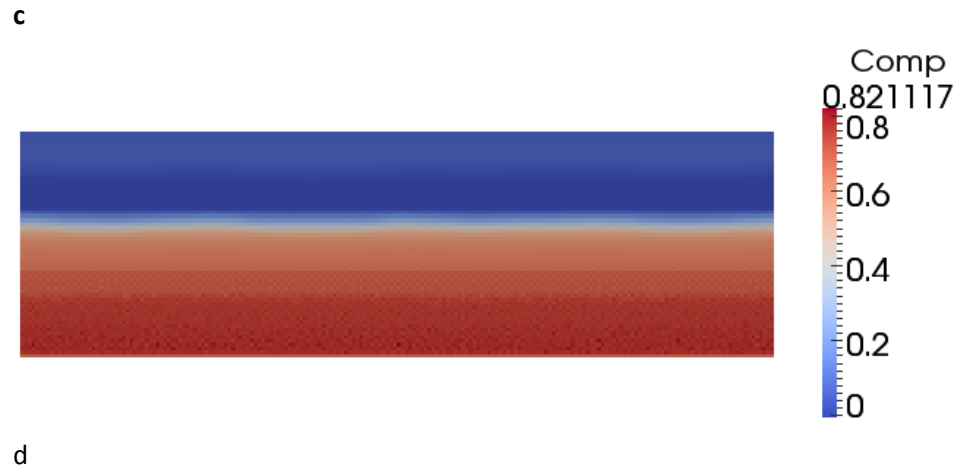


Figure 4.7: Hydrogenation of α -Zr by an infinite source of H at the bottom surface of the microstructure. (a) and (b) are at time $t = 10$ MCS and (c) and (d) are $t = 100$ MCS. (a) and (c) show the precipitates nucleating and growing from the bottom surface with the coloring at the top indicating the H concentration in α -Zr grains and (b) and (d) show the H concentration in the entire microstructure, both in the δ -ZrH_{1.5} precipitates and α -Zr grains.

For the conditions simulated, the behavior shown in Figure 4.7 is expected. The concentration of H diffusing is uniform across the microstructure in the X-direction, forming a continuous uniform concentration front that moves in the Y-direction. Note, that all precipitates nucleated at or very near the bottom surface, although nucleation was attempted at the same rate uniformly in the entire structure. This is consistent with the expected behavior as the highest driving force for nucleation is at supersaturated concentrations of H in the α -Zr matrix. At lower concentrations away from the bottom surface, the energy barrier of the interfacial energy prevents precipitates from nucleating, however, existing precipitates can grow as there is no interfacial energy barrier associated with the growth of precipitates. Furthermore, one notices that some nucleated precipitates grow and some simply nucleate, grow to a small size and then stop.

If the kinetics are diffusion controlled, then the thickness d of the precipitates must be proportional to diffusion time t as $d^2 \sim t$. This was quantified and found to hold as shown in Figure 4.8, a plot of the average precipitate thickness as a function of diffusion. The diffusion exponent of 1.93 ± 0.23 , obtained by least-squaring fitting of the data, is in good agreement with the expected diffusion exponent of 2.

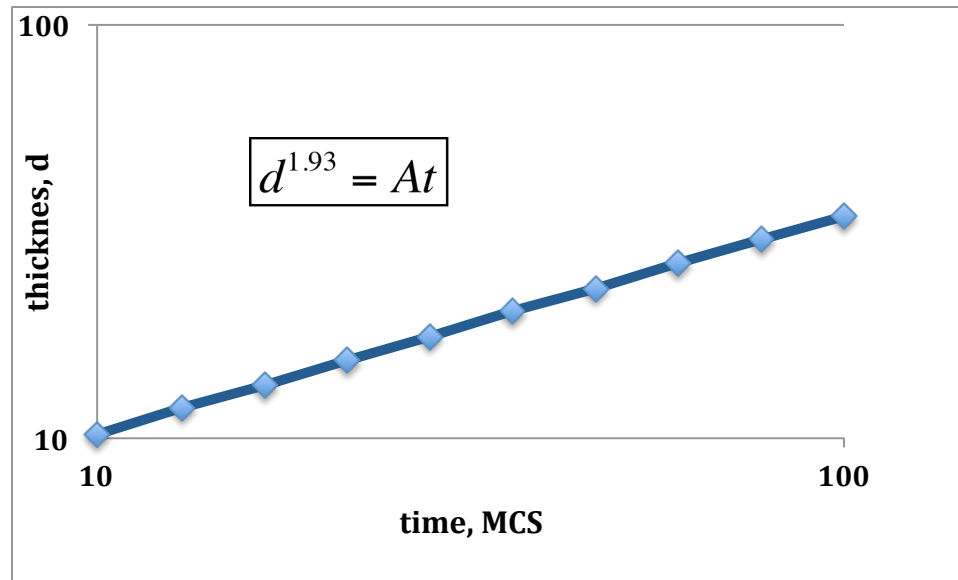


Figure 4.8: Average precipitate thickness as a function of diffusion time plotted on log scales. The diffusion exponent of 1.93, almost 2, indicates diffusion-controlled kinetics.

While these results validate the model as results predicted by analytic solution to the problem, they do not yield the results observed in the experiments, namely the difference in hydride layer thickness, which appears to follow the grain structure.

In Zircaloy-2 and Zircaloy-4, the layer thickness varied from grain to grain with the orientation of hydrides being a $\langle 111 \rangle_{\delta} // \langle 0001 \rangle_{\alpha}$ orientation relationship. This change in δ -ZrH_{1.5} layer thickness can originate from two cases, anisotropy in the diffusion kinetics or anisotropy in the interfacial growth kinetics. The experimental result show that the thickness of the hydride layer, d , scales with hydrogen charging time, t , as $d^2 \propto t$, indicating that hydride growth rate is diffusion-controlled, not interface growth-controlled. In the diffusion-controlled regime, two different diffusion behaviors can influence hydride layer growth, anisotropic diffusion in the α -Zr matrix phase or in the δ -ZrH_{1.5} hydride layer that is forming at the surface. These two will be tested next.

Differential diffusion in the α -Zr phase: The same simulation described with exactly the same parameters described for the uniform diffusion was performed, but with diffusion coefficients that were highly dependent on crystallographic direction in the α -Zr phase. The diffusion coefficient parallel to the basal plane was assigned values ranging from 0.1 to 0.001 of the diffusion coefficient perpendicular to the basal plane, $D_{//}(0001)_{\alpha} = 0.1 * D_{\perp}(0001)_{\alpha}$ to $0.001 * D_{\perp}(0001)_{\alpha}$. The diffusion coefficients in the δ -ZrH_{1.5} and perpendicular to the basal plane were the equal, $D_{//}(0001)_{\alpha} = D_{\delta}$ and the same as those used in the uniform diffusion case discussed above. The results obtained for the microstructural and compositional evolution were virtually identical for all values of $D_{//}(0001)_{\alpha}$ ranging from $0.1 * D_{\perp}(0001)_{\alpha}$ to $0.001 * D_{\perp}(0001)_{\alpha}$. The precipitate thickness growth kinetics were identical to the uniform diffusion case and the compositional profiles differed slightly $< 2\%$ at the precipitate growth front. The simulation results suggest that the precipitate growth rate is controlled by the diffusion of H through the δ -

ZrH_{1.5} layer and the diffusion in the α -Zr matrix layer have no effect on the hydrogen charging of the Zr-samples. This suggests that when the diffusion is much faster in one direction than the other, the grains aligned with the faster diffusion parallel to the growing hydride layer redistribute the hydrogen quickly leading to very uniform hydrogen content along the growing hydride layer front.

Thus, differential diffusion in the α -Zr phase cannot explain the variation in δ -ZrH_{1.5} layer from grain to grain as observed in the experiments. Testing more extreme differences in the diffusion coefficients is not supported by diffusion coefficients reported in the literature. Of the many who measured the diffusion coefficient, only Kearns (Kearns, 1972) reported a small anisotropy with the diffusion along the, c-axis perpendicular to the basal plane, being slightly lower than in the perpendicular direction. Sawatzky (Sawatzky, 1960) reported $D = 2.17 \times 10^{-3} \exp(8380/RT) \text{ cm}^2/\text{s}$ between 260 to 560 °C in Zircaloy-2 with $Q = 8380 \text{ cal/mol}$. Kearns (Kearns, 1972) reported diffusion coefficient of H in Zr, Zircaloy-2 and Zircaloy-4 to be very similar (cf. Figure 4.9); however, he reported small difference with orientation with D in the c-axis $< 2 \cdot D$ in the perpendicular directions. He reported $D = 6 \times 10^{-3} \exp(10,500/RT)$ in the 275 to 700 °C temperature range. Vostryakov et al. (Vostryakov et al., 2012) did not report any anisotropy in diffusion of H in Zr. Grosse et al. (Grosse et al., 2012) reported very similar diffusion coefficients as previous authors with no anisotropy with direction.

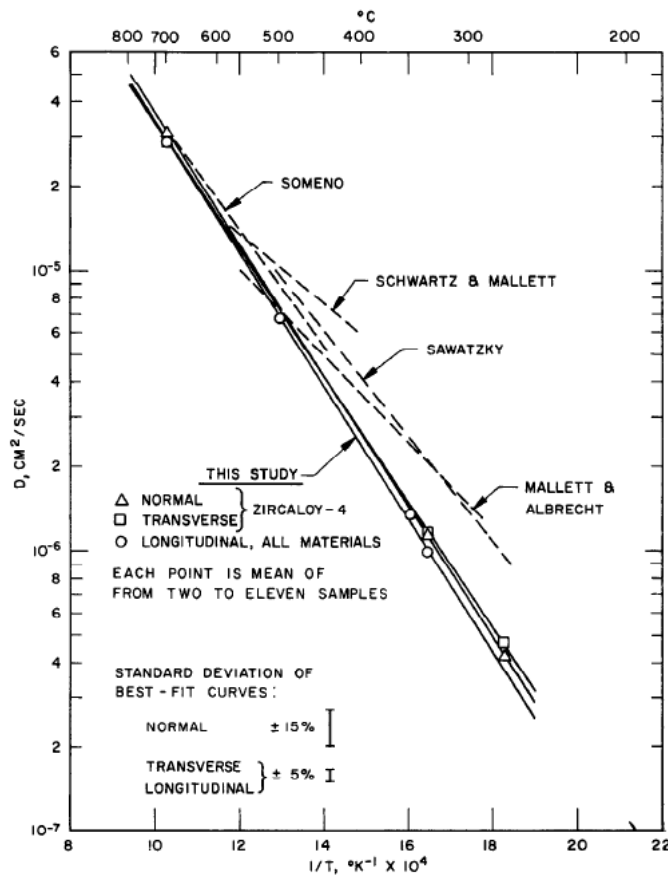


Figure 4.9: Summary of diffusion coefficients in Zircaloy-2 and Zircaloy-4 measured experimentally by many and summarize by Kearns (Kearns, 1972).

Differential diffusion in the δ -ZrH_{1.5} phase: Differential diffusion with crystallographically dependent diffusion coefficients in the δ -ZrH_{1.5} phase was investigated next. The same simulation method already described with exactly the same parameters used for the uniform diffusion and differential diffusion in α -Zr was performed. The initial microstructure was the one shown in Figure 4.5 with arrows showing the normal to the basal plane. However, this time the diffusion coefficients were highly dependent on crystallographic direction in the δ -ZrH_{1.5} phase. The diffusion coefficient parallel to the (111) plane in the FCC δ -ZrH_{1.5} precipitates was assigned values ranging from 0.1 to 0.001 of the diffusion coefficient perpendicular to the (111) plane, $D_{//}(111)_{\delta} = 0.1 * D_{\perp}(111)_{\delta}$ to $0.001 * D_{\perp}(111)_{\delta}$. The diffusion coefficients in the α -Zr and perpendicular to the (111) plane were equal, $D_{//}(111)_{\delta} = D_{\alpha}$, and the same as those used in the uniform diffusion case discussed above.

Crystallographically differential diffusion in δ -ZrH_{1.5} yielded behavior that was qualitatively different from previous results shown in Figure 4.7 for microstructural evolution. The microstructural and compositional evolutions are shown in Figure 4.10 for $D_{//}(111)_{\delta} = 0.01 * D_{\perp}(111)_{\delta}$. To repeat, the images show the δ -ZrH_{1.5} precipitates in different colors at the bottom and the coloring in the α -Zr above indicates the composition as H-content in the α -Zr phase. Accompanying these images are the corresponding composition distributions in the entire microstructure. Again nucleation of the precipitates occurred at the bottom surface where the hydrogen source was introduced for the same reasons discussed before; in this region the driving force for nucleation is highest as the supersaturation is also the highest. Again, nuclei do not form away from the hydrogen source as the existing precipitates grow before the supersaturation concentration of H in α -Zr matrix necessary for nucleation can be achieved. The hydride layer thickness varies considerably from grain to grain as shown in Figure 4.10. In these simulations, the diffusion is slowest in the direction perpendicular to the arrows in Figure 4.5, so the left region of the simulation has fast diffusion in the X-direction, but slow diffusion in the Y-direction and therefore the precipitates have the lowest thickness in this region.

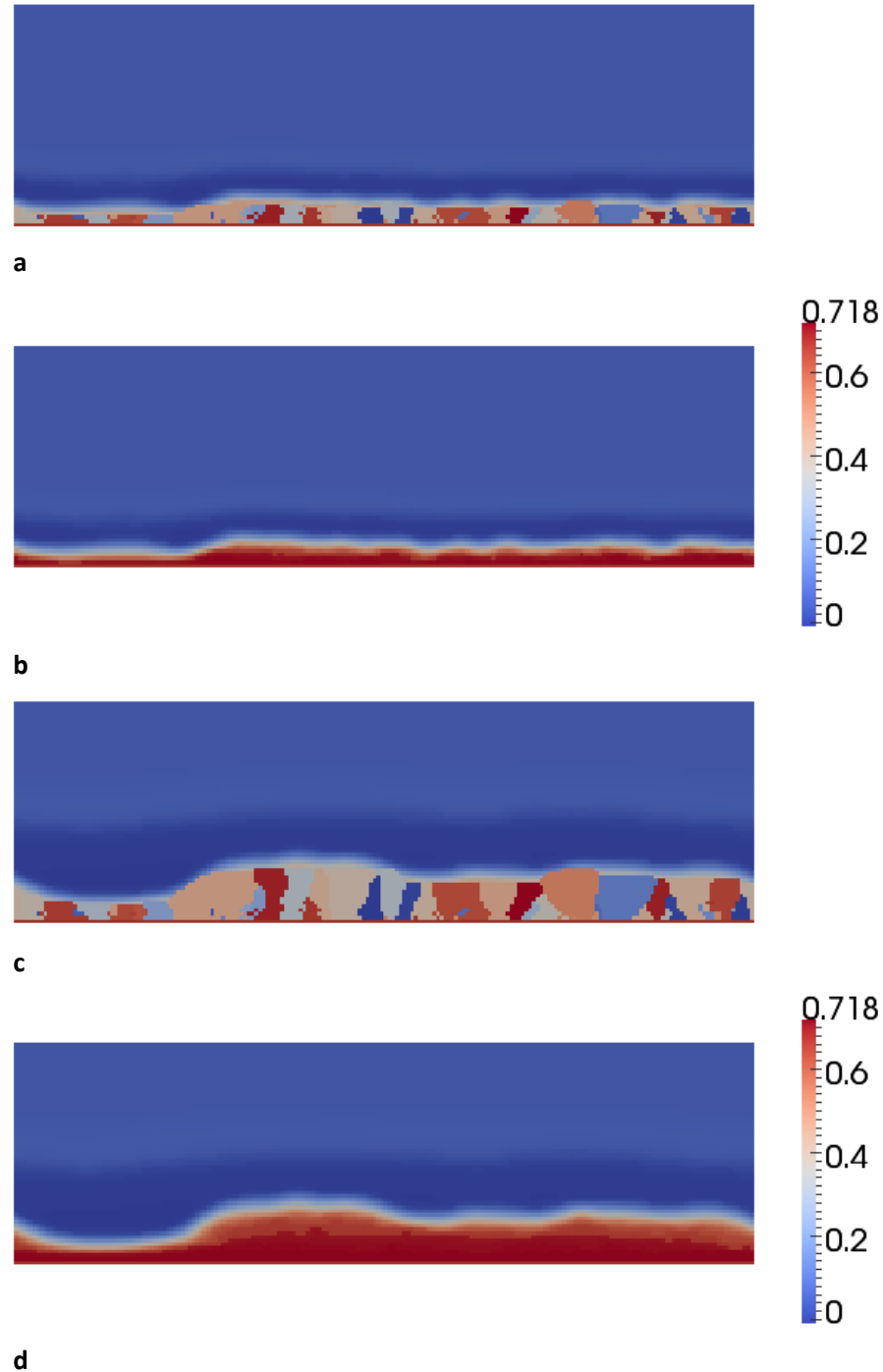


Figure 4.10: Hydrogen charging of the α -Zr by an infinite source of H at the bottom surface of the microstructure with differential diffusion in the δ -ZrH_{1.5} phase. (a) and (b) are at time $t = 10$ MCS and (c) and (d) are $t = 100$ MCS. (a) and (c) show the precipitates nucleating and growing from the bottom surface with the coloring at the top indicating the H concentration in α -Zr grains and (b) and (d) show the H concentration in the entire microstructure, both in the δ -ZrH_{1.5} precipitates and α -Zr grains.

The average precipitate thickness layer for this simulation is plotted in Figure 4.11. Again consistent with the results presented in Figure 4.10 and Figure 4.7, the hydride layer

forms at a much slower rate for the differential diffusion with $D_{//}(111)_{\delta} = 0.01 * D_{\perp}(111)_{\delta}$ than for the uniform diffusion. This is because the diffusion of H in the precipitates is much slower overall. In the region corresponding to the red grain, second from the left, the hydride layer grows the fastest as diffusion along the Y-direction is highest. However, it is still not as fast as that seen in the uniform diffusion case (can be seen by comparing Figure 4.7c and d to Figure 4.10c and d because the gradient in concentration in the X-direction $\partial C/\partial X$ is higher than in the Y-direction $\partial C/\partial Y$, so the flux of H in the fast diffusion grains is partly being diverted in the X-direction, perpendicular to the fast growth direction in the red grain. However, in the uniform diffusion case the concentration gradient in the X-direction $\partial C/\partial X = 0$ nominally and therefore the flux of H is almost entirely in the Y-direction. The other important feature is that the slope of the lines is almost identical indicating that diffusion-controlled kinetics dominate hydride layer growth even in the differential diffusion case. The exponent of the differential diffusion case was found by least-square fitting of the data to be 2.17, again in excellent agreement with the expected exponent of 2.0 for diffusion-controlled kinetics.

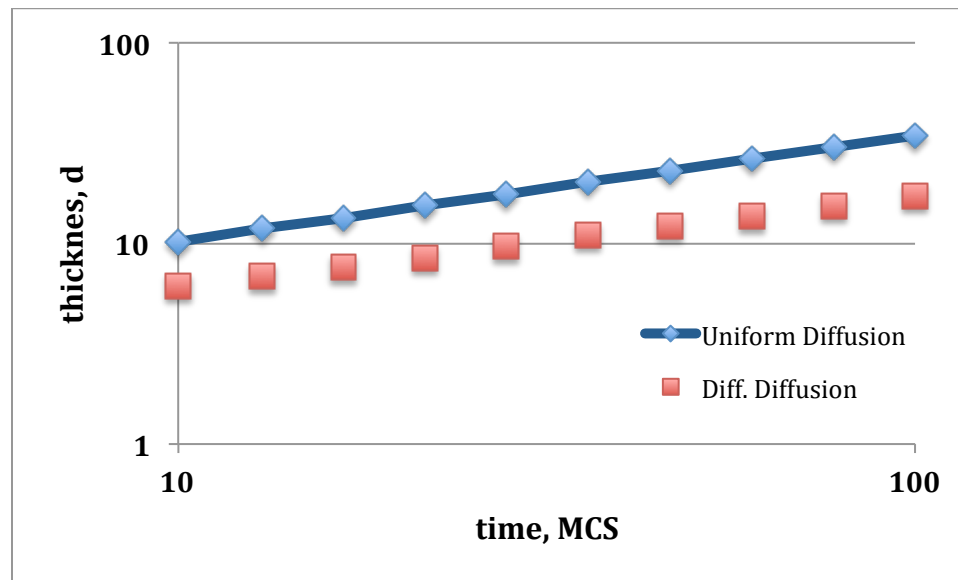


Figure 4.11: Average precipitate thickness as a function of diffusion time plotted on log scales for the uniform diffusion and differential diffusion in the δ -ZrH_{1.5} precipitate.

These simulations suggest that it is the differential diffusion in the growing hydride layer that leads to the behavior observed in the hydrogen charging experiments, specifically, the layer thickness kinetics with growth exponent of 2.0 and the variation in layer thickness from grain to grain. Furthermore, the differential diffusion necessary for the variation in layer thickness is large, a two orders of magnitude difference in diffusion coefficients. There is little evidence to suggest that such a large difference in diffusion coefficients exists for this process. Indeed, as pointed by Harkness and Young (Harkness & Young, 1973) who studied hydrogen diffusion in the δ phase, anisotropic diffusion in cubic crystals is extremely rare, thus, since δ phase zirconium hydride is FCC, and since the samples characterized experimentally were polycrystalline, uniform diffusion behavior is essentially assured. The diffusivity of hydrogen in zirconium hydride was measured over a relatively large range of temperatures and hydrogen concentrations by

Majer et al. (Majer et al., 1994). These authors, along with others (e.g. Terrani et al., 2009), found that the hydrogen diffusivity in δ -ZrH_{1.5±x}, is isotropic and its diffusion coefficient is $D_\delta = 7.29 \times 10^{-3} (1-C/2) \exp(-58.8[\text{kJmol}^{-1}]/RT[\text{K}]) \text{ cm}^2/\text{s}$, where C is the H/Zr ratio, R is the gas constant and T is temperature. Using such isotropic hydrogen diffusion coefficient, numerous experimental studies have successfully explained hydrogen diffusion behavior in the δ - phase of zirconium hydride (see, e.g.: Terrani et al., 2010; Hu et al., 2014).

However, it is well known that the presence of stress resulting in elastic strain of the crystal lattice can change the diffusion coefficients. In section 2.3, it was noted that large dilatation strains accompanied phase transition from α -Zr phase to δ -ZrH_{1.5}, with the largest strain occurring normal to the basal plane of the HCP α -Zr matrix as

$$\varepsilon = \begin{bmatrix} 0.048 & 0 & 0 \\ 0 & 0.048 & 0 \\ 0 & 0 & 0.072 \end{bmatrix}$$

Accompanying the transformation is the formation of large compressive stresses inside the δ -ZrH_{1.5} precipitates (*ca.* -450 ± 90 MPa as determined by Santisteban et al., 2009), which can and do reduce H diffusivity. Hydrogen diffusion induced by stress gradients was observed in various studies about hydrogen-induced delayed hydride cracking (Northwood & Kosasih, 1983) and in studies by Kammenzind et al. (Kammenzind et al., 1998) or by Menibus and co-workers (de Menibus et al., 2014). As discussed in these studies and the review by Puls (Puls, 2012), hydrogen diffuses towards an elastic stress field that is tensile in character, away from large compressive stresses that reduce hydrogen diffusivity.

Since these precipitates are forming at the surface of the Zr-claddings, when the large strain direction is parallel to the surface, the material of either side will restrict expansion and therefore result in compression of the precipitate with elastic straining of the lattice. In contrast, when the large strain direction is perpendicular to the surface, there is only material on one side and not the other, so the expansion of the precipitate is much less restricted resulting in much lower stresses in the precipitate with lower stress. This difference in compressive stress of the precipitates with the different grain orientations is suggested as the cause for the change in δ -ZrH_{1.5} layer thickness from grain to grain in the Zr-claddings observed by Clark et al. (Clark et al., 2013) in their experiments.

4.1.2 Discussion

Previous studies have shown that hydrogen uptake and hydride formation in Zr-based cladding materials depend on numerous parameters such as, for example, the hydrogen concentration, the fabrication processes of cladding materials, the heat treatment procedure, the time and temperature used for hydrogen charging, and the presence or absence of stress in the materials. Therefore, it comes as no surprise that model adjustment is usually necessary to reproduce the specific conditions of a given experiment designed to study of hydrogen uptake and hydride formation.

Although further development of the present model is necessary to capture the complexity of experimental conditions, the present model was validated by the experimental results of Clark et al., as discussed above. This model also provides

understanding of the observed behaviors in other studies of hydrogen uptake and hydride formation in Zr-based cladding materials, under a rich variety of conditions and using different experimental methods (see e.g.: Sawatzky, 1960; Gulbransen & Andrew, 1954; Mallett & Albrecht, 1957; Kearns, 1972; Mazzolai & Ryll-Nardzewski, 1976; Kiran Kumar et al., 2010; Choi et al., 1998; Iyer & Pickering, 1990; Liu et al., 2008).

For the conditions of uniform isotropic diffusion, the behavior shown in Figure 4.7 is expected. The concentration of H diffusing is uniform across the microstructure in the X-direction, forming a continuous uniform concentration front that moves in the Y-direction. Note, that all precipitates nucleated at or very near the bottom surface, although nucleation was attempted at the same rate uniformly in the entire structure. This is consistent with the expected behavior as the highest driving force for nucleation is at supersaturated concentrations of H in the α -Zr matrix. At lower concentrations away from the bottom surface, the energy barrier of the interfacial energy prevents precipitates from nucleating, however, existing precipitates can grow as there is no interfacial energy barrier associated with the growth of precipitates. Furthermore, some nucleated precipitates grow; while others simply nucleate, grow to a small size and then stop. This behavior of uneven hydride growth was observed for both the isotropic and anisotropic diffusion cases.

If the kinetics are diffusion controlled, then the thickness d of the precipitates must be proportional to diffusion time t as $d^2 \sim t$. However, for highly anisotropic diffusion such as the behavior simulated in Figure 4.10, it was not clear that the $d^2 \sim t$ relationship with a layer growth exponent of 2 would be obtained. These simulations have shown that the diffusion controlled kinetics even with highly anisotropic growth results in the layer growth exponent of 2, supporting the assertion that the hydride layer growth observed by Clark et al. is diffusion controlled.

We attribute the anisotropy in diffusion in the hydrogen charging experiments to the stress state of the hydride precipitates and their orientation. The hydride that have their high expansion direction along the basal pole of the underlying matrix grain perpendicular to the surface will be elastically constrained the most and experience high compressive stresses. It is well known that diffusion is affected by elastic stress and in the case of interstitial diffusion such as that in δ -ZrH_{1.5}, diffusion will be slower when a compressive stress is applied (Aziz, 1997). The large dilatation accompanying precipitation is thought to be the cause of the variation in layer thickness seen in the experiment and reproduced in the simulation.

4.2 Case II: Precipitation and Reorientation of δ -ZrH_{1.5} Precipitates

Many studies (see, e.g.: Colas et al., 2010; Hanson et al., 2011; Birk et al., 2012; Puls, 2012, and references therein; Min et al., 2014) have focused on the formation and reorientation of δ -ZrH_{1.5} precipitates by characterizing samples after precipitate formation using metallographic techniques. These have been reviewed in section 2.5 in some detail. For this validation exercise, we focus on the work of Colas et al. (Colas et al., 2010), who used X-ray radiation generated by a synchrotron to study precipitate formation in situ during heating and cooling to study precipitate formation and dissolution. They studied hydriding behavior of both Zircaloy-2 and Zircaloy-4. First, the

basic microstructures of the as-fabricated samples were characterized and found to be consistent with results reported previously. The grains were elongated in the RD in Zircaloy-4, but equiaxed in the Zircaloy-2 samples. The grain sizes of the two were different with Zircaloy-2 having larger grains of 20 μm than that of Zircaloy-4, which is typically reported to be 8 μm . Both Zr-alloys had strong texture with the basal planes aligned in the RD.

Samples were charged with hydrogen by high temperature gas diffusion. First the native oxygen layer was removed and thin layer of nickel was deposited to prevent reoxidation of the surface. The samples were then heated treated in a 12%-H and 88%-Ar gas atmosphere at 450°C in several cycles with total time at 450°C ranging up to 3 h. At this low temperature, no recrystallization or other changes to the microstructure were expected or seen. The H content in Zircaloy-2 varied from 80 to 600 ppm by weight and ~600 ppm wt. in Zircaloy-4. The initial characterization of the hydride precipitate orientation in both Zr-alloys is with the precipitates lining up in the circumferential direction as shown in Figure 4.12.

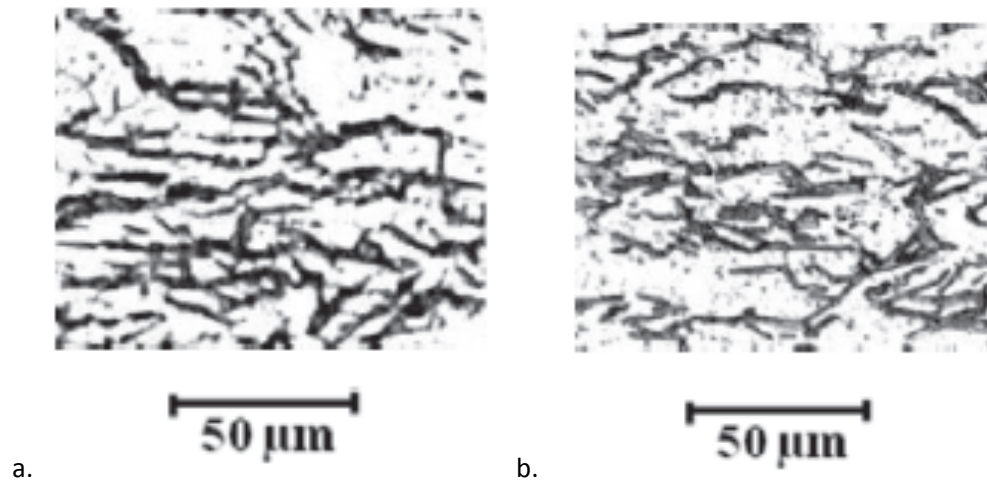


Figure 4.12: Optical images showing $\delta\text{-ZrH}_{1.5}$ precipitates in (a) Zircaloy-2 and (b) Zircaloy-4 with H content of 600 ppm wt. (Colas et al., 2010)

X-ray diffraction, done in transmission mode, was able to determine if hydride precipitates were present and the intensity of the diffracted signal was used to determine the amount of hydride present in region of approximately 0.3 mm x 0.33 mm x 0.5mm. The diffraction pattern resulted in diffraction rings and sampling the intensity in different angular regions of the diffract pattern was used to determine the orientation of precipitates in the RD or the TD. Figure 4.13 shows the different directions in a cladding schematically and will aid in the discussion that follows.

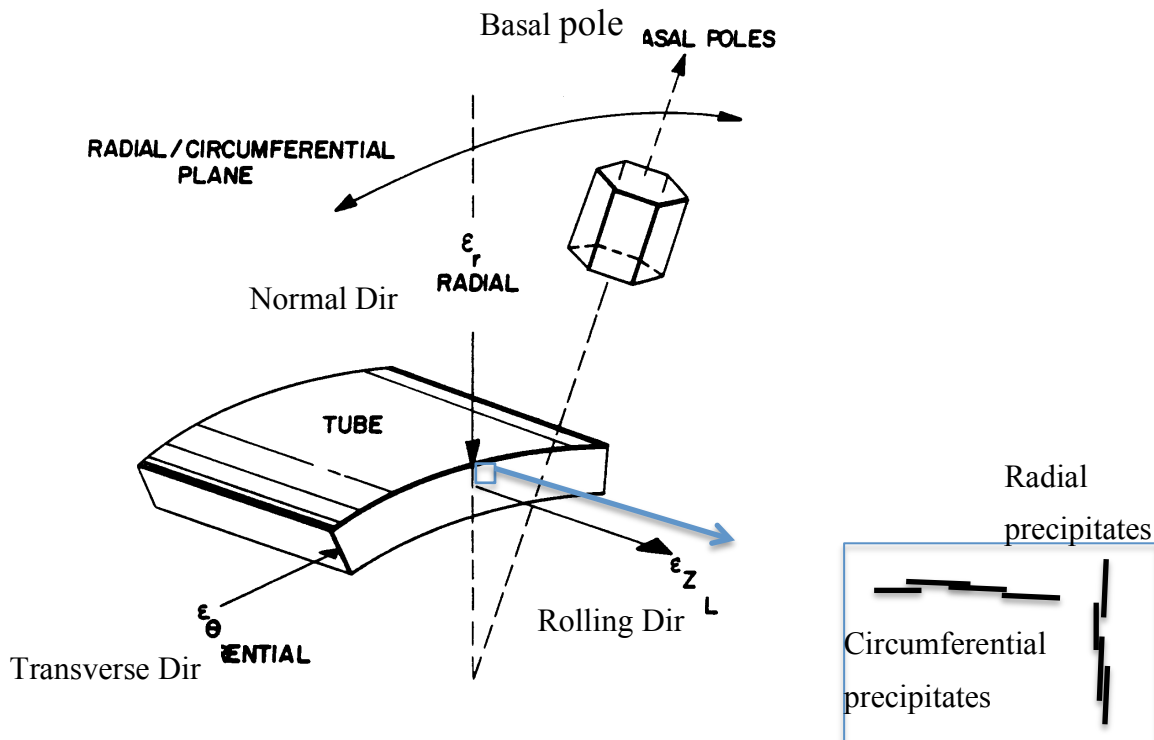


Figure 4.13: A schematic diagram showing the transverse, normal and rolling directions in a cladding. The preferred orientation of the basal pole is in the normal direction with the basal plane aligning preferentially in the rolling direction. The orientation of circumferentially and radially oriented precipitates is also shown in the expanded view of the square.

Colas et al. (Colas et al., 2010) reported precipitation of circumferential precipitates when cooling from high temperatures ranging from 390 to 542°C down to room temperature with no applied stress to low stresses. Radial precipitates formed when stresses of 85 MPa and higher were applied perpendicular to the radial direction. Optical micrographs of these precipitates forming in Zircaloy-4 with 600 wt ppm H with no applied stress and applied stress of 85 MPa are shown in Figure 4.14. The first case, with no applied stress shown precipitates oriented in the circumferential direction and the second image shows many precipitates reoriented in the radial direction. While, Zircaloy-4 results are shown here, similar results were obtained for Zircaloy-2 with reorientation of precipitates in the radial direction occurring at stress of 80 MPa and higher.

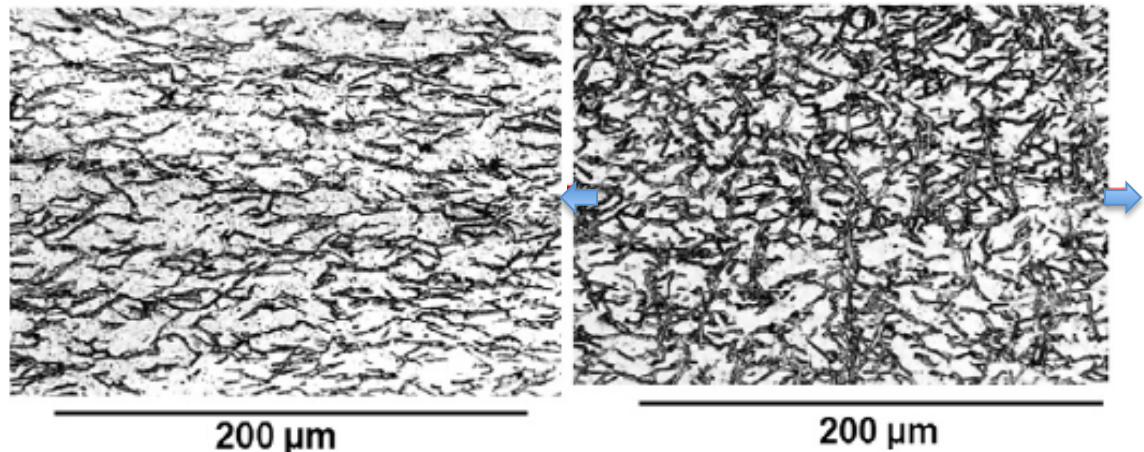


Figure 4.14: Optical micrographs showing precipitate orientation in Zircaloy-4 with and without applied stress. The arrows indicate applied uniaxial stress of 85 MPa (Colas et al., 2010).

4.2.1 Model Validation

We seek to reproduce the precipitate reorientation using the hybrid Potts-phase field model adapted to simulate hydride precipitation in Zr-based claddings. For this validation exercise, we validate the model in steps; the first set of simulation is of δ -ZrH_{1.5} precipitation in Zircaloy-4-like microstructure without crystallographic texture with and without stress applied perpendicular to the RD. The second set is of δ -ZrH_{1.5} precipitation in the best Zircaloy-4 microstructure that could be generated based on information available in the published literature. Again, the precipitation simulations were performed with and without stress applied.

Precipitation in Zircaloy-4 with no texture and no stress The underlying microstructure for the simulation was generated as described in section 2.1.1 using the software package, Dream3D (Jackson, 2013). As explained before, Dream3D is a free, open and modular software package that allows users to construct microstructures digitally. The synthetic microstructures with the characteristics of Zircaloy-4 had an average grain size of 10 μm in the RD with a standard deviation of 1 μm . While there are little data on grain size and structure, there are even less on grain size distributions and their standard deviations. Thus, the choice of standard deviation is estimated from existing knowledge of rolled metals microstructures. The average elongation in the rolled direction of the synthetic microstructure is also 2x as compared to the transverse and NDs; this is based on simple measurements of the microstructures found in the published literature. The digitally generated Zircaloy-4 microstructure is shown in Figure 4.15. Notice that grains are elongated in the RD and appear equiaxed in the perpendicular direction. This is again consistent with known characteristics of Zircaloy-4.

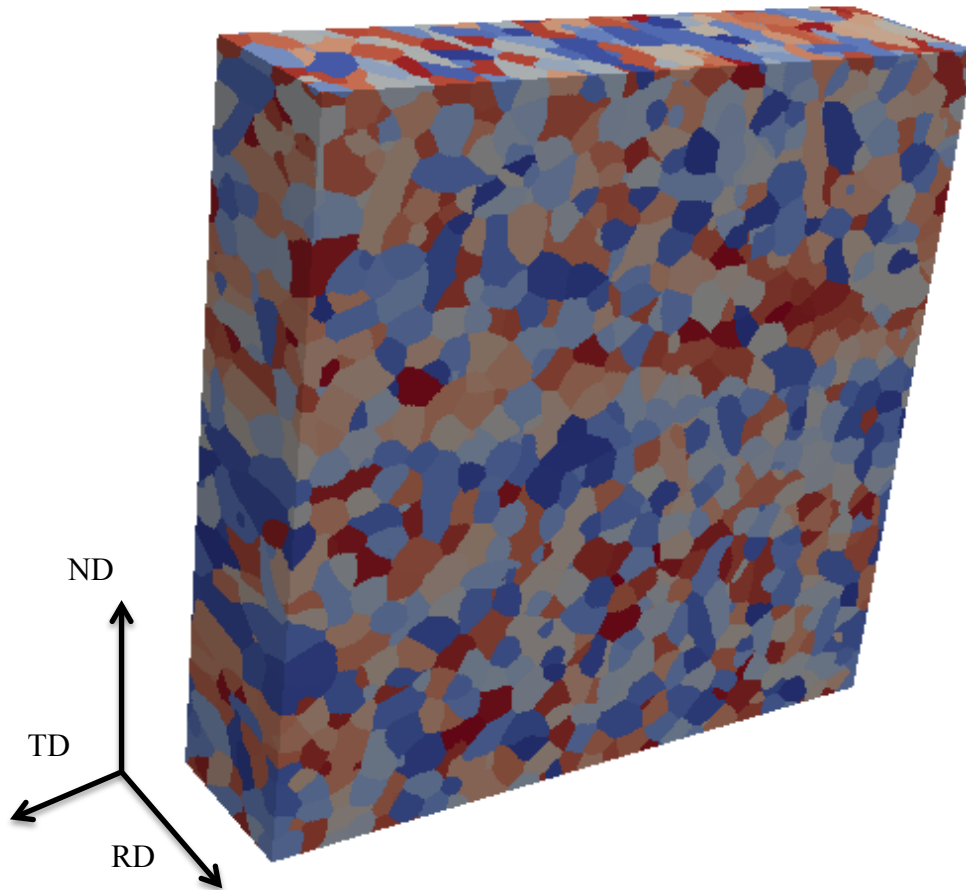


Figure 4.15: Digitally generated Zircaloy-4 microstructure with the rolling, normal and transverse directions indicated. See Figure 4.13 for definitions of the three directions. The size of this volume is 100 x 100 x 25 μm .

The simulation parameters are as follows. The simulation starts with the grain structure shown above, with randomly oriented grains with no crystallographic texture. All the hydrogen present is dissolved in the α -Zr matrix at a supersaturation of 5 mol% which is approximately 500 ppm wt. δ -ZrH_{1.5} precipitates can only grow in the crystallographic correct relationship with the underlying α -Zr grain, that is the precipitate grow in the basal plane of the HCP α -Zr. Nucleation of new precipitates is attempted at a uniform rate with equal probability everywhere in the microstructure. No preference is given to regions near grain boundaries or any other region of microstructure. The conditions assumed for the simulations are that all the hydrogen is dissolved at some high temperature, and then it is cooled instantaneously to 300°C and precipitate nucleate and grow. Nucleation attempt rate is constant and growth rate is controlled by the rate of diffusion of hydrogen to the growing precipitates. The volumetric chemical free energy is calculated by **Equation 4-2** and with the exact values of the chemical potentials μ_1 and μ_2 , were calculated using **Equation 4-3** with the method described to obtain free energy directly from the numerical values of the free energies generated by ThermoCalc for the Zr-H system at 300°C. The nucleation attempt rate N used for these simulation is $N = 0.05$ and nucleation is simulated using the same method described in Case 1 using the standard Metropolis algorithm. Precipitate growth was also simulated using the same

method described in Case 1. Grain growth of the α -Zr was not simulated as grain growth does not occur at this low temperature. At each MCS, 5% of the α -Zr sites attempted nucleation, if the change in energy calculated using **Equation 4-4** was 0.0 or less, the nucleation was successful. If a precipitate failed to nucleate at that site, then a precipitate growth step was attempted by each α -Zr site using the Potts methods in conjunction with **Equation 4-4** to determine if growth occurred or not. Following these nucleation or growth attempts by each site, the composition evolution was treated using **Equation 4-5**.

The microstructural and compositional evolution resulting from this simulation is shown in Figure 4.16. It shows δ -ZrH_{1.5} precipitates nucleated in (a) and grew to their final size and number in (c). The composition in (b) and (d) show high hydrogen content in the precipitates and a region of depleted hydrogen immediately around the precipitate, which is consistent with diffusion-controlled precipitate growth. These results are very similar to those presented in Chapter 2, with precipitates with each grain having only three different orientations, but the random orientation of the grains gives large differences in the orientation between grains. While nucleation attempt rate remains constant throughout the simulation, most precipitates nucleate early in the simulation when the supersaturation of hydrogen in the matrix is high. After that it is energetically favorable for existing precipitates to grow rather than for new ones to nucleate. The primary difference shown here is the scale of these simulations is considerable larger and allows one to obtain engineering scale behavior of the precipitates.

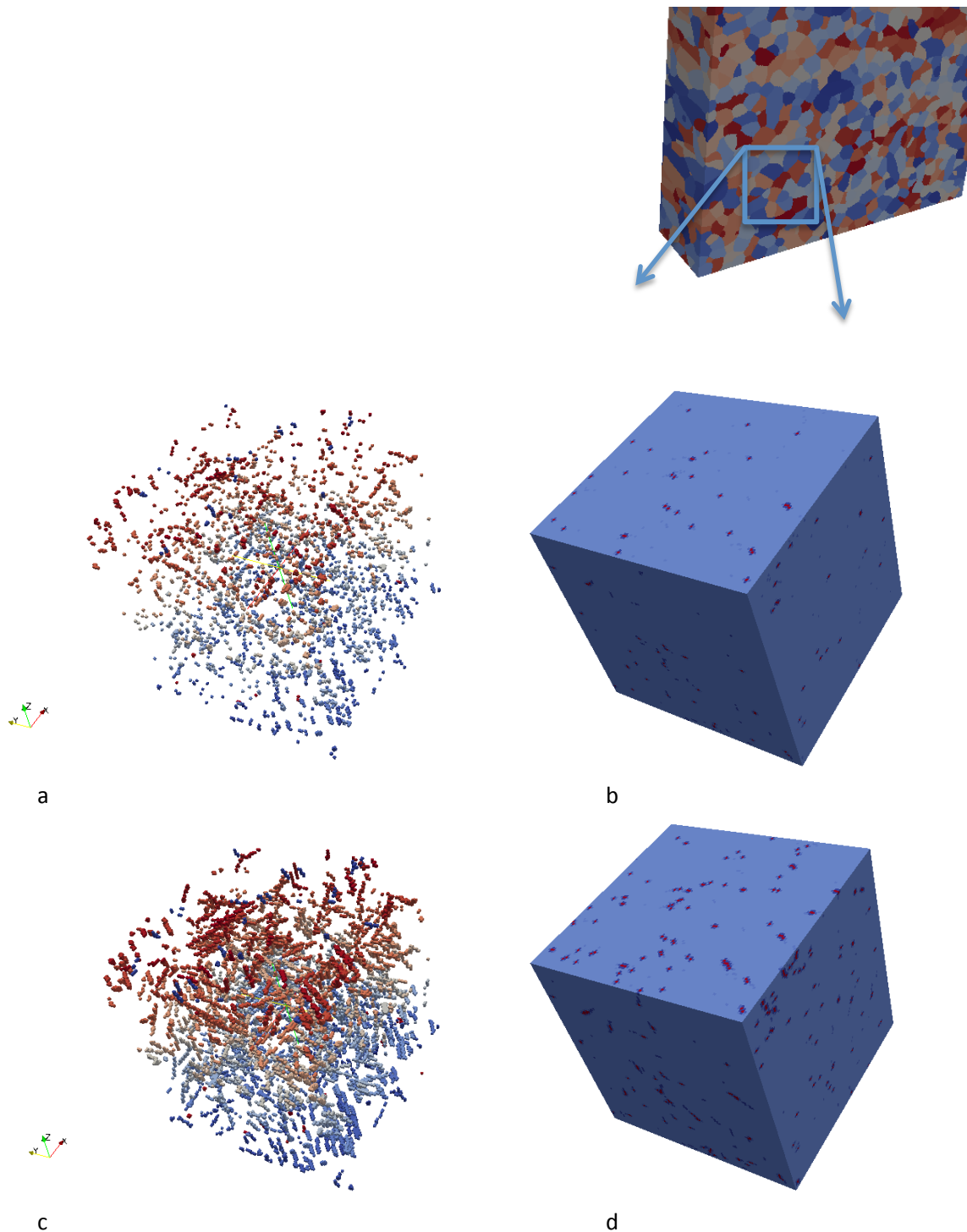


Figure 4.16: A small portion ($10 \times 10 \times 10 \mu\text{m}$ shown by the inset at the top right) of the simulation is imaged as imaging the total microstructure would be overwhelming amount of data at time $t = 20$ MCS in (a) and (b) and $t = 100$ MCS in (c) and (d). All the precipitates in that volume are shown in (a) and (c) with each color corresponding to a precipitate. The compositions corresponding to that image at the surface of the volume is shown in (b) and (d) with the red areas are high in hydrogen and are the precipitates.

Precipitation in Zircaloy-4 with no texture and uniaxial stress applied Exactly the same simulation with the same microstructure, composition, free energies, temperature history, and simulation parameters was performed with uniaxial, constant stress applied perpendicular to the radial direction. As described in Section 3.3.1, stress was introduced by adding a strain energy term E_s to the free energy given in **Equation 4-4**. The strain energy of the precipitate was related to the direction of applied stress as

$$E_s = \varepsilon \sin(\phi - 45)$$

Eq. 4-6

where ε is a constant and is a function of the applied stress and strain accompanying hydride nucleation or growth and ϕ is the misorientation angle between the direction of the applied stress and precipitate growth direction. In this method of calculation, precipitates that are perpendicular to the applied stress direction have an energetic advantage to nucleate and grow; while those parallel to the applied stress have an energetic penalty and those at 45° are not affected by the applied stress. Thus precipitates that are perpendicular to the applied stress nucleate and grow preferentially.

The results of this simulation are shown in Figure 4.17. Again a small section of the entire microstructure is imaged with all the precipitates forming with that volume imaged with stress applied in X-direction, along the circumferential direction, and in Y-direction along the radial direction. These results show that grains favorably oriented with their basal planes perpendicular to the applied stress form precipitates under the particular applied stress, thus giving δ -ZrH_{1.5} precipitate reorientation under different applied stress conditions.

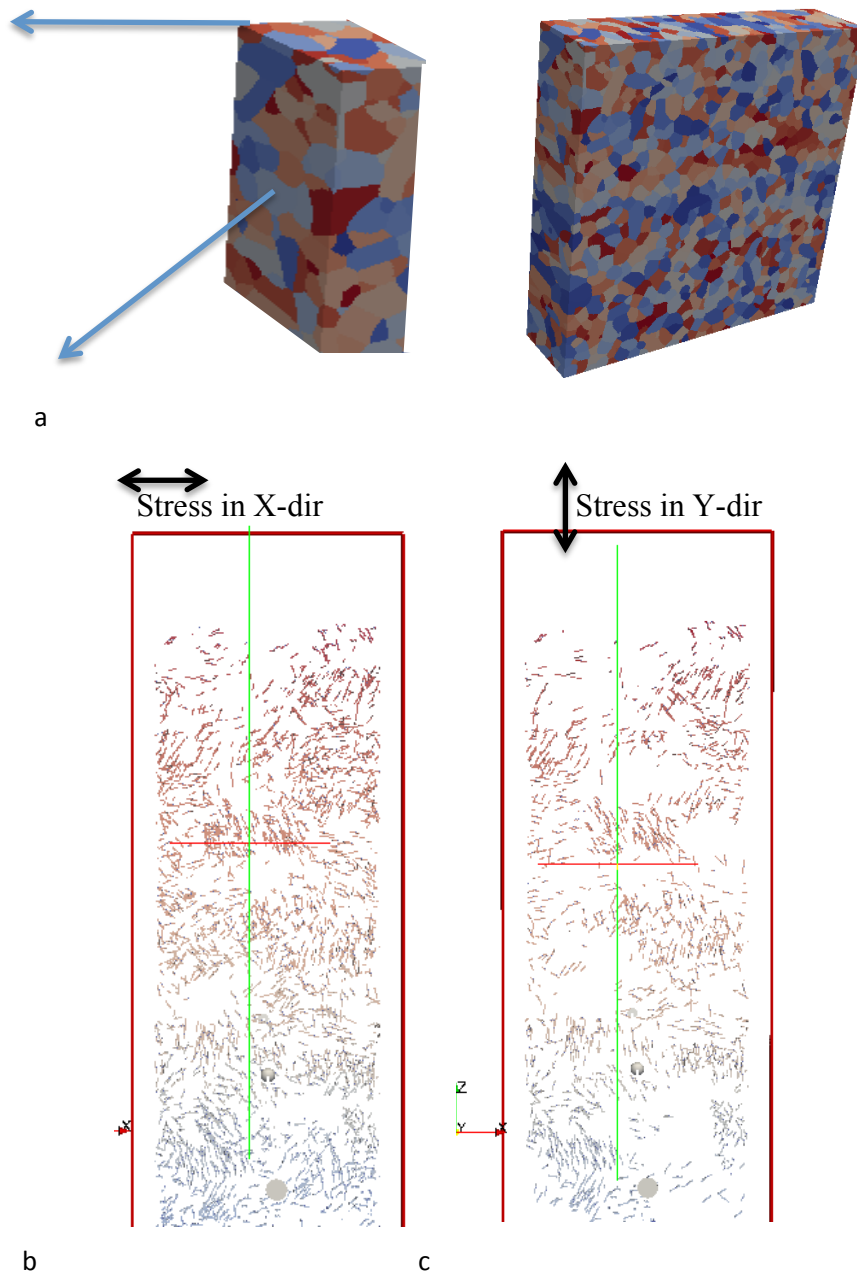


Figure 4.17: Reorientation of precipitates in the volume shown in (a) when stress is applied along the (b) circumferential direction and (c) the radial direction.

Precipitation in Zircaloy-4 with texture, and without and with applied stress in the radial and circumferential directions. Although the same grain structure shown in Figure 4.15 was used, the grains were assigned orientations with a probability distribution given by **Equation 3-1** and plotted in Figure 3.7. Most grains had basal planes oriented parallel to the RD as shown in Figure 4.13. The simulation was performed under identical condition as those described in the section on precipitation in Zircaloy-4 with no texture and no stress. The only difference was this microstructure had texture.

The results after all precipitates have formed are presented in Figure 4.18, precipitates in a small region of the microstructure. These images show little to no reorientation with applied stress. Because the orientation of the individual precipitates is difficult to see in these figures, the data were reduced to numerical data, so that they can be plotted for a clearer interpretation of these data. The angle of the precipitates in all the simulations presented in this section 3.2.1 (precipitation in a Zircaloy-4 microstructure with and without texture and with no applied stress and stress applied in the circumferential and radial directions) are plotted as frequency of occurrence at that angle in Figure 4.19.

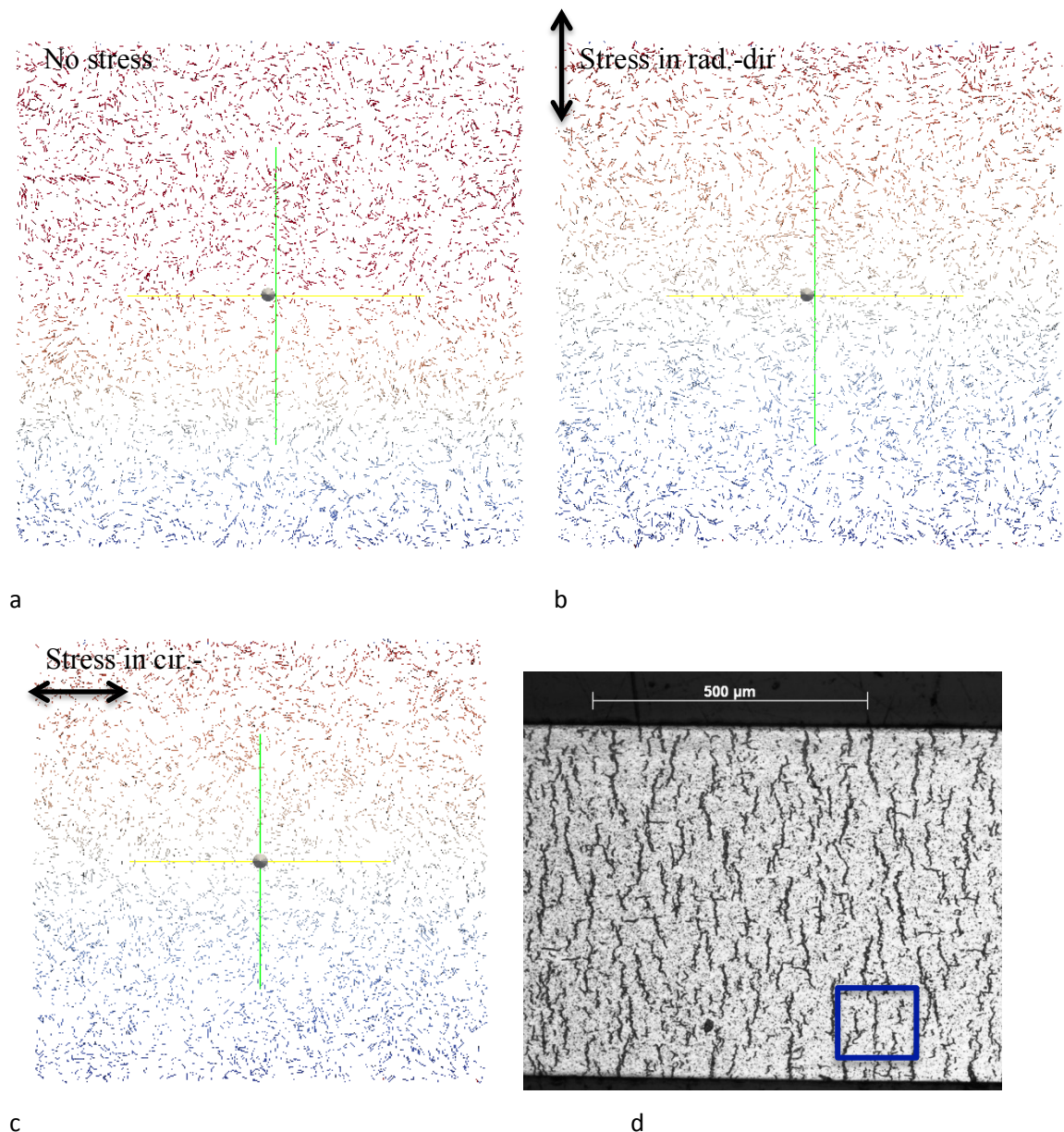


Figure 4.18: Reorientation of precipitates in a thin slice over the entire simulation area with (a) no stress is applied, and with stress applied along the (b) circumferential direction and (c) the radial direction. (d) A micrograph showing the precipitate reorientation under applied stress in the radial direction. The scale of the microstructural images (a) to (c) is shown by the inset blue box.

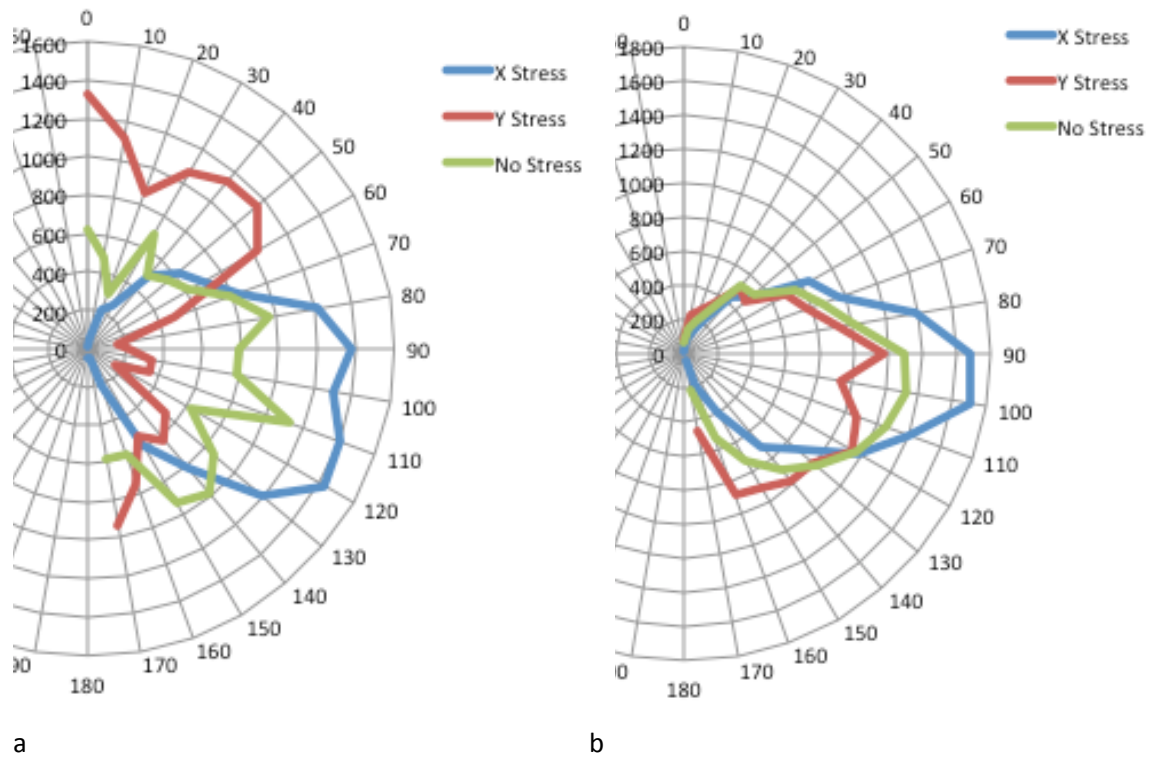


Figure 4.19: Frequency plot of precipitate oriented in that direction for Zircaloy-4 with (a) randomly oriented grains and no texture and (b) with strong texture with the basal plane aligned in the rolling direction.

Figure 4.19 shows that in Zircaloy-4 with no texture in the grain orientation, the orientation of precipitates is nominally uniform in all directions as shown by the green curve in (a). However, when stress is applied in either the circumferential or radial directions, the precipitates reorient themselves so that they are primarily perpendicular to the applied stress as shown by the red and blue curves in (a). Zircaloy-4 with strong crystallographic grain texture, with the basal plane of the HCP α -Zr grains oriented primarily in the RD show very different results. When no stress is applied, the precipitates are primarily aligned in the circumferential direction as shown by the green curve in (b). Under applied radial stress, the orientation of the precipitates remains very similar with most precipitates still oriented in the circumferential direction, but with a slightly increase in the range of angles. Under applied circumferential stress, the precipitate orientation becomes even more closely aligned with the circumferential direction.

These simulation results are not in agreement with the results reported by Colas et al. (Colas et al., 2010) and others studying reorientation of precipitates under different stress conditions as seen Figure 4.14 and Figure 4.18d. The results of precipitation under no applied stress in the Zircaloy-4 with texture were in good agreement with experimentally reported results, but under conditions of applied stress particularly in the radial direction, this did not hold.

4.2.2 Discussion

While some behaviors reported in the literature were successfully simulated by the hybrid Potts-phase field model, the reorientation in textured Zircaloy-4 was not. Since virtually all experimental characterization of δ -ZrH_{1.5} precipitates forming in α -Zr matrix show the precipitates forming in the basal plane with (0001) α -Zr// (111) δ -ZrH_{1.5}, it stands to reason that in a strongly textured cladding, reorientation of the precipitates cannot occur by individual precipitates changing their orientation as they can in non-textured materials. There are simply not sufficient number of α -Zr grains oriented with their basal planes aligned nominally parallel to the radial direction to enable precipitate reorientation as seen in the optical micrographs of Zircaloy-2 and Zircaloy-4.

We propose that the reorientation observed in these claddings can be explained by individual precipitates aligning themselves by stacking in the radial direction rather than by the rotation of individual precipitates along the radial direction. This behavior is shown schematically in Figure 4.20.

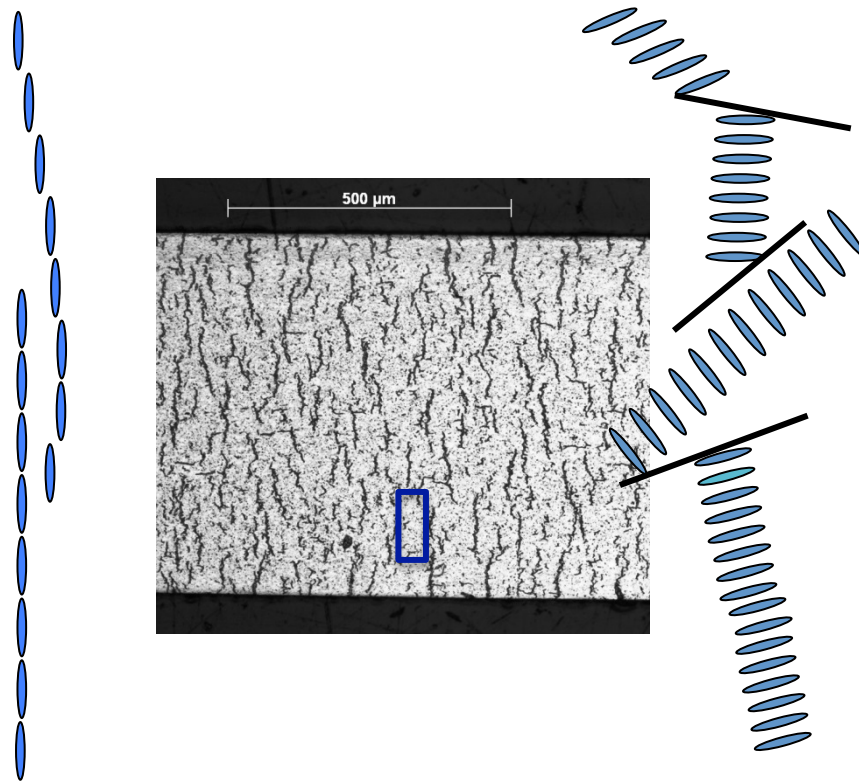


Figure 4.20: A feature such as that shown in the blue box on the optical micrograph was thought to be formed by precipitates rotating and aligning themselves as shown to the left in dark blue. Our simulations, however, are suggesting that this is not possible and stacking of the precipitates as shown to the right in lighter blue is probably the explanation for this behavior.

4.3 Summary and Conclusions

We applied the hydride precipitate formation model to two cases that were studied experimentally to validate the model. In the first case of hydrogen charging of Zircaloy-2, Zircaloy-4 and Zirlo™ by aqueous charging, many of the experimentally observed

behavior of H diffusion into the α -Zr matrix were reproduced in good agreement with the experiments. However, one of the behaviors observed in all three materials was that the δ -ZrH_{1.5} layer thickness d varied widely from grain to grain, while the average thickness maintained the relationship $d \sim t^2$ expected for diffusion-controlled layer growth. Application of the model with only one set of conditions reproduced this variation in hydride layer thickness. High anisotropy in the diffusion coefficient in the hydride phase with crystallographic direction reproduced these experimental results, with the variation in layer thickness from grain to grain, but with layer thickness growth exponent of 2. Not only was the model validated in this case, but it was used to provide understanding and insight into the physical behavior of diffusion and precipitation under surface charging conditions at low-temperatures. The model showed that high anisotropy in the diffusion coefficient in the hydride phase was necessary. Furthermore, even under conditions of high diffusion anisotropy leading to highly variable hydride layer thickness, the kinetics of diffusion-controlled with exponent of 2 still remained as seen in the experiments.

The second case, hydride reorientation under tensile hoop stress in Zircaloy-4, the model could not reproduce the large string-like features observed by optically microscopy in experiments. A condition of precipitate growth in the model is that the precipitate can only grow in the basal plane of the HCP α -Zr matrix. This condition is well justified as it has been repeatedly reported by many experimentalists as already reviewed earlier. In Zircaloy-4, a highly textured material with the basal-plane predominantly oriented in the rolling direction, the individual hydride precipitates can only be aligned in the basal plane, predominantly in the rolling direction, which is also the circumferential direction. Therefore, it is impossible to form the long string-like features by reorientation of individual precipitates. The model was able to provide this insight leading to much better understanding of how precipitates may align and stack to form features observed at relative low magnifications under optical microscopy. While the model was not validated in this second case, the model results have led to better understanding of precipitates formation. This will be explored and discussed in much great detail in the next chapter with the next steps for model development and continued discovery of the precipitation mechanisms.

4.4 References

- Aziz, M. J. (1997). Thermodynamics of diffusion under pressure and stress: Relation to point defect mechanisms, *Appl. Phys. Lett.* **70**: 2810–2812.
- Birk, S., H. Hanson, S. Marschman, B. Sindelar, K. Sorenson, and J. Wagner (2012). *Used Nuclear Fuel Storage and Transportation Research, Development and Demonstration Plan*, FCRD-FCT-2012-000053.
- Bradbrook, J.S., G.W. Lorimer, and N. Ridley (1972). The Precipitation of Zirconium Hydride in Zirconium and Zircaloy-2, *J. Nucl. Mater.* **42**: 142-160.
- Choi, Y., J.W. Lee, Y.W. Lee, and S.I. Hong (1998). Hydride formation by high temperature cathodic hydrogen charging method and its effect on the corrosion behavior of Zircaloy-4 tubes in acid solution, *J. Nucl. Mater.* **256**: 124-130.

- Clark, B.G., S. Rajasekhara, D. Enos, R. Dingreville, B.L. Doyle, K. Hattar, and R. Weiner (2013). *Nanoscale Mechanisms in Advanced Aging of Materials During Storage of Spent "High Burnup" Nuclear Fuel*, Sandia Report, SAND2013-8084, Sept 2013.
- Colas, K.B., A.T. Motta, J.D. Almer, M.R. Daymond, M. Kerr, A.D. Banchik, P. Vizcaino, and J.R. Santisteban (2010). In situ study of hydride precipitation kinetics and re-orientation, *Acta Mater.* **58**: 6575-6583.
- De Menibus, A. H., Q. Auzoux, O. Dieye, P Berger, S. Bosonnet, E. Foy, V. Macdonald, J. Besson, and J. Crepin (2014). Formation and Characterization of Hydride Blisters in Zircaloy-4 Cladding Tubes, *J. Nucl. Mater.* **449**: 132-147.
- Doyle, B. L., and D. K. Brice (1988). The analysis of elastic recoil detection data, *Nucl. Instr. Meth. Phys. Res. B* **35**: 301-308.
- Ells, C. E. (1968). Hydride Precipitates in Zirconium Alloys (A review), *J. Nucl. Mater.* **28**: 129-151.
- Glazoff, M.V. (2013). Modeling of Some Physical Properties of Zirconium Alloys for Nuclear Applications in Support of UFD Campaign, IN/EXT-13-29581.
- Grosse, M., M. van den Berg, C. Goulet, and A. Kaestner (2012). In-situ investigation of hydrogen diffusion in Zircaloy-4 by means of neutron radiography, *J. Phys: Conf. Series* **340**: 012106.
- Gulbransen, E. A., and K.F. Andrew (1954). Diffusion of hydrogen and deuterium in high purity zirconium, *J. Electrochem. Soc.* **101**: 560-566.
- Hanson, B., H. Alsaed, C. Stockman, D. Enos, R. Meyer, and K. Sorenson (2011). *Gap Analysis to Support Extended Storage of Used Nuclear Fuel*, FCRD-USED-2011 000136, PNNL-20509.
- Harkness, S. D., and W. A. Young (1973). *The diffusion coefficient of hydrogen in delta-phase zirconium hydride*, Atomics International, AEC Research and Development Report NAA-SR-10516.
- Hindle, E.D., and G.F. Slattery (1966). Influence of processing variables on grain structure and hydride orientation in zircaloy-2 tubing, *J. Inst. Met.* **94**: 245-249.
- Hu, X., Terrani, K., Wirth, B. D. (2014). Hydrogen desorption kinetics from zirconium hydride and zirconium metal in vacuum, *J. Nucl. Mater.* **448**: 87-95.
- Iyer, R., and H.W. Pickering (1990). Mechanism and kinetics of electrochemical hydrogen entry and degradation of metallic systems, *Ann. Rev. Mater. Sci.* **20**: 299-338.
- Jackson, M.A. (2013). Digital Representation Environment for Analyzing Microstructure in 3D, <http://dream3d.bluequartz.net/>
- Kammenzind, B. F., B. M. Berquist, R. Bajaj, P. H. Kreyns, D. G. Franklin (1998). The long range migration of hydrogen through Zircaloy in response to tensile and compressive stress gradients, in: G. Sabol, G. Moan (Eds.), 12th international Symposium on Zirconium in the Nuclear Industry, ASTM STP 1354, Toronto, Canada, 1998, pp. 196-233.

- Kearns, J.J. (1972). Diffusion-coefficient of hydrogen in alpha zirconium, zircaloy-2 and zircaloy-4, *J. Nucl. Mater.* **43**: 330-338.
- Khatamian, D., and F.D. Manchester (1989). An ion-beam study of hydrogen diffusion in oxides of Zr and Zr-Nb (2.5 wt-percentage) .1. Diffusion parameters for dense oxide, *J. Nucl. Mater.* **166**: 300-306.
- Kiran Kumar, N.A.P., J.A. Szpunar, and Z. He (2010). Preferential Precipitation of Hydrides in Textured Zircaloy-4 Sheets, *J. Nucl. Mater.* **403**: 101-107.
- Liu, Y.Z., Q. Peng, W.J. Zhao, and H.M. Jiang (2008). Hydride Precipitation by Cathodic Hydrogen Charging Method in Zirconium Alloys, *Mater. Chem. & Phys.* **110**: 56-60.
- Louthan, M.R., and R.P. Marshall (1963). Control of Hydride Orientation in Zircaloy, *J. Nucl. Mater.* **9**: 170-184.
- Majer, G., W. Renz, and R. G. Barnes (1994). The mechanism of hydrogen diffusion in zirconium dihydrides, *J. Phys.: Condens. Matter.* **6**: 2935-2942.
- Mallett, M.W., and W.M. Albrecht (1957). Low-pressure solubility and diffusion of hydrogen in zirconium, *J. Electrochem. Soc.* **104**: 142-146.
- Mazzolai, F.M., and J. Ryll-Nardzewski (1976). Anelastic study of diffusion-coefficient of hydrogen in alpha-zirconium, *J. Less-Common Met.* **49**: 323-327.
- Min, S. J., J. J. Won, K. T. Kim (2014). Terminal cool-down temperature-dependent hydride reorientations in Zr-Nb Alloy claddings under dry storage conditions, *J. Nucl. Mater.* **448**: 172-183.
- Northwood, D., and U. Kosasih (1983). Hydrides and delayed hydrogen cracking in zirconium and its alloys, *Int. Metals Rev.* **28**: 92-121.
- Puls, M.P. (2012). *The Effect of Hydrogen and Hydrides on the Integrity of Zirconium Alloy Compounds Delayed Hydride Cracking*. Springer.
- Rajasekhara, S., P.G. Kotula, D.G. Enos, B.L. Doyle, K. Hattar, B.G. Clark). Influence of Zr-Alloy Composition on Hydride formation during initial period of hydrogen charging, in preparation.
- Santisteban, J. R., A. Steuwer, G. Domizzi, and M. Peel (2009). Determination of residual stresses around blisters in Zr-2.5%Nb pressure tubes, *Powder Diffraction* **24**: S72-S76.
- Sawatzky, A. (1960). The diffusion and solubility of hydrogen in the alpha-phase of zircaloy-2, *J. Nucl. Mater.* **2**: 62-68.
- Terrani, K. A., J. E. Seifried, and D. R. Olander (2009). Transient hydride fuel behavior in LWRs, *J. Nucl. Mater.* **392**: 192-199.
- Terrani, K. A., M. Balooch, D. Wongsawaeng, S. Jaiyen, and D. R. Olander (2010). The kinetics of hydrogen desorption from and adsorption on zirconium hydride, *J. Nucl. Mater.* **397**: 61-68.
- Tesmer, J.R., M. Nastasi, J.C. Barbour, C.J. Maggiore, and J.W. Mayer (eds.) (1995). In *Handbook of modern ion beam analysis*, Materials Research Society, 83-138.

Vostryakov, A.A., E.A. Pastukhov, N.I. Sidorov, and V.P. Chentsov (2012). High-Temperature Diffusion of Hydrogen in Zirconium, Niobium, and Tantalum, *Russian Metallurgy (Metally)*, 672–675.

Whitlow, H.J., Y. Zhang, Y. Wang, T. Winzell, N. Simic, E. Ahlberg, M. Limback, and G. Wikmark (2000). Studies of electrochemical oxidation of Zircaloy nuclear reactor fuel cladding using time-of-flight-energy elastic recoil detection analysis, *Nucl. Instr. Meth. Phys. Res. B* **161**: 584-589.

5. DEVELOPMENT OF HYBRID POTTS-PHASE FIELD MODEL FOR SIMULATION OF ZIRCONIUM HYDRIDE PRECIPITATE FORMATION AND ZIRCALOY-4 CLADDINGS: FUTURE DEVELOPMENT TO INCORPORATE MORPHOLOGY OF PRECIPITATES

As seen in previous chapters, the hybrid model has been useful for simulating many aspects of δ -ZrH_{1.5} formation in zirconium claddings. However, it has failed to predict the gross reorientation behavior observed in Zircaloy-2, Zircaloy-4, ZirloTM and M5. This is primarily because the morphology of precipitates has not been well characterized, particularly in samples that have been subject to tensile hoop stresses. In this chapter, a methodology is presented to incorporate the morphological feature of the hydride precipitates into the hybrid model. While, the hybrid model will be used to obtain morphologies, a new strategy for modeling the hydride precipitation in Zr-based claddings will be proposed and explained. The new strategy will consist of a model with two separate components.

1. A rate-theory model performed on a microstructure, such as the one shown in Figure 4.15 that will predict precipitation and reorientation given local conditions such as temperature, composition, microstructural features such as grain boundaries and other characteristics such as radiation defect densities. This model will solve evolution equations not by direct numerical simulation of all the kinetic processes that are active, but rather as the rate of known kinetic processes given the local conditions in such a microstructure.
2. The hybrid model will be coupled to a mechanical model that calculates local stress fields around precipitates for predicting morphology of precipitates at a much smaller scale such as that shown in Figure 3.22 by direct numerical simulation. The morphological characteristics found from this second part will be incorporated in the rate-theory model for simulation of groupings of precipitates.

The relevant materials physics and its incorporation into such a two-part model are discussed next.

5.1 Precipitate Morphology

Fundamental morphological characterization of the hydride precipitate at the microstructural scale is lacking. This is primarily because microstructural characterization at the grain size-scale has proven to be challenging by standard SEM techniques. Large strains associated with the pilgering process used to fabricate claddings introduces very large amount of strain energy in grains making traditional methods to delineate grain boundaries extremely difficult (Danielson & Sutherlin, 2004). Thus imaging at this scale of grains and precipitates has proven to be difficult. Optical microscopy at the sub-mm scale is robust at imaging precipitates and TEM has yielded much information about individual precipitates, their crystallography and habit planes. However, microstructural characterization at the grain scales showing groups of precipitates and how they organize themselves with respect to each other is virtually non-existent.

Limited evidence exists to show that δ -ZrH_{1.5} precipitates organize themselves to form larger structures that are visible optically as shown schematically in Figure 4.20 and in a TEM micrograph of Zr-2.5% Nb in Figure 3.20 (Bradbrook et al., 1972; Perovic et al., 1983). However, results of the large, mesoscale simulation presented in Section 4.2 suggest that spatial ordering of precipitates is the only way that the characteristic features of radial precipitates can be explained. δ -ZrH_{1.5} precipitates cannot form in non-basal planes of the parent HCP α -Zr grain. The α -Zr grains of all Zr-based claddings are crystallographically textured with strong alignment of the basal plane in the rolling direction (in the circumferential direction). Thus, only a small fraction of grains are aligned with their basal planes in the radial direction. This small fraction of grains that are aligned with their basal planes in the radial direction result in groupings of precipitates in grains that are separated widely and cannot form the long reoriented precipitate features seen in optical micrographs. This suggests that individual precipitates that are radially reoriented cannot result in large reoriented precipitate structures as seen in Figure 3.17, Figure 4.14, and Figure 4.18. Therefore, the precipitates must organize or stack to give the long, radially oriented precipitate features seen in these figures.

For precipitates to arrange themselves in this fashion, there must be a thermodynamic driving force that promotes such an organization. It is suggested that this thermodynamic driving force is the strain energy associated with the volumetric dilatation that accompanies precipitation of δ -ZrH_{1.5} in α -Zr. As described in Section 3.3, there is a large volumetric dilatation of 17% associated with this phase transformation. The strain tensor for the transformation is

$$\varepsilon = \begin{bmatrix} 0.048 & 0 & 0 \\ 0 & 0.048 & 0 \\ 0 & 0 & 0.072 \end{bmatrix}$$

with the largest strain of $\varepsilon_{33} = 0.072$ occurring in the direction of the basal pole of the HCP α -Zr phase. The magnitudes of the strain components suggest that precipitates form circular platelets in the shape of a disc with the short axis of the disc aligning with the basal pole. However, TEM results in the literature suggest that the precipitates may be needle-shaped and recent high-resolution SEM images obtained by Shimskey and Lavender (Shimskey and Lavender, 2014) suggest the same. While, the TEM images show elongated needle-like precipitates all the precipitate morphological works discussed in section 3.2.2 describe the precipitates as platelets, so precipitates are discussed and analyzed with both geometries.

Perovic and co-workers have suggested ordered precipitates in α -Zr and in other metals (Perovic et al., 1981) form by elastic stress-influenced nucleation, termed autocatalytic nucleation, and elastic stabilization. They argue the first precipitates nucleated heterogeneously on radiation or other defects, and once the stress field formed around the precipitates (Perovic et al., 1982), the locations of subsequent nucleation were determined by the elastic stress field forming around them (Perovic et al., 1992; Perovic & Weatherly, 1984). However, they did not characterize the morphology of hydrides at the microstructural scale that were reoriented by stress applied perpendicular to the radial direction. While ordering of the precipitates is seen, the stacking of precipitates as shown schematically in Figure 4.20 is not known to be definitively shown.

It is proposed in this work that the ordering of precipitates into stacks as shown in Figure 4.20 is what appears to give the gross reorientation of hydride precipitation observed by optical microscopy and not reorientation of individual precipitates. The elastic stresses surrounding $\delta\text{-ZrH}_{1.5}$ precipitates will be analytically investigated to determine if there is a thermodynamic driving force for such stacking to occur. This will be done by using the Eshelby method to calculate the stress field around inclusions.

Eshelby analysis of $\delta\text{-ZrH}_{1.5}$ precipitates: Eshelby (Eshelby, 1957) used analytical techniques to calculate the stress field produced by a phase transformation in a small region (inclusion) embedded within an infinite elastic medium. He imagined an inclusion that is removed from its matrix. The inclusion undergoes a uniform strain due to the inelastic phase transformation process. A stress is applied to the surfaces of the inclusion so that it elastically deforms to its original dimensions. The inclusion is inserted back into the matrix with a strong bond between them at the interface and the stress applied to the inclusion surface is removed. Under these conditions, assuming that both the inclusion and matrix deform elastically only, they will both experience elastic stress. This stress field is the Eshelby solution and is ideally suited to calculate the stress field of a $\delta\text{-ZrH}_{1.5}$ precipitate forming with uniform strain in an $\alpha\text{-Zr}$ matrix. It has been used to evaluate the stress field of a single $\delta\text{-ZrH}_{1.5}$ precipitate in an infinite $\alpha\text{-Zr}$ matrix with the correct crystallographic orientation of the precipitate with the known strain misfit.

This section describes the simplest case for modeling/estimating the stored elastic energy at the surface of a single $\delta\text{-ZrH}_{1.5}$ precipitate. The precipitate is assumed to have formed within an infinite matrix medium of zirconium. The result of precipitate formation is modeled as an inelastic transformation over the domain defined by the precipitate shape and extent. If the precipitate formation is not embedded within the infinite matrix, the precipitate size and shape would change due to the inelastic transformation. However, due to the surrounding matrix, an elastic field is induced inside and outside the inclusion. Using the Eshelby approach, this induced elastic field can be computed and subsequently used to evaluate stored elastic energy due to precipitate formation.

The precipitate is assumed to be in the shape of an ellipsoid which is parameterized by three length dimensions (a, b, c) along the coordinate axes x, y, z . It is also assumed that both the matrix and inclusion have the same isotropic elastic moduli. Values used for demonstration calculations are given in Table 5.1.

Table 5.1 Isotropic inclusions: shape parameters and material moduli. The ellipsoidal parameters given here describe a long/needle-like precipitate.

Property	Value	Units
Young's modulus: E	93×10^{-3}	<i>Tera Pa</i>
Poisson's ratio: ν	0.28	<i>dimensionless</i>
Major axis: a	0.5	μm
Minor axis: b	0.05	μm
Minor axis: c	0.05	μm

This calculation is described as the 'transformation' problem by Eshelby. Using the assumptions above, the following steps are used to calculate the stored elastic energy in the matrix. The calculation described below provides the energy density in the matrix at

the surface interface between the inclusion (region where the so-called eigenstrains $\{e^T\}$ are given) and the matrix.

1. For a given inclusion shape, components of the 4th order Eshelby tensor S_{ilmn} are assumed to be known. The Eshelby tensor \mathbf{S} can also be represented by a 6×6 matrix $[S]$ – details on calculation of $[S]$ for particular shapes are described later in **Equation 5-5**. A relationship between components of the stress-free strains e_{mn}^t and components of the constrained strains e_{mn}^c is given by the Eshelby tensor which maps second order tensors into second order tensors. This relationship can also be expressed in Voight matrix form where the transformation strain and constrained strain are denoted as 6 component vectors using brackets $\{\cdot\}$.

$$e_{il}^c = S_{ilmn} e_{mn}^t \text{ tensor notation, } \{e^c\} = [S]\{e^t\} \text{ Voight/matrix notation} \quad \text{Eq. 5-1}$$

2. Using the above formula, the constrained strain tensor \mathbf{e}^c is evaluated; subsequently, the strain in the matrix on the surface of the inclusion can be computed. The scalar $e^c = \text{Tr } \mathbf{e}^c$ and deviatoric parts $'\mathbf{e}^c$ are computed separately and recombined as necessary to form the full tensor.

$$e^c(out) = e^c(in) - \frac{1+\nu}{3} \frac{1-\nu}{1-\nu} e^t - \frac{1-2\nu}{1-\nu} \hat{n} \cdot '\mathbf{e}^t \hat{n} \quad \text{Eq. 5-2}$$

$$\begin{aligned} '\mathbf{e}^c(out) = '\mathbf{e}^c(in) &+ \frac{1}{1-\nu} (\hat{n} \cdot '\mathbf{e}^t \hat{n}) \hat{n} \otimes \hat{n} - '\mathbf{e}^t \hat{n} \otimes \hat{n} - \hat{n} \otimes '\mathbf{e}^t \hat{n} - \frac{1-2\nu}{1-\nu} \hat{n} \cdot '\mathbf{e}^t \hat{n} + \\ &\frac{1}{3} \frac{1-2\nu}{1-\nu} (\hat{n} \cdot '\mathbf{e}^t \hat{n}) \mathbf{I} - \frac{1}{3} \frac{1+\nu}{1-\nu} e^t \left(\hat{n} \otimes \hat{n} - \frac{1}{3} \mathbf{I} \right) \end{aligned} \quad \text{Eq. 5-3}$$

where boldface denotes tensors, $'\mathbf{e}^c$ denotes the deviatoric tensor associated with \mathbf{e}^c , $'\mathbf{e}^t$ denotes the deviatoric tensor associated with the eigenstrain \mathbf{e}^t , $e^c = \text{Tr } \mathbf{e}^c = \mathbf{I} : \mathbf{e}^c$ denotes the scalar part of the eigenstrain tensor \mathbf{e}^t , \mathbf{I} denotes the second order identity tensor, ν denotes Poisson's ratio, and \hat{n} denotes the unit normal to the inclusion surface. This formula (Eshelby, 1957) was derived using potential theory and provides a jump (difference) in strain when moving across the interface. Since the strain on one side of the interface is known $\mathbf{e}^c(in)$ the only unknown is the strain in the matrix $\mathbf{e}^c(out)$.

1. Using $\mathbf{e}^c(out)$ calculated above, the stored elastic energy J in the matrix is evaluated:

$$J = \frac{1}{2} (\kappa (e^c)^2 + 2\mu '\mathbf{e}^c : '\mathbf{e}^c) \quad \text{Eq. 5-4}$$

where κ denotes the bulk modulus, and μ denotes the shear modulus.

Formulas for calculating the Eshelby tensor of an ellipsoidal inclusion are briefly described. When the inclusion and matrix have the same isotropic moduli, most components in the Eshelby tensor are zero. It is convenient to represent the Eshelby tensor in the form of a 6×6 matrix and use Voight representations for strain tensors.

$$[S] = \begin{bmatrix} S_{1111} & S_{1122} & S_{1133} & 0 & 0 & 0 \\ S_{2211} & S_{2222} & S_{2233} & 0 & 0 & 0 \\ S_{3311} & S_{3322} & S_{3333} & 0 & 0 & 0 \\ 0 & 0 & 0 & S_{1212} & 0 & 0 \\ 0 & 0 & 0 & 0 & S_{1313} & 0 \\ 0 & 0 & 0 & 0 & 0 & S_{2323} \end{bmatrix} \quad \text{Eq. 5-5}$$

The above matrix shows that eigenstrain components (xx, yy, zz) map to the same in \mathbf{e}^c but do not couple to shear components in \mathbf{e}^c . Note that components of shear in the eigenstrain do not couple with components (xx,yy,zz), i.e. $S[1:3,3:6] = 0$ and $S[3:6,1:3] = 0$; also note that components of shear do not couple with one another, i.e. $S = [3,4 = 0]$ for example. When the eigenstrain only consists of components (xx,yy,zz) then there will be no shear in \mathbf{e}^c . The above matrix **Equation 5-5** maps a Voight representation $\{e^t\} = \{e_{xx}^t, e_{yy}^t, e_{zz}^t, 2e_{xy}^t, 2e_{xz}^t, 2e_{yz}^t\}$ of the eigenstrain tensor components into a Voight representation of the constrained strain tensor \mathbf{e}^c .

For an ellipsoidal inclusion where $b = c < a$, the following formulas can be used to compute the non-zero entries in the above Eshelby matrix in **Equation 5-5**.

$$\begin{aligned}
 S_{1111} &= Qa^2I_{aa} + RI_a, & S_{1122} &= Qb^2I_{ab} - RI_a, & S_{1133} &= Qc^2I_{ac} - RI_a \\
 S_{2211} &= Qa^2I_{ab} - RI_b, & S_{2222} &= Qb^2I_{bb} + RI_b, & S_{2233} &= Qc^2I_{bc} - RI_b \\
 S_{3311} &= Qa^2I_{ac} - RI_c, & S_{3322} &= Qb^2I_{bc} - RI_c, & S_{3333} &= Qc^2I_{cc} + RI_c \\
 S_{1212} &= \frac{1}{2}Q(a^2 + b^2)I_{ab} + \frac{1}{2}R(I_a + I_b) \\
 S_{1313} &= \frac{1}{2}Q(a^2 + c^2)I_{ac} + \frac{1}{2}R(I_a + I_c) \\
 S_{2323} &= \frac{1}{2}Q(b^2 + c^2)I_{bc} + \frac{1}{2}R(I_b + I_c)
 \end{aligned} \tag{Eq. 5-6}$$

where the following formulas can be used to evaluate the above matrix entries; note there is an order dependence in these formulas in that some values depend upon previously computed values.

$$\begin{aligned}
 I_b &= \frac{2\pi ac^2}{(a^2 - c^2)^{\frac{3}{2}}} \left\{ \frac{a}{c} \left(\frac{a^2}{c^2} - 1 \right)^{\frac{1}{2}} - \cosh^{-1} \frac{a}{c} \right\} \\
 I_c &= I_b \\
 I_a &= 4\pi - I_b - I_c \\
 I_{ab} &= \frac{1}{3} \frac{I_b - I_a}{a^2 - b^2} \\
 I_{ac} &= \frac{1}{3} \frac{I_c - I_a}{a^2 - c^2} \\
 I_{aa} &= \frac{4}{3} \frac{\pi}{a^2} - I_{ab} - I_{ac} \\
 I_{bc} &= \frac{1}{3} \frac{\pi}{b^2} - \frac{I_{ab}}{4} \\
 I_{bb} &= 3I_{bc} \\
 I_{cc} &= \frac{4}{3} \frac{\pi}{c^2} - I_{ac} - I_{bc} \\
 Q &= \frac{3}{8\pi(1-\nu)} \\
 R &= \frac{1-2\nu}{8\pi(1-\nu)}
 \end{aligned} \tag{Eq. 5-7}$$

Using the Eshelby solution, the stress field in the matrix near the precipitate will be calculated. Next, the stress field will be incorporated into the hybrid equation of state as

$$\mathbf{E}_{hybrid} = \sum_{i=1}^N \left(\mathbf{E}_v(\mathbf{q}_i, \mathbf{C}_i) + \sum_{j=1}^n \mathbf{J}(\mathbf{q}_i, \mathbf{q}_j) + \kappa_c (\nabla \mathbf{C}_i)^2 + \frac{\gamma}{2} \sigma_i^2 \right) \tag{Eq. 5-8}$$

where Y is Young's elastic modulus and σ_i is the Eshelby stress in pixel i . This modification of the hybrid Potts-phase field model will enable the solution of the stacking of smaller individual precipitates.

Role of Radial Stress on Reorientation of δ -ZrH_{1.5} Precipitates: All Zr-based claddings form δ -ZrH_{1.5} precipitates in the circumferential orientation as shown in Figure 3.16 and Figure 4.12 unless there is a substantial tensile hoop stress applied to the cladding. Many have applied tensile hoop stresses (in the direction perpendicular to the radial direction) to hydrogenated Zr-based claddings. Louthan and Marshall (Louthan and Marshall, 1963) reported no reorientation in Zircaloy at tensile hoop stresses less than 100 MPa; above 100 MPa, reorientation increased with increasing stress. Bai et al. (Bai et al., 1994) reported a threshold stress of 95 to 210 MPa for Zircaloy-4 depending on fabrication processes with reorientation saturating at stresses of 170 to 330 MPa. Colas et al. (Colas et al., 2010) reported a threshold stress of approximately 85 MPa for both Zircaloy-4 and Zircaloy-2. While the overall reorientation of the precipitates is characterized by all these researchers using optical microscopy, none have looked carefully at the morphology to determine the arrangement or groupings of the precipitates to see if the individual ones have reoriented or they are stacked and grouped to appear to form reoriented structures at the optical scale. It is this feature of precipitate stacking that will be explored using the Eshelby analysis of the stress state around precipitates.

5.2 Thermodynamics of precipitation

The thermodynamic volumetric free energies of the different phases giving rise to the equilibrium phases in the Zr-H system have been extensively reviewed in Section 3.2.1. We have shown that ThermoCalc can be used to generate free energies that give excellent compositional results using the hybrid model for the precipitates and matrix in Chapters 2 and 3. The factors that will change these free energies are temperature and additional components. Temperature can be easily handled by ThermoCalc and has been demonstrated over temperature range of 300°C to 400°C. Additional components can be handled to a point by ThermoCalc; however, the primary effect of the small amount of additives used in Zr-based claddings will be to change the shapes of the δ -ZrH_{1.5} and α -Zr free energy curve minima and move them higher or lower in energy with respect to each other. While these will change the exact composition of the two phases in equilibrium with each other, it will not change the overall precipitation behavior significantly as reported by many (Erikson et al., 1964; Kearns, 1967; Sawatzky & Wilkins, 1967; Slattery, 1967; Khatamian & Ling, 1997; Khatamian et al., 1995; Pan et al., 1996; Une & Ishimoto, 2003).

The thermodynamic variable that appears to have a much greater influence is the stress field associated with δ -ZrH_{1.5} precipitation. The equation of state used in the hybrid model has an additional term, the elastic strain energy given by the fourth term of **Equation 5-8**. We will modify the hybrid model to include the local, microstructure-based elastic free energy term to treat the autocatalytic nucleation and growth of precipitates. However, neither the Potts nor phase-field models can calculate the stress field as a result of strains. Both are energy models and cannot solve for tensorial quantities such as stress or strain. So, we must couple the hybrid model to mechanics

model. This topic was described in the previous section and will be discussed further in future proposed work section.

While the first term, the volumetric free energy is used to generate the phase stability diagram, it is the total free energy given by **Equation 5-8** that determines the microstructural and compositional evolution. The resulting microstructure and composition are typically not exactly the same as the ones at equilibrium as the interfacial energies and strain energies can cause small deviations locally. For the process of interest in this work, precipitation of δ -ZrH_{1.5} in α -Zr, precipitation occurs at temperatures slightly below those expected from the equilibrium phase diagram when cooling from a higher temperature. While the chemical free energy would predict a given precipitation temperature, the precipitates must overcome the increase in interfacial and elastic strain energies associated with nucleating and growing a precipitate; thus, many have measured lower precipitation temperatures than predicted by the Zr-H equilibrium phase diagram. Une and Ishimoto (Une & Ishimoto, 2003) measured the terminal solid solubility during dissolution, TSSD, of hydrides using differential scanning calorimetry and reported under cooling of approximately 25 to 40°C in the 300 to 400°C range for precipitation. Colas et al. (Colas et al., 2010) measured the TSSD in Zircaloy-2 and Zircaloy-4 using neutron diffraction and reported very similar results as Une and Ishimoto with under coolings of 25 to 30°C and very little sensitivity to cooling rate. Une and Ishimoto also compiled the TSSD published by several research groups on zirconium, Zircaloy-2, Zircaloy-4 and Zr-2.5% NB at different cooling rates and using different methods. All showed very similar TSSD. Therefore for the purposes of modeling, we assume the concentration of hydrogen in α -Zr is that obtained by Une and Ishimoto (Une & Ishimoto, 2003)

$$C_{TSSD} = 1.2 \times 10^5 \exp\left(\frac{-36540}{RT}\right) \quad \text{Eq. 5-9}$$

where R is the gas constant 8.314 J/K-mol and T is temperature in K.

5.3 Kinetics of precipitate nucleation and growth

The kinetics of precipitation are important for predicting the precipitation and reorientation as this is a non-equilibrium process occurring as the temperature is continuously changing. Thus, how quickly the changes occur as the temperature is changing is important. Before addressing the kinetics of precipitation itself, it is relevant to review the thermal history of drying and cooling during dry storage. The fuel assembly drying temperature, achieved by not applying a vacuum around the assembly for some time less than a day, cannot exceed 400°C per Nuclear Regulatory Commission (NRC) regulations (NUREG, 1997). When the fuel assembly is actively cooled again, the outer cladding temperature drops by 50 to 75°C in a period of a few hours to days by Hansen's calculations (Hansen, 2012) as shown in Figure 3.1, and over a much longer period by Rashid's calculations (Rashid & Machiels, 1997). After that the fuel assembly and cladding temperatures decrease very slowly at rates of a 1 to 3°C/yr. Hydride precipitation is a diffusional phase transformation with precipitates nucleating and growing. Even at early times, when the temperature drops rapidly in comparison, the rate of temperature change is the less than 4°C/hr.

At these slow cooling rates, the microstructural and compositional evolution accompanying δ -ZrH_{1.5} precipitation is virtually unaffected by the temperature change.

The slow cooling rate ensures that the microstructure is continually reaching equilibrium in a quasi-static fashion. The rate-controlling parameters for growth of a nucleated precipitate can be either diffusion of hydrogen from the matrix to the growing surface or the kinetics of precipitate growth at the precipitate/matrix interface. The former is assumed to be the mechanism as experiments on surface hydride formation suggest it is diffusion controlled (Clark et al., 2013). While the kinetics may not change the morphology, it will influence how quickly the hydrides form and possibly the time to clad failure. Diffusion coefficients for H and Zr have been measured for the temperature range of interest here (Mallett & Albrecht, 1957; Hood, 1988). Interestingly, no measurable difference in diffusion of H in zirconium, Zircaloy-2 and Zircaloy-4 were found and furthermore, the grain size and shape were also determined not to be factors (Kearns, 1972). Texture, however, may be important, as Kearns has reported that the diffusivity is a function of crystallographic orientation in α -Zr. There is a temperature gradient in the claddings during cooling and a heat transport estimate also has been determined (Sawatzky, 1960). A more complete discussion of the diffusion coefficients of H diffusing in α -Zr is given in Section 4.1.1 and Figure 4.9. Here only the implications of these diffusion results will be discussed.

At the temperatures of interest, the diffusion coefficient of hydrogen in α -Zr ranges from 5×10^{-6} to 2×10^{-5} cm²/sec between 300 and 400 °C. At these diffusivities, hydrogen will diffuse 100 μ m at 400 °C in 5 sec. and at 300 °C in 20 sec. At these very fast diffusion rates, precipitate growth, which requires diffusion on the order of a grain length (10 μ m, requiring 2 sec at 300°C and 0.05 seconds at 400°C) will be, for all practical purposes, instantaneous with time as precipitate growth will be very fast in comparison to rate of cooling even during the initial period when temperature is dropping quickly. Although Kearns reported anisotropy in the diffusion of hydrogen in Zircaloy-2 and Zircaloy-4, the difference was only by a factor of 2. This only decreases the diffusion time by 2 \times , which is still too fast to be of concern in claddings that are cooling very slowly.

Next, we consider nucleation rate. While the nucleation rate by itself has not been characterized, several (Root & Fong, 1996; Ells, 1968; Une & Ishimoto, 2003; Colas et al., 2010) have experimentally characterized the total δ -ZrH_{1.5} to α -Zr phase transformation time. Root and Fong (Root & Fong, 1996) characterized the precipitation and dissolution of precipitates using neutron diffraction studies in Zr-2.5% Nb. They used cooling rates of 0.1 to 2.5°C/min; although these cooling rates are very slow, they are much faster than the cooling rates of fuel claddings during dry storage. They report that the precipitates reach complete equilibrium within an hour or so. Obtaining neutron diffraction patterns requires long times, of at least an hour, so Colas et al. (Colas et al., 2010) used synchrotron-generated X-rays which require much less time to characterize precipitation. They characterized precipitation at cooling rates ranging from 60 to 3°C/min in Zircaloy-2 and Zircaloy-4 and reported reaching equilibrium in 10 to 15 minutes with a small decrease in precipitation temperature at the high cooling rate. Une and Ishimoto (Une & Ishimoto, 2003) used differential scanning calorimetry to study precipitation behavior and reported complete precipitation occurring in 100's of seconds in the temperature range of 200 to 500°C. Such a short precipitation time at cooling rates that are orders of magnitude faster than those observed in claddings during dry storage suggest that nucleation is also very fast in spent fuel cladding materials. Lastly, δ -ZrH_{1.5}

precipitation in α -Zr studied experimentally was performed on unirradiated claddings. However, δ -ZrH_{1.5} precipitation in spent fuel will occur in materials that have a lot of irradiation defects providing nucleation sites with lower energy barriers; thus, increasing the nucleate rate. This point will be discussed further in the section on radiation effects. However, the point to be made here is that, while nucleation of δ -ZrH_{1.5} may be the time limiting step in precipitation as opposed to hydrogen diffusion, the overall time for precipitation to attain equilibrium, with concentrations given by **Equation 5-9**, is only a few minutes. When compared to the dry storage times and slow cooling rate of δ -ZrH_{1.5} precipitation behavior in all claddings, the precipitation may be considered instantaneous.

Kinetic evolution processes, other than precipitation, may occur. Further oxidation of cladding or more hydrogen uptake by the claddings during dry storage does not occur. The temperatures are too low for these to occur. Continued chemical interaction with the fuel pellets is also not significant during dry storage. However, at temperatures of 300 to 350 °C, there will be recovery of radiation defects which can affect the strain response of the cladding, making the cladding more ductile as the defects recover. The radiation-induced dislocations and their characteristics will be reviewed next.

5.4 Radiation-induced dislocation and growth in HCP α -Zr

A complicating factor in the phase stability, thermodynamics and kinetics of claddings is the irradiation damage that they sustain in reactor during service. Despite the ability of Zr and Zr-alloys materials to withstand high temperature and irradiation conditions for extended periods of time, radiation-induced phenomena such as creep, growth, hardening, or amorphization do occurs as irradiation damage is sustained during service in reactor. As explained in Chapter 2, the underlying grain structure and texture does not change due to radiation exposure at the temperatures experienced by claddings during reactor operation or drying, however, many point- and line- defects form and organize at the angstrom- and nano-scales which do change hydride formation and reorientation behavior. These will be reviewed in this section.

Relevant at all irradiation temperatures, irradiation creep is driven by super-saturation of vacancies and interstitials and is responsible for climb of dislocation loops and climb and glide of edge dislocations. Radiation-induced growth (RIG), a volume-conserving distortion of materials, is among the most important mechanisms that can compromise the structural integrity of irradiated Zr-based materials. RIG is driven by growth of irradiation-induced loops in the absence of stress and tends to occur in anisotropic materials where the defect diffusion coefficient varies in different crystallographic planes (Woo and Gosele, 1983). In the HCP α - Zr phase, anisotropic defect diffusion coefficients exist, and interstitials show this tendency to a greater degree, with a high diffusion coefficient in the basal plane and a low diffusion coefficient in the prism plane (Frank, 1988; Pasianot and Monti, 1999; Osetsky et al., 2002). Zr-based materials are characterized by low stacking fault energies and predominantly two-dimensional defects (Choi et al., 2013). The network dislocations in the HCP α -Zr primarily have Burgers vectors of $\mathbf{b}=1/3\langle 11-20 \rangle$ of \mathbf{a} -type or $\mathbf{b}=1/3\langle 11-23 \rangle$ of $\mathbf{c}+\mathbf{a}$ -type and $\mathbf{b}=[0001]$ of \mathbf{c} -type (Griffiths et al., 1996) as shown Figure 5.1. The latter \mathbf{c} -component network dislocations have large Burgers vectors and consist of double half-planes. Irradiation results in the formation of dislocation loops that have a single half-plane and Burgers vectors of:

$b=1/3\langle 11-20 \rangle$ *a*-type, especially at low fluences and temperatures; $b=1/6\langle 20-23 \rangle$ *c*/2 + *p*-type or $b=1/2[0001]$ *c*/2-type, especially at high fluences and temperatures. The latter radiation-induced *c*-component dislocations can also be produced by climb of existing *c*-component network dislocations, primarily on basal planes and result in a “corduroy structure” shown in Figure 5.1. The climb of *a*-type loops occurs by interstitial capture and the climb of *c*-type loops from vacancy capture, which results in an accelerated growth mechanism, known as “breakaway growth.”

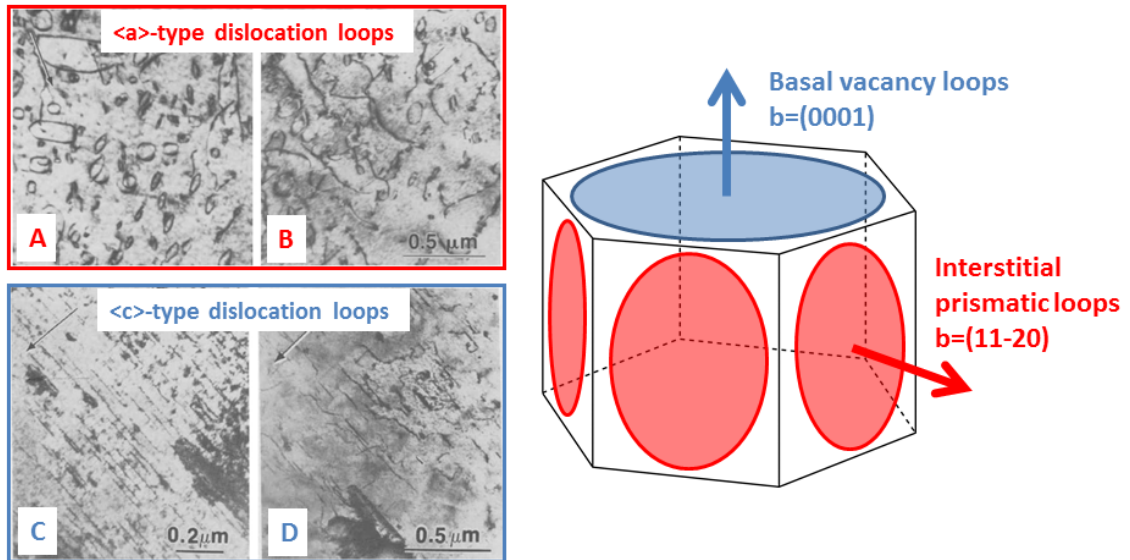


Figure 5.1: Left: (Top) a-type dislocation in an annealed zirconium microstructure at 427°C: (A) $1.1 \times 10^{25} \text{ n/m}^2$; (B) $1.5 \times 10^{25} \text{ n/m}^2$. (Bottom) c-type dislocation in annealed Zircaloy-4 at 287°C: (C) $8.5 \times 10^{25} \text{ n/m}^2$, (D) $7 \times 10^{25} \text{ n/m}^2$ (adapted from Choi et al., 2013). Right: Schematic representation of basal vacancy loops and interstitial prismatic loops formed in the HCP α -phase of pure Zr and Zr alloys.

Based on the extensive experimental work conducted on Zr-based materials, three key parameters have been identified to explain RIG: temperature, fluence, and materials variables (Zee et al., 1987; Carpenter et al., 1988; Rogerson, 1988). As the temperature increases, the density of dislocation loops in Zr and Zircaloy tends to decrease while the loop size increases. Interstitial dislocation loops tend to exhibit a circular shape regardless of the temperature, while vacancy loops usually adopt circular shapes for loop sizes $< 40 \text{ nm}$ and elliptical shapes for larger loop sizes (Choi et al., 2013). According to the seminal work of Northwood and co-workers (Northwood et al., 1974, 1977, 1979) on Zr and Zircalloys, interstitial loops dominate at temperatures below 200 °C and the number of interstitial and vacancy loops is the same around 200 – 250 °C. The proportion of vacancy loops increases to a maximum of about 70% up to 400°C and decreases to 20% at higher temperature. Above 500°C, no radiation damage is observed because radiation-induced defects are annealed by relaxation (Gilbert et al. 1979). The observed mean loop diameter is typically in the range 8-10 nm at 350 °C and 16-23 nm at 400 °C (Choi et al., 2013).

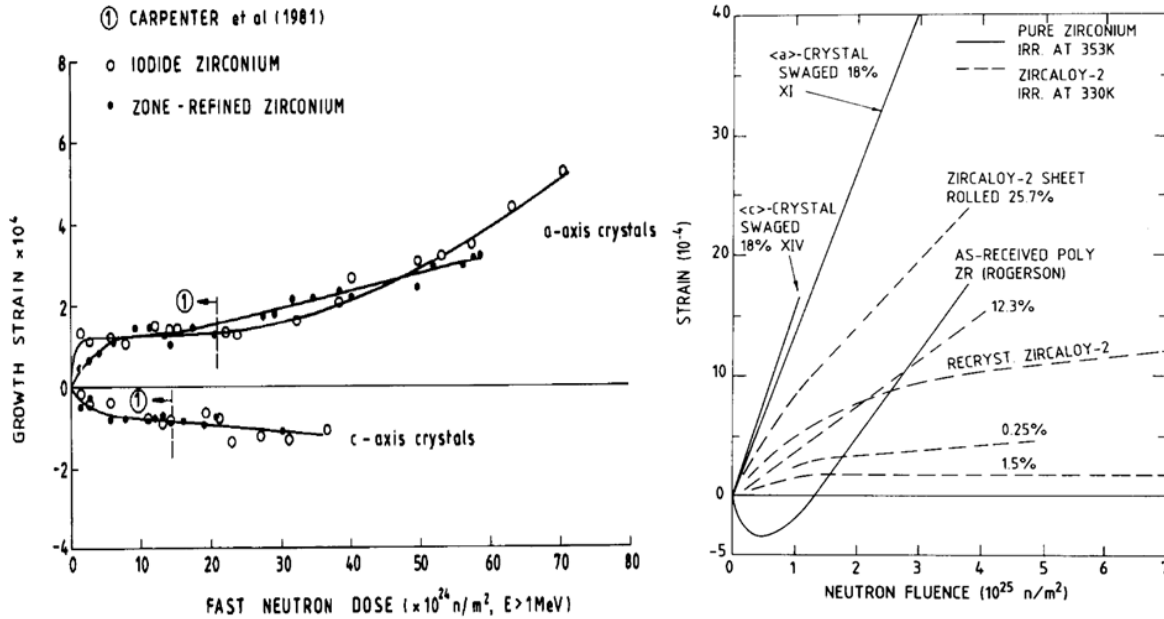


Figure 5.2: Left: Irradiation growth in annealed iodide and zone-refined zirconium single crystals at 280°C (Carpenter et al., 1981; Rogerson, 1988). Right: Comparison of growth behavior of cold-worked zirconium and Zircaloy-2 (Zee et al., 1987).

The effect of neutron fluence on RIG has also been extensively investigated experimentally for a rich variety of Zr and Zr alloys as shown in Figure 5.2. The relative proportions of *a*- and *c*-type dislocation loops within a given temperature range are determined by the irradiation dose, as well as by the presence of other microstructural features (e.g. grain boundaries, network dislocations, etc.). In annealed Zr single crystals, *a*-type dislocation loops density increases rapidly with increasing fluence and start saturating around fluences of $0.1\text{--}2 \times 10^{25}$ n/m². A low stationary growth rate occurs at fluence up to $5\text{--}6 \times 10^{25}$ n/m². After this stationary stage, *c* dislocation loops start to appear and growth breakaway, or accelerated growth, is observed.

Zircaloy-2 and Zircaloy-4 irradiated with fluence up to 8.6×10^{25} n/m² in the temperature range 280 – 322 °C were also investigated to reveal *c*-type dislocation loop characteristics (Holt and Gilbert, 1986). *c*-type loops were observed only with fluence above 3.0×10^{25} n/m², while *a*-type dislocations appeared below this neutron dose. It was also shown that high-density *c* dislocation loops are correlated with the presence of second-phase particles. Indeed, irradiation of Zr alloys results in the redistribution of alloying elements (e.g. Sn, Fe, Ni, and Cr) or impurities from second phases into the primary Zr α -phase. In particular, a clear connection between the creation of *c* dislocation loops and iron sites has been established (De Carlan et al., 1996).

Materials variables in single-crystal or polycrystalline Zr and in annealed or cold-worked Zr alloys also impact RIG. Representative RIG behaviors, as function of the neutron fluence, for annealed Zr single crystals and cold-worked Zr and Zircaloy-2 are shown in Figure 5.2. In single-crystal Zr, RIG is rapid at the beginning and starts from the major sinks, i.e. interstitial dislocations and dislocation loops. At higher fluence, vacancy concentration increases and interstitials tend to disappear in the matrix by recombination with vacancies. Therefore, dislocations and dislocation loops become neutral sinks,

resulting in a slow-growth, stationary stage. During the last growth breakaway stage occurring at highest fluence, c dislocation loops are formed on the basal plane and RIG increases proportionately with radiation dose. In polycrystalline Zr, similar RIG trends are observed, but larger growth strain results due to the favorable effect played by grain boundaries in the growth phenomena. In Zircaloy-2 and Zircaloy-4, RIG is very similar to polycrystalline growth behavior. During the initial transient stage, grain size seems to impact the growth behavior, although this is no longer the case during stationary and breakaway growth. In cold-worked Zircaloys, the dislocation density is high and thus dislocations are major sinks in the Zr matrix, resulting in a nearly linear RIG with the radiation dose. In recrystallized Zircaloys, however, the low dislocation density resulting from annealing causes grain boundaries to become the major sink. As a consequence, the flux of defects to grain boundaries becomes the dominant mechanism to control RIG and growth occurs initially at grain boundaries. At higher fluence, RIG reaches a saturation stage, due to the simultaneous generation of dislocation loops and the absorption of interstitials by grain boundaries. As fluence further increases, more vacancy loops are generated, similarly as in single crystals, and RIG increases linearly with radiation dose.

5.5 Model Adaptation to Incorporate Precipitate Morphology

A model to simulate hydride precipitates in Zircaloy-4 was developed and demonstrated in Chapters 2-4. However, reorientation of the precipitates as observed by optical characterization was not simulated by the microstructure because the autocatalytic nucleation and elastically stabilized growth of the precipitates, which we now believe to occur in Zr-based claddings, is not incorporated into the hybrid model. We will couple the hybrid Potts-phase field model to a micromechanics calculation on the precipitate scale to incorporate the additional and necessary thermodynamic energy contribution resulting from the elastic strain energy associated with the dilatation accompanying δ -ZrH_{1.5} formation. This will be done by using **Equation 5-8** to determine the total free energy of a δ -ZrH_{1.5} precipitate forming in an α -Zr matrix including the elastic strain energy as a function of precipitate size. The stress in each site σ_i around a precipitate of a given size and shape will be calculated using the Eshelby solution as explained in Section 5.1. The total free energy will be minimized using the hybrid methodology by evolving both the microstructure by phase transformation from α -Zr to δ -ZrH_{1.5} and the accompanying compositional field to find the equilibrium configuration of precipitates shape and morphology in simple configurations as explained in previous chapters. These results will be incorporated into a rate-theory model described next.

Whereas the hybrid model is a direct numerical simulation of the entire microstructural and compositional evolution, the rate theory model will be a model that gives a detailed 3D microstructure and composition of individual δ -ZrH_{1.5} precipitates in a polycrystalline, pilgered α -Zr with texture, radiation damage and other relevant features. The underlying microstructure for the rate theory model is identical to the hybrid; the spin at each lattice site will identify that site as belonging to either a δ -ZrH_{1.5} precipitate or to a α -Zr grain of a particular crystallographic orientation. The crystallographic orientation of δ -ZrH_{1.5} precipitate will be determined by its parent α -Zr grain as (0001) α -Zr// (111) δ -ZrH_{1.5}. Associated with each site is a composition corresponding to the concentration of hydrogen in that pixel. The starting microstructure will be identical to

those described in Chapters 3 and 4, the underlying grain structure of the Zr-based claddings with a uniform distribution of dissolved hydrogen that is supersaturated when cooled to the simulation starting temperature, just after drying. The first sites to be nucleated will be attempted by a pre-determined rate function that is based on known nucleation behavior such as dislocation loops serving as nucleation sites with a higher frequency of these loops at grain boundaries or some other physical mechanism. Once a few nuclei have nucleated, the subsequent ones will be nucleated with the results of the hybrid model that incorporates micro-mechanical state of the precipitates and the matrix surrounding it. As these nuclei form, the total hydrogen content in the nuclei and matrix will be adjusted to conserve mass of H and Zr. The rate of the nucleation growth will be considered very fast compared to the cooling rate with precipitates coming to equilibrium with 15 to 30 min as justified in Section 5.3. The continued nucleation and growth of nuclei will stop when the overall concentration of hydrogen in the α -Zr matrix is depleted to the concentration given by **Equation 5-9**. The growth of individual precipitates will stop when the size of the precipitates reaches the elastically stabilized size calculated by the hybrid with micro-mechanics incorporated in it. As the temperature drops during dry storage due to the decay of radioactive materials, the further nucleation and/or growth of precipitates will be determined at temperature increments ranging from 1 to 5 °C. The corresponding hybrid model simulations with micro-mechanical state will be performed at this new lower temperature to obtain the size and shape of the precipitates with the elastic materials constants and other conditions at the new temperature. In this way, the continuous evolution of hydride precipitate formation and reorientation will be simulated.

Rather high tensile hoop stresses ranging from 100 to 200 MPa are required in Zr-based claddings to obtain reorientation. The large simulation results presented in Chapter 3.2.2 show that reorientation of precipitates is not possible in the textured materials when no micro-mechanical stress accompany phase transformation. These results combined with many experimental results suggest that the stress state in and around the individual precipitates and the applied tensile hoop stress are necessary to stack and group precipitates to give the type of reorientation observed by optical techniques in Zr-based claddings. These stress effects of applied hoop stresses and how they influence nucleation and growth of precipitates will be investigated using the hybrid model that incorporates micro-mechanics. This behavior will be incorporated into the rate theory model by modifying the location of nuclei and their growth rates in response to the applied hoop stress of different magnitudes.

5.6 Discovery and Validation Experiments

To support the model, understanding of several key phenomena is critical; foremost of these is the characterization of δ -ZrH_{1.5} precipitates at the grain scale where many tens of precipitates can be imaged. As explained, we suspect that the alignment and spacing of the precipitates is a critical feature of δ -ZrH_{1.5} precipitation and reorientation. Within individual grains, the precipitates are not only expected to orient themselves along the basal plane, but also order themselves in regularly spaced arrangements to form long strings of precipitates. They form in the circumferential direction when there is no stress or a small stress applied; they stack with the long edges on top of each other when there is large hoop stress. Experiments to support this are critical.

The underlying microstructure and texture of Zircalloys, Zirlo™ and M5 claddings is a critical feature of reorientation. Characterizing these would increase the ability to predict δ -ZrH_{1.5} precipitation orientation by enabling the simulation of crystallographic alignment of the precipitates. Furthermore, grain boundaries are the preferred sites for some claddings, thus characterizing the grain structure and size is important for predicting these features.

A substantial tensile hoop stress is a necessary condition for precipitates to reorient themselves. Characterizing the stress on the cladding as a function of burn-up is another parameter that would aid greatly in predicting the reorientation of the δ -ZrH_{1.5} precipitates.

Much of the experimental characterization requested can be obtained from unirradiated samples that are just hydrogenated. While some features of nucleation and growth will be changed by radiation damage, an understanding of the overall morphology of precipitates and how they align themselves would be very helpful to design the model as well as to validate it under matching conditions.

5.7 Summary and Conclusions

A key validation exercise did not yield the reorientation results seen in Zircaloy-4 when large (>100 MPa) tensile hoop stresses are applied. The model is thought to have failed in this one respect because the morphology of the long string-like precipitates that form the reoriented feature is thought to consist of precipitates of the same orientation as the ones that form when no stress is applied, but stacked in a way that the overall precipitates appear to have rotated in response to the tensile hoop stress. This stacking behavior is thought to originate from the dilatation that accompanies precipitate formation, resulting in both precipitate and matrix being under elastic stress. A methodology to determine these elastic stresses is proposed using the Eshelby solution. The hydride precipitation model that is the hybrid Potts-phase field model will be modified to incorporate the elastic strain energy in and around the precipitates in the equation of state. The hybrid model with micro-mechanical thermodynamics will be used to simulate the nucleation and growth of precipitates in a small microstructure consisting of a few grains. The alignment and ordering of the precipitates will be characterized as a function of grain orientation and applied stress.

For predicting hydride formation and reorientation in a large microstructure consisting of hundreds or even thousands of grains, a rate-theory model is proposed. This model will incorporate the results from the hybrid model with micro-mechanics to align groups of precipitates under different conditions. The actual precipitation and growth of the precipitates will be simulated by developing rate equations of all the active processes such as nucleation rates as a function of local composition, temperature and defect structure, growth of the precipitated until they are either elastically stabilized or the hydrogen dissolved in the Zr-matrix is exhausted. The role of thermodynamics, kinetics and radiation damage on precipitation was reviewed and their incorporation in the model was explained.

With the two-part model, i.e. the hybrid model with micro-mechanics and the rate theory model, the entire precipitation behavior in all Zr-based cladding will be simulated and predicted. We have also requested specific experiments to aid in the development and

validation of the model. The most important of these requests is the morphological characterization of the precipitates, which would be used to validate the predictions of the model.

5.8 References

- Bai, J. B., N. Ji, D. Gilbon, C. Prioul, and D. Francois (1994). Hydride Embrittlement in Zircaloy-4 Plate: Part II. Interaction between the Tensile Stress and the Hydride Morphology, *Met. & Mater. Trans. A* **25**: 1199-1208.
- Bradbrook, J. S., G. W. Limer, and N. Ridley (1972). The precipitation of Zirconium hydride in zirconium and Zircaloy-2", *J. Nucl. Mater.* **42**: 142-160.
- Carpenter, G. J. C., R. A. Murgatroyd, A. Rogerson, and J. F. Watters (1981). Irradiation growth of zirconium single crystals, *J. Nucl. Mater.* **101**: 28-37.
- Carpenter, G. J. C., R. H. Zee, and A. Rogerson (1988). Irradiation growth of zirconium single crystals: A review, *J. Nucl. Mater.* **159**: 86-100.
- Choi, S. I., and J. H. Kim (2013). Radiation-induced dislocation and growth behavior of zirconium and zirconium alloys - A review. *Nucl. Eng. & Techno.* **45**: 385-392.
- Clark, B.G., S. Rajasekhara, D. Enos, R. Dingreville, B.L. Doyle, K. Hattar, and R. Weiner (2013). *Nanoscale Mechanisms in Advanced Aging of Materials During Storage of Spent "High Burnup" Nuclear Fuel*, Sandia Report, SAND2013-8084, Sept 2013.
- Colas, K.B., A.T. Motta, J.D. Almer, M.R. Daymond, M. Kerr, A.D. Banchik, P. Vizcaino, and J.R. Santisteban (2010). In situ study of hydride precipitation kinetics and re-orientation, *Acta Mater.* **58**: 6575-6583.
- Cox, J. J., E. R. Homer, and V. Tikare (2013). Coupled microstructural-compositional evolution informed by a thermodynamic database using the hybrid Potts-phase field model, *MRS Proceedings*, 1524.
- Danielson, P. E, and R. C. Sutherlin (2004). *Metallography and Microstructures of Zirconium, Hafnium, and Their Alloys*, *Metallography and Microstructures*, ASM Handbook, ASM International, **9**: 942-958
- De Carlan, Y., et al. (1996). Influence of iron in the nucleation of <c> component dislocation loops in irradiated zircaloy-4. *Am. Soc. Test. & Mater. STP* **1295**: 638-653.
- Ells, C. E. (1968). Hydride Precipitates in Zirconium Alloys (A review), *J. Nucl. Mater.* **28**: 129-151.
- Erikson, W. H., and D. Hardie (1964). The influence of alloying elements on the terminal solubility of hydrogen in alpha-zirconium, *J. Nucl. Mater.* **13**: 254-262.
- Eshelby, D. (1957). The determination of the elastic field of an ellipsoidal inclusion, and related problems, *Proc. R. Soc. A* **241**: 376-396.
- Frank, W. (1988). Intrinsic point defects in hexagonal close-packed metals, *J. Nucl. Mater.* **159**: 122-148.
- Gilbert, R.W., K. Farrell, and C. E. Coleman (1979). Damage structure in zirconium alloys neutron irradiated at 573 to 923 K, *J. Nucl. Mater.* **84**: 137-148.

- Griffiths, M., J. F. Mecke, and J. E. Winegard (1996). Evolution of Microstructure in Zirconium Alloys During Irradiation, in *Zirconium in the Nuclear Industry: Eleventh International Symposium*, E. R. Bradley and G. P. Sabol, Eds., Am. Soc. Test. & Mater. STP **1295**: 580-602.
- Hansen, G. (2012). 2D Multimaterial Heat Conduction in Cylindrical Geometry With Source, unpublished.
- Holt, R. A., and R. W. Gilbert (1986). $\langle c \rangle$ -component dislocations in annealed Zircaloy irradiated at about 570 K, *J. Nucl. Mater.* **137**: 185-189.
- Homer, E. R., V. Tikare, and E. A. Holm (2013). Hybrid potts-phase field model for coupled microstructural and compositional evolution, *Comput. Mater. Sci.* **69**: 414-423.
- Hood, G. M. (1988). Point Defect Diffusion in alpha-Zr, *J. Nucl. Mater.* **159**: 149-175.
- Kearns, J.J. (1967). Terminal Solubility and Partitioning of Hydrogen in the Alpha Phase of Zirconium, Zircaloy-2 and Zircaloy-4, *J. Nucl. Mater.* **22**: 292-303.
- Kearns, J.J. (1972). Diffusion-coefficient of hydrogen in alpha zirconium, zircaloy-2 and zircaloy-4, *J. Nucl. Mater.* **43**: 330-338.
- Louthan, M.R., and R.P. Marshall (1963). Control of Hydride Orientation in Zircaloy, *J. Nucl. Mater.* **9**: 170-184 (1963).
- Mallett, M. W., and W. M. Albrecht (1957). Low-pressure solubility and diffusion of hydrogen in zirconium, *J. Electrochem. Soc.* **104**: 142-146.
- Northwood, D. O., and R. W. Gilbert (1974). Neutron radiation damage in zirconium and its alloys. *Radiation Effects* **22**: 139-140.
- Northwood, D.O. (1977). Irradiation damage in zirconium and its alloys. *Energy Reviews* **15**: 547-610.
- Northwood, D.O., et al., (1979). Characterization of neutron irradiation damage in zirconium alloys - an international "round-robin" experiment. *J. Nucl. Mater.* **79**: 379-394.
- NUREG (1997). 1536, Standard Review Plan for Spent Fuel Dry Storage Systems at a General License Facility, US NRC 1997.
- Osetsky, Y. N., Bacon, D. J., & De Diego, N. (2002). Anisotropy of point defect diffusion in alpha-zirconium. *Metall. & Mater. Trans. A: Physical Metallurgy and Materials Science* **33**: 777-782.
- Pan, Z. L., I. G. Ritchie, and M. P. Puls (1996). The terminal solid solubility of hydrogen and deuterium in Zr-2.5Nb alloys, *J. Nucl. Mater.* **228**: 227-237.
- Pasianot, R. C., and A. M. Monti (1999). A many body potential for α -Zr. Application to defect properties, *J. Nucl. Mater.* **264**: 198-205.
- Perovic, V., G. R. Purdy, and L. M. Brown (1981). Autocatalytic Nucleation and Elastic Stabilization of Linear Arrays of Plate-Shaped Precipitates, *Acta Metall.* **29**: 889-902.

- Perovic, G. C. Weatherly, and C. J. Simpson (1982). Role of Elastic Strains in the Foramtion of Stacks of Hydride Precipitates in Zirconium Alloys, *Scripta Metall.* **16**: 409-412.
- Perovic, V., G. C. Weatherly, and C. J. Simpson (1983). Hydride Precipitation in α/β Zirconium Alloys, *Acta Metall.* **31**: 1381-1391.
- Perovic, V., and G. C. Weatherly (1984). The Nucleation of Hydrides in a Zr-2.5wt% Nb Alloy, *J. Nucl. Mater.* **126**: 160-169.
- Perovic, V., G. C. Weatherly, S. R. MacEwen, and M. Leger (1992). The influence of Prior Deformation on Hydride Precipitation in Zircaloy, *Acta Metall. Mater.* **40**: 363-372.
- Rashid, J., and A. Machiels (2007). Threat of Hydride Re-orientation to Spent Fuel Integrity During Transporation Accidents: Myth or Reality?, *Proc. 2007 International LWR Fuel Performance Meeting*.
- Rogerson, A. (1988). Irradiation growth in zirconium and its alloys. *J. Nucl. Mater.* **159**: 43-61.
- Root, J. H., and R. W. L. Fong (1996). Neutron diffraction study of the precipitation and dissolution of hydrides in Zr-2.5Nb pressure tube material, *J. Nucl. Mater.* **232**: 75-85 (1996)
- Sawatzky, A. (1960). Hydrogen in Zircaloy-2: Its Distribution and Heat of Transport, *J. Nucl. Mater.* **2**: 321-328.
- Sawatzky, A., and B. J. S. Wilkins (1967). Hydrogen solubility in zirconium alloys determined by thermal diffusion, *J. Nucl. Mater.* **22**: 304-310.
- Shimskey, R. W., and C. A. Lavender (2014). Personal communication, July 11, 2014.
- Slattery, G. F. (1967). The terminal solubility of hydrogen in zirconium, *J. Ins. Metal.* **95**: 43-47.
- Tikare, V., E. R. Homer, and E. A. Holm (2012). A Model for simulation of coupled microstructural and compositional evolution, in *Ceramic Materials for Energy Applications II*, John Wiley & Sons, Inc., **360**, 145-157.
- Une, K., and S. Ishimoto (2003). Dissolution and precipitation behavior of hydrides in Zircaloy-2 and high Fe Zircaloy, *J. Nucl. Mater.* **322**, 66-72.
- Woo, C. H., & Gosele, U. (1983). Dislocation bias in an anisotropic diffusive medium and irradiation growth, *J. Nucl. Mater.* **119**: 219-228.
- Zee, R. H., Carpenter, G. J. C., Rogerson, A., & Watters, J. F. (1987). Irradiation growth in deformed zirconium, *J. Nucl. Mater.* **150**: 319-330.